Heterogeneous doping and superconductivity in La_2CuO_4-based heterostructures

Von der Fakultät Chemie der Universität Stuttgart
zur Erlangung der Würde eines

Doktors der Naturwissenschaften

(Dr. rer. nat.) genehmigte Abhandlung

Vorgelegt von
Federico Baiutti
aus Fiumicello (Udine), Italien

Hauptberichter:	Prof. Dr. Joachim Maier
Mitberichter:	Prof. Dr. Peer Fischer
Prüfungsvorsitzenderin:	Prof. Dr. Anke Weidenkaff

Tag der Einreichung:	19.06.2015
Tag der mündlichen Prüfung:	24.07.2015

Max-Planck-Institut für Festkörperforschung
Stuttgart
2015

Erklärung

Die vorliegende Doktorarbeit wurde vom Autor selbst in der Abteilung von Prof. Maier am Max-Planck-Institut für Festkörperforschung, im Zeitraum von August 2011 bis Juni 2015 angefertigt. Der Inhalt ist die eigene Arbeit des Autors, Ausnahmen sind gekennzeichnet, und wurde noch nicht zur Erlangung einer Qualifizierung oder eines Titels an einer akademischen Institution eingereicht.

Stuttgart, den 19. Juni 2015 Federico Baiutti

Declaration

The work described in this thesis was carried out by the author in the Department of Prof. Maier at the Max Planck Institute for Solid State Research from August 2011 to June 2015. The contents are the original work of the author except where indicated otherwise and have not been previously submitted for any other degree or qualification at any academic institution.

Stuttgart, 19th June 2015 Federico Baiutti

To my family.

Contents

Zusammenfassung

Die Effekte an Grenzflächen von ionischen Materialien stellen eindrucksvolle Möglichkeiten im Hinblick auf die Realisierung von nanoskaligen Systemen mit verbesserten oder neuartigen Funktionen dar. Auf Grund dessen waren sie in den vergangenen Jahren Gegenstand zahlreicher Studien.

Speziell das heterogene Dotieren, das es erlaubt durch Zuführen von Grenzflächen lokal chemische und funktionelle Eigenschaften abzustimmen, wurde besonders im Hinblick auf ionisch- und gemischt ionisch-elektronische Leiter untersucht. Es hat sein Potential gegenüber dem "konventionellere" homogenen Dotieren bewiesen, das im Gegensatz dazu auf der Einführung von statistisch verteilten Dopanden im Host-Material beruht. Auf ähnliche Weise haben eine Reihe von Untersuchungen im Gebiet der oxidischen elektronischen Materialien die Möglichkeit der gezielten Manipulation von Grenzflächeneigenschaften hervorgehoben, (z.B. induzierte Metallartigkeit, Supraleitfähigkeit, Magnetismus) in dem Materialien durch einen kristallographisch geordneten Aufbau verbunden wurden, z.B. durch Erschaffung von epitaktischen Grenzflächen.

In der vorliegenden Arbeit wurde das Auftreten von Supraleitfähigkeit basierend auf heterogenem Dotieren von Lanthankuprat (La_2CuO_4) in epitaktisch angeordneten Systemen untersucht. La_2CuO_4 kann vom Isolator zum Supraleiter übergehen, wenn die Lochleiterkonzentration durch Dotieren erhöht wird. Es ist somit ein geeignetes Modelsystem mit gut untersuchten physikalischen und chemischen Eigenschaften und vergleichsweise simpler Struktur. Außerdem stellt die Untersuchung von Kupraten im Hinblick auf Hochtemperatursupraleitung ein sehr faszinierendes Forschungsgebiet dar, wozu der immer noch nicht vollständig ver-

standene Effekt und deren großes Potential für elektronische Anwendungen beitragen.

Es wurden zwei Strukturtypen untersucht: erstens, einer Schichtstruktur von La_2CuO_4 und $La_{2-x}Sr_xNiO_4$ (Lanthanstrontiumnickelat), zweitens, zwei-dimensional dotiertem La_2CuO_4. Um die höchstmögliche Probenqualität zu erreichen, wurden epitaktische dünne Filme durch atomare Schicht-Für-Schicht-Anordnung mit Hilfe der oxidischen Molekularstrahlepitaxie (ALL-Oxide MBE) erzeugt. ALL-Oxide MBE ermöglicht eine präzise Kontrolle der Zusammensetzung jeder einzelnen atomaren Schicht in der Struktur. Die Installation und die Optimierung eines ALL-Oxide MBE Systems, sowie die Einführung dieser Technik zur Erzeugung der gewünschten Probeneigenschaften, ist ein wichtiger Teil der vorliegenden Arbeit.

Die Durchführbarkeit der zuvor beschriebenen schichtartigen Strukturen wird zunächst anhand der erfolgreichen Implementierung des ALL-Oxide MBEs zum Wachstum von einphasigen Komponenten wie La_2CuO_4, La_2NiO_4 und $La_{2-x}Sr_xNiO_4$ demonstriert. Die Grenzen der Phasenstabilität und die kritischen Parameter während der Synthese stehen dabei im Vordergrund.

Die La_2CuO_4 /$La_{2-x}Sr_xNiO_4$ Hetero- (Bi- oder Multischicht-) strukturen wurden untersucht, um die Grenzflächeneffekte, die durch die Migration der positiven Ladungsträger, wie Elektronenlöcher und Sauerstofffehlstellen, vom $La_{2-x}Sr_xNiO_4$ in das La_2CuO_4, zu enthüllen. In diesem Fall und um das thermodynamische Gleichgewicht aufrecht zu erhalten, kann eine Region mit angereicherten Lochladungsträgern an der Grenzschicht des La_2CuO_4 angenommen werden (Space-Charge Effekten), die letztendlich das Auftreten von Hochtemperatursupraleitung, auf Grund des lokal positiven Dotierens, erwarten lässt. Obwohl keine der zusammengesetzten Phasen für sich allein genommen supraleitend ist, tritt in der Probe Hochtemperatursupraleitung mit einer kritischen Temperatur T_c von ≈ 35 K auf. Ergänzende Untersuchungen weisen auf eine Ladungsumverteilung an der Grenzfläche hin, in der auch die kationische Stöchiometrie eine Rolle spielt und durch die die erhaltenden Ergebnisse erklärt werden können.

Im zweiten Fall, dem zwei-dimensional dotierten Lanthankuprat, werden in Multischichtstrukturen die atomaren LaO Schichten in der La_2CuO_4 Kristall-

struktur durch MO Schichten substituiert, wobei M ein Akzeptordopand darstellt (M=Sr, Ba, Ca). Eine Reihe von Experimenten in Abhängigkeit der zwei-dimensional gedopten Schichten zeigte, dass eine exakte Lochansammlung auftritt, die für das Auftreten der Hochtemperatursupraleitung ($T_c \approx 35$ K) verantwortlich gemacht wird. Dieser Effet wird dem gleichzeitigen Auftreten von heterogenem und homogenem Dotieren zugeschrieben, die gleichzeitig an gegenüberliegenden Seiten der dotierten Schichten aktiv sind (und deshalb räumlich getrennt sind). Bemerkenswerterweise stehen beide unabhängig voneinander im Zusammenhang mit der Supraleitfähigkeit. Dadurch kann ein direkter Vergleich zwischen den beiden Dotierungsarten gezogen werden, wodurch das Potential des heterogenen Dotierens gegenüber dem homogenen gezeigt werden kann.

Die in dieser Arbeit vorgestellten Ergebnisse demonstrieren, dass Hochtemperatursupraleitfähigkeit in auf La_2CuO_4-basierenden Heterostrukturen durch heterogenes Doping induziert werden kann. Außerdem weißt dies auf die komplexen Zusammenhänge zwischen (i) Ladungsumverteilung basierend auf Space-Charge Effekten, (ii) kationischem Intermixing und (iii) strukturellen Aspekten hin, die zu der gezielten Abstimmung von faszinierenden Eigenschaften in epitaktischen oxidischen Grenzflächen beitragen.

Abstract

Effects arising at interfaces in ionic materials represent an exciting opportunity towards the realization of nanosized systems having improved or novel functionalities. For this reason, they have been the object of a number of studies in recent years.

In particular heterogeneous doping, relying on the introduction of interfaces in order to locally tune the chemical and functional properties, has been extensively studied in the context of ionic and mixed ionic-electronic conductors, and has proven its potential in comparison with the more "conventional" homogeneous doping, which is based instead on the introduction of randomly placed dopant ions in the host material. In a similar way, in the field of oxide electronics, a number of investigations highlighted the possibility of engineering interfacial properties (e.g. inducing metallicity, superconductivity, magnetism), by coupling materials in a crystallographic ordered fashion, i.e. forming epitaxial interfaces.

In the present study, we investigate the possibility of obtaining high-temperature superconductivity in epitaxial systems based on lanthanum cuprate (La_2CuO_4) by means of heterogeneous doping. La_2CuO_4, which undergoes an insulator-to-superconductor transition upon hole doping, represents a suitable model system due to his well-known physical and chemical properties and to the relatively simple structure. In addition, the study of cuprates in relation to high-temperature superconductivity represents a highly fascinating topic owing to the still open questions related to such an effect and to its great potential for electronic applications.

Two type of structures are investigated: the first one consists of heterostructures of La_2CuO_4 and $La_{2-x}Sr_xNiO_4$ (lanthanum strontium nickelate), the second

one of two-dimensionally doped La_2CuO_4. In order to ensure the best sample quality, epitaxial thin films are realized by means of atomic-layer-by-layer oxide molecular-beam-epitaxy (ALL-Oxide MBE). ALL-oxide MBE allows for a precise control of the composition of each atomic layer of the structure. The installation and the optimization of an ALL-oxide MBE system, together with the implementation of such a technique for the realization of the samples, is an important part of the present work.

The feasibility of the synthesis of the structures described above is first proved by successfully implementing ALL-oxide MBE for the growth of the single phase constituents, i.e. La_2CuO_4, La_2NiO_4 and $La_{2-x}Sr_xNiO_4$. Phase stability limits and synthesis critical points are put into the fore.

In the case of La_2CuO_4 / $La_{2-x}Sr_xNiO_4$ heterostructures, bi- and multilayered (superlattice) structures are studied in order to unveil possible interface effects arising from the migration of positive charge carriers, namely electron holes and oxygen vacancies, from $La_{2-x}Sr_xNiO_4$ into La_2CuO_4 . In such a situation, in order to maintain thermodynamical equilibrium, a region of hole accumulation is expected to form at the La_2CuO_4 side of the interface (space-charge effect), having as a final consequence the occurrence of high-temperature superconductivity due to local p-type doping. Notably, although none of the constituting phases is superconducting if taken singularly, the resulting samples indeed exhibit high-temperature superconductivity with critical temperature T_c up to ≈ 35 K. Complementary investigations indicate that effects of charge redistribution at the interface, in which also the cationic stoichiometry plays a role, can be accounted for the findings.

In the second case i.e. two dimensionally doped lanthanum cuprate, superlattices are obtained by substituting LaO atomic layers in the La_2CuO_4 crystal structure with MO layers, in which M is an acceptor dopant (M=Sr, Ba, Ca). A number of independent experiments demonstrate that, in proximity of the two-dimensionally doped layer, a sharp hole accumulation occurs giving rise to high-temperature superconductivity (T_c up to ≈ 35 K). Such an effect is ascribed to the occurrence of both heterogeneous and homogeneous doping mode, which are simultaneously active at the opposite sides of the doped layer (and thus spatially

separated). Remarkably, they both independently contribute to superconductivity. Such a situation allows for a direct comparison between the two doping modes and for pointing out the potentialities of heterogeneous doping over the homogeneous situation.

The findings presented in this work demonstrate the feasibility of inducing high-temperature superconductivity in La_2CuO_4-based heterostructures by heterogeneous doping. Moreover, they highlight the complex interplay among (i) charge redistribution based on space-charge effects, (ii) cationic intermixing and (iii) structural aspects, which contribute to the definition of the fascinating properties of epitaxial oxide interfaces.

Chapter 1

Introduction and motivation

Oxide materials exhibit a great variety of functional properties, spanning a whole spectrum of electrical, optical and magnetic behaviors, and great attention has been devoted to their study in recent years.

In oxide-based systems, particular attention has been lately addressed towards the investigation of effects appearing in the presence of an interface (*interface effects*), which can lead not only to improved functionalities but even to the occurrence of novel properties that do not belong to the bulk. In this sense, the introduction of an interface is a powerful tool in order to locally tailor material functionalities and is particularly interesting in nanosized systems exhibiting a large volume fraction of interfaces. This approach has a great potential application in electronic and electrochemical devices.[1,2]

This strategy has seen early development in the context of ionic and mixed ionic/electronic conductors, where the intentional introduction of interfaces has been extensively studied as a novel doping technique (*heterogeneous doping*) in comparison with the classical *homogeneous doping*, in which aliovalent ions are randomly dissolved in a host material with the purpose of enhancing the concentration of specific charge carriers.[3] Heterogeneous doping relies on the deliberate two-dimensional confinement of an excess charge yielding, at the interface, a spatially confined and thermodynamically necessary charged zone (*space charge-zone*). Here, the usual electroneutrality condition is replaced by Poisson's equation and

respective boundary conditions.[4] As a consequence, a local rearrangement of the defect concentrations (mobile ionic and electronic), eventually leading to a modification of the material electrical properties in the space-charge zone, is obtained. By appropriately decreasing the distance between interfaces, these effects may become predominant over the bulk behavior and deeply affect the overall material functionalities.

A clear example in this sense has been highlighted by Lupetin *et al.*, who investigated the electrical behavior of polycrystalline strontium titanate ($SrTiO_3$) upon grain-size decrease.[5] Due to the intrinsic excessive positive charge at the grain boundary core (which is usually assigned to excess of oxygen vacancies and/or cation segregation),[6,7] nanocrystalline $SrTiO_3$ is characterized by an exemplary electrical behavior. In particular, it was shown that, by decreasing the grain size, *p*-type and ionic conductivity are depressed by about 3 and 6 orders of magnitude, respectively, whereas *n*-type conductivity is greatly enhanced (about 3 orders of magnitude) in comparison with a microcrystalline structure (see Figure 1.1). A similar example is given by the study of the cerium oxide (CeO_2) system, in which the conduction mechanism was switched from ionic to electronic upon grain-size reduction.[8–10]

Space-charge effects have been highlighted not only in relation with grain boundaries of polycrystalline materials, but also in correspondence of line defects such as edge dislocations. For example Adepalli *et al.* demonstrated the influence of dislocations in single crystals of titanium oxide (TiO_2): due to the excess negative charge at the dislocations core (supposed to stem from a local increased titanium vacancies concentration), a positive charge carrier accumulation leading to the switch of the conductivity from *p*-type to ionic (oxygen vacancies) was found.[12]

Epitaxial structures, in which different phases are stacked on top of each other to form a thin film with controlled crystallographic orientation and predefined number of interfaces, represent a very exciting playground for the study of interface effects due to the well-defined geometry and to the possibility of tailoring layers thickness at wish. The investigation of the CaF_2/BaF_2 system which was

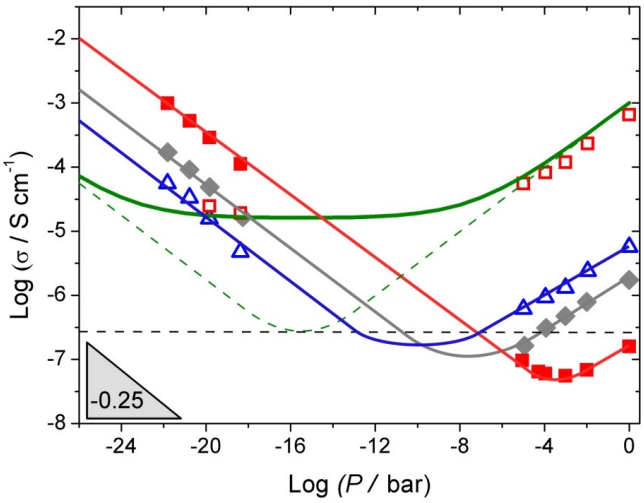

Figure 1.1. Conductivity versus oxygen partial pressure for $SrTiO_3$ (at $T = 544$ °C) . The symbols are assigned as follows: (red open squares) bulk microcrystalline $SrTiO_3$; (blue open triangles) grain boundaries of the microcrystalline $SrTiO_3$; (grey diamonds) nanocrystalline $SrTiO_3$ (grain size ≈ 50 nm); (solid red squares) nanocrystalline $SrTiO_3$ with the effective grain size of ≈ 30 nm. The continuous green line illustrates the conductivity behaviour of the microcrystalline bulk as espected from the literature.[11] Reproduced with permission from Ref. 5.

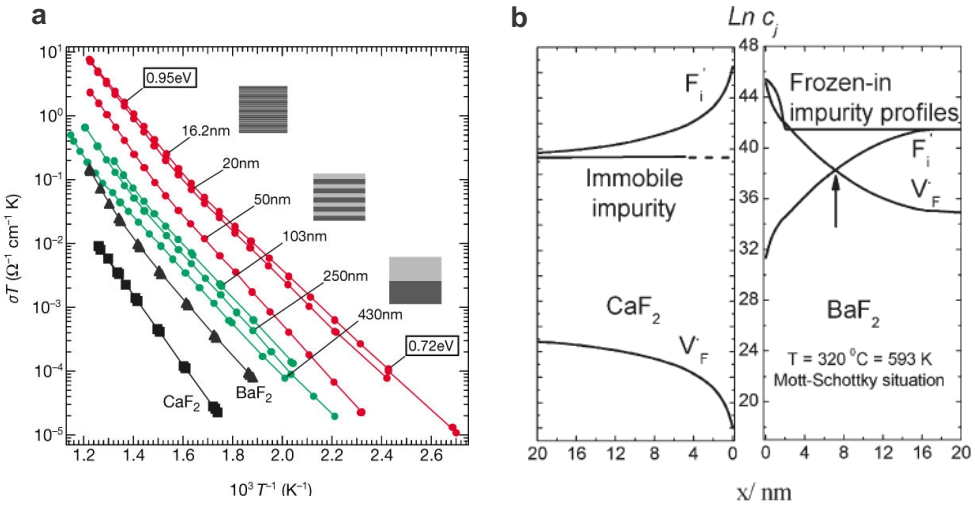

Figure 1.2. a) Conductivity as a function of temperature for CaF_2/BaF_2 heterostructures with variable interface density. Reproduced with permission from Ref. 13. b) Interface defect profiles at $T = 320$ °C for semi-infinite CaF_2/BaF_2 layers. Reproduced with permission from Ref. 15.

carried out by Sata *et al.* showed that, by appropriately increasing the interface density, higher ionic conductivity along the interface is obtained (Figure 1.2a).[13] Both single phase components are ionic conductors with fluorine ion F^- as main charge carrier: if CaF_2 and BaF_2 are brought into contact, F^- redistribution occurs (namely, transfer of fluorine ion in the direction of CaF_2). This determines the increase of fluorine vacancies on the BaF_2 side and of fluorine interstitials on the CaF_2 side within the space-charge region (Figure 1.2b).[14,15] If the system is nanosized (and each layer thickness approaches the space-charge width) such a modified charge carrier distribution eventually results in the modification of the overall material electrical behavior.

Interface effects have also substantially contributed to the observation of unexpected phenomena in the field of oxide electronics in the recent years. One of the earliest examples in this sense was given by Hammerl *et al.*, which showed the potentiality of "grain-boundary doping" in polycristalline $YBa_2Cu_3O_{7-\delta}$: here, by changing the chemical composition of the grain boundaries, increased values of

supercurrent density were obtained.[16]

The breakthrough in this field was however represented by the discovery of the formation of a conducting interface between two insulators $SrTiO_3$ and $LaAlO_3$ (the same system was later found to be also locally superconducting and magnetic), becoming the pole of attraction and inspiration for numerous studies.[17–19] One of the most accepted explanations invokes the presence of electronic redistribution, i.e. the electron transfer from the surface of $LaAlO_3$ to the interface of $SrTiO_3$ in order to compensate for the built-up electrostatic potential ("polar catastrophe") arising from the different net charges of the single atomic layers constituting the two phases.[20,21] Namely, this derives by considering the structure as an "ideal" system in which neutral $(SrO)^0$ and $(TiO_2)^0$ planes of $SrTiO_3$ are stacked with charged $(LaO)^{+1}$ and $(AlO_2)^{-1}$ planes of $LaAlO_3$ ("polar discontinuity"). This scenario received some criticisms as it neglects the possible presence of structural imperfections or the role of ionic charges, so alternative explanations have been proposed. It was shown that also other effects, such as oxygen nonstoichiometry (i.e. oxygen vacancies acting as a dopant for $SrTiO_3$) or cationic redistribution (i.e. La migration from $LaAlO_3$ into $SrTiO_3$ acting as a donor) can be involved.[17,20,22–25] Some of the different scenarios are illustrated in Figure 1.3.

Further examples dealing with different materials or properties have been recently published. They comprise for example the occurrence of metallic conductivity and superconductivity at the $LaTiO_3$ / $SrTiO_3$ interface or the formation of a ferromagnetic state between an antiferromagnetic insulator and a paramagnetic metal ($CaMnO_3$ and $CaRuO_3$),[26–28] in both cases as a consequence of local electronic charge transfer.[29] In particular the case of the interface between metallic $La_{2-x}Sr_xCuO_4$ and insulating La_2CuO_4, which has been explored by the group of Bozovic, exhibits some similarities with the work which will be presented in the following. It was demonstrated that high-temperature superconductivity (a property which do not pertain to any of the constituting phases) is induced in La_2CuO_4 as a consequence of hole injection. The latter was ascribed to a chemical potential gradient leading to hole transfer.[30,31] Decoupling of hole and dopant distribution was demonstrated in Refs. 32, 33, which also show that high-temperature

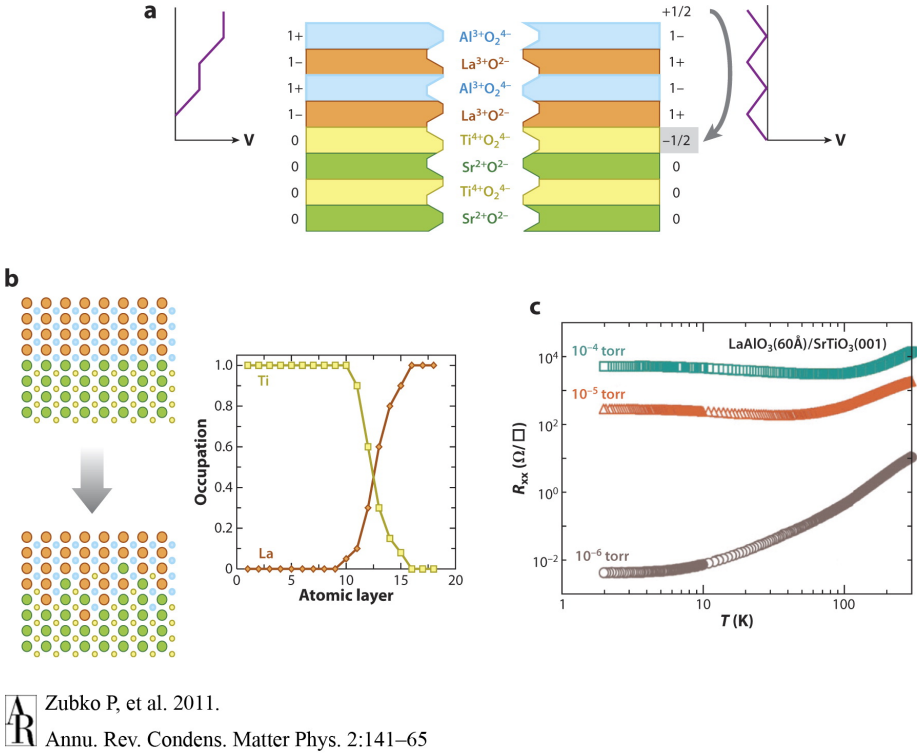

Zubko P, et al. 2011.
Annu. Rev. Condens. Matter Phys. 2:141–65

Figure 1.3. Possible scenarios occurring at the $LaAlO_3$ / $SrTiO_3$ interface. a) Formation of electron gas as a consequence of the polar discontinuity between the $LaAlO_3$ and the $SrTiO_3$ layers.[20,21] b) Chemical analyses, supported by ab-initio calculation, have revealed the tendence of a certain cationic intermixing. The depth profiles for the Ti and La ions shown here have been measured by electron energy loss spectroscopy (original data from Ref. 20). c) Effect of growth conditions, in particular of the oxygen partial pressure used during the fabrication, suggestive of a certain role of oxygen vacancies in the interface functionalities.[17] Reproduced with permission from Ref. 2.

superconductivity is confined in a single CuO_2 plane.

Scope of the work and outline of the project

As one can infer from the examples given above, the explanations of interface effects are controversial: in the field of electrochemistry, interface effects are in general associated with ionic charge rearrangement as a consequence of forces acting on the ions, aspects which, instead, are usually considered as secondary and detrimental in case of electronic systems. Notwithstanding this, it is the goal of the present study to use the concepts of heterogeneous doping and of ionic space-charge in order to induce high-temperature superconductivity. The model system of choice are epitaxial structures of La_2CuO_4, which is the material of reference in the field of high-temperature superconductivity and which represents a great model in consideration of its well-known physical and chemical properties. Moreover, due to its layered structure, it is intrinsically a suitable candidate for the realization of artificial superstructures.

The project consists in the synthesis and in the structural and functional characterization of selected multilayered heterostructures. An important part resides in the samples preparation, representing here a particularly important aspect also in consideration of the fact that high-temperature superconductivity is extremely sensitive to the crystalline quality of the material. For this reason, the Oxide Molecular Beam Epitaxy (Oxide MBE) method, which is a sophisticated technique for the precise realization of oxide heterostructures, has been employed. During the time of the project, I personally contributed to the installation and optimization of the Oxide MBE system which is currently installed at the Max-Planck Institute in Stuttgart.

Chapter 2

Theoretical background

2.1 Properties of A_2BO_4-type structures

Lanthanum cuprate (La_2CuO_4) and lanthanum nickelate (La_2NiO_4), materials which are the main object of the present work, share the same A_2BO_4-type structure. In the following section, structure and defect chemistry of the two systems are discussed. The conventions used for the defect chemistry modeling follow the Kröger-Vink notation.[34]

2.1.1 Crystal structure

The A_2BO_4-type structure, which is represented in Figure 2.1, is a Ruddlesden-Popper (R-P) phase having the general formula $AX(ABX_3)_n$. The structures belonging to a R-P series are formed by a number n of perovskite blocks ABX_3 separated by AX rock-salt layers (in case of A_2BO_4, n=1).[35,36] The A cation site is, both for La_2CuO_4 and La_2NiO_4, occupied by nine-fold coordinated La^{+3}, whereas the B cation (Cu^{+2} and Ni^{+2} for La_2CuO_4 and La_2NiO_4, respectively) is placed in the center of a BO_6 oxygen octahedra and is six-fold coordinated. The BO_6 structure is highly distorted, with the B-O_{plane} bond length being remarkably shorter ($\approx$ 1.9 Å for both La_2CuO_4 and La_2NiO_4) than the out-of-plane B-O_{apical} distance ($\approx$ 2.5 Å and $\approx$ 2.2 Å for La_2CuO_4 and La_2NiO_4, respectively).[36,37]

Alternatively, the A_2BO_4-type structures can be viewed as made by an alter-

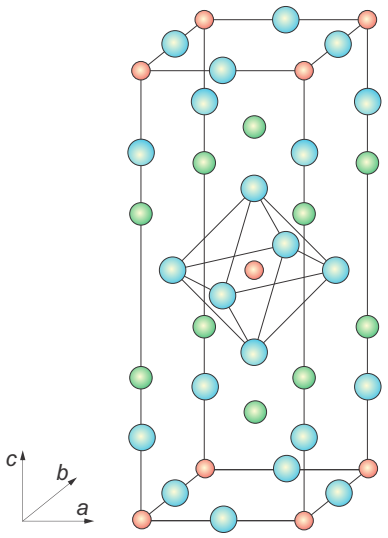

Figure 2.1. Crystal structure for La_2CuO_4 and La_2NiO_4 systems. Color are assigned as follows: blue= oxygen, green=lanthanum, red=copper (for La_2CuO_4) or nickel (for La_2NiO_4).

nation of two-dimensional layers which are stacked on top of each other, i.e. BO_2 planes separated by two AO layers.[38]

The room temperature crystal structure of La_2CuO_4 and La_2NiO_4 is slightly orthorombic; lattice parameters are summarized in Table 2.1.[37,39,40]

	$\mathbf{La_2CuO_4}$	$\mathbf{La_2NiO_4}$
$\boldsymbol{a}$ /Å	5.37	5.46
$\boldsymbol{b}$ /Å	5.41	5.49
$\boldsymbol{c}$ /Å	13.16	12.56

Table 2.1. Room temperature in-plane (a, b) and out-of-plane (c) lattice parameter for La_2CuO_4 and La_2NiO_4.[37,39,40]

A large amount of oxygen can be easily intercalated in the crystal (in the form of negatively charged interstitial defects between two LaO layers) forming hyperstoichiometric $A_2BO_{4+\delta}$.[41–43] In particular La_2NiO_4 can intercalate a large amount of extra oxygen (most references agree that in equilibrium at low temperature in air $\delta \approx 0.14$ for lanthanum nickelate),[43–45] whereas δ is generally considered

lower in lanthanum cuprate.[45,46]

A second way for varying the charge carriers concentration in this compounds is by substituting La^{+3} with an aliovalent cation. Most commonly, such doping is performed in order to increase the hole concentration via substitution of La^{+3} with a lower valent cation, namely Ca^{+2}, Sr^{+2}, Ba^{+2}. In Table 2.2, the Shannon ionic radius (for nine-fold coordination) for the different dopants, in comparison with La, is reported.

Noteworthy, as it will be described in details below (see Section 2.1.3), La_2CuO_4 undergoes an insulator-to-superconducting transition upon hole doping.

	ionic radius / Å	**relative difference with La**
La^{+3}	1.21	
Sr^{+2}	1.31	+8.26 %
Ca^{+2}	1.18	-2.47 %
Ba^{+2}	1.47	+21.48%

Table 2.2. Shannon ionic radius for common dopants for the La_2CuO_4 system (nine-fold coordinated).[47]

2.1.2 Defect chemistry of lanthanum cuprate

A detailed chemical model for La_2CuO_4 has been given by Maier *et al.*[48–50] As mentioned above, in the case of the native material, hole doping ($h^\bullet$) can be achieved via incorporation of oxygen. The feasibility of this doping technique has been experimentally verified and (superconducting) oxygen doped La_2CuO_4 has been obtained using different methods such as high pressure oxygen annealing, ozone annealing or by chemical and electrochemical methods.[51–55]

Oxygen doping consists in the incorporation of an interstitial (O_i'') in an empty interstitial site ($V_i^\times$) according to the reaction:

$$\frac{1}{2}\,O_2 + V_i^\times \rightleftharpoons O_i'' + 2\,h^\bullet \tag{2.1}$$

Which expresses the external defect equilibrium reaction between La_2CuO_4 and the gas phase.

The corresponding mass-action law (in which, in general, the mass-action constant for the r reaction (K_r) is defined as a function of the corresponding standard mass-action constant (K_r^0) and of the reaction enthalpy (ΔH_r)) is:

$$K_{\mathrm{ox}} = \frac{[\mathrm{O_i''}]p^2}{{P_{\mathrm{O_2}}}^{1/2}} = K_{\mathrm{ox}}^0 \exp\left(-\frac{\Delta H_{\mathrm{ox}}}{kT}\right) \tag{2.2}$$

with p being the hole concentration $[\mathrm{h}^\bullet]$, $P_{\mathrm{O_2}}$ being the oxygen partial pressure, k being the Boltzmann constant and T being the temperature.

As described above, another possibility to increase the hole concentration in La_2CuO_4 is based on acceptor doping, substituting La^{+3} with a divalent cation (general formula $La_{2-x}M_xCuO_4$, M=Sr, Ca, Ba).[38,56–58] Depending on the dopant, different solubilities (and superconducting properties, see Section 2.1.3) are obtained. The solubility limit can be estimated as $x \approx 0.1$ for Ca, whereas it is much higher for Ba, Sr (in both cases, $x \approx 1.4$). However, these values are strongly dependent on sample preparation method.[59–63]

The dopant incorporation reaction (which is considered as irreversible therefore mass-action law is not applicable to it) leads to an increase of the hole concentration according to the equation:

$$2\,\mathrm{SrO} + 2\,\mathrm{La_{La}^{\times}} + \frac{1}{2}\,\mathrm{O_2} \longrightarrow \mathrm{La_2O_3} + 2\,\mathrm{Sr'_{La}} + 2\,\mathrm{h^\bullet} \tag{2.3}$$

One should notice here that an equivalent possibility of formulating the dopant incorporation reaction predicts the formation of oxygen vacancies $\mathrm{V_O^{\bullet\bullet}}$:

$$2\,\mathrm{SrO} + 2\,\mathrm{La_{La}^{\times}} + \mathrm{O_O^{\times}} \longrightarrow \mathrm{La_2O_3} + 2\,\mathrm{Sr'_{La}} + \mathrm{V_O^{\bullet\bullet}} \tag{2.4}$$

For the defect chemistry of La_2CuO_4 one should also take into account the following equilibria reactions, namely the anti-Frenkel reaction involving an oxygen site ($\mathrm{O_O^{\times}}$):

$$\mathrm{O_O^{\times}} + \mathrm{V_i^{\times}} \rightleftharpoons \mathrm{O_i''} + \mathrm{V_O^{\bullet\bullet}} \tag{2.5}$$

and the band-band reaction expressing the electronic (e') transition from the valence into the conduction band:

$$nil \rightleftharpoons h^{\bullet} + e' \tag{2.6}$$

The corresponding mass-action laws read:

$$K_F = [O_i''][V_O^{\bullet\bullet}] = K_F^0 \exp\left(-\frac{\Delta H_F}{kT}\right) \tag{2.7}$$

$$K_B = p \cdot n = K_B^0 \exp\left(-\frac{\Delta H_B}{kT}\right) \tag{2.8}$$

for Equation (2.5) and Equation (2.6), respectively. Please note that, in Equation (2.8), n indicates the electron concentration $[e']$.

Finally, the electroneutrality condition can be written as follows:

$$2\,[O_i''] + [Sr_{La}'] + n = p + 2\,[V_O^{\bullet\bullet}] \tag{2.9}$$

By combining Equation (2.2), Equation (2.7), Equation (2.8) and Equation (2.9) one can readily solve the defect concentration as a function of the oxygen partial pressure at a fixed Sr content and at a given temperature.

In the particular case of the pure material, Equation (2.9) can be simplified as:

$$2[O_i''] = p \tag{2.10}$$

which, combined with Equation (2.2), results in:

$$p \propto P_{O_2}^{1/6} \tag{2.11}$$

as experimentally verified by conductivity experiments.[42,64,65]

In the case of Sr-doped material, the solution can be simplified for different regimes (see Figure 2.2):

- **Oxygen vacancies compensation.** At low oxygen partial pressures, the formation of oxygen vacancies is promoted and the simplified electroneutrality condition is $[Sr_{La}'] \simeq 2\,[V_O^{\bullet\bullet}]$. From here, a $1/4$ P_{O_2}- dependence is predicted

for holes (positive slope) and for electrons (negative slope). O_i'' concentration is constant (see Equation (2.7));

- **Hole compensation.** In the regime of intermediate oxygen pressure, a constancy of p is obtained ($[Sr'_{La}] \simeq p$). This situation is the most common in the usual preparation and measurement regimes and has been verified experimentally.[66] The oxygen vacancy and the oxygen interstitial concentrations vary with a $\pm 1/2$ P_{O_2}-dependence (positive slope for oxygen interstitials, negative for oxygen vacancies);

- **Oxygen excess.** At high P_{O_2}, double positively charged oxygen interstitial are expected to become majority defects leading to the electroneutrality condition $2\,[O_i''] \simeq p$. In this regime the dopant compensation becomes negligible. $+1/6$ slope is obtained for holes (and oxygen interstitials), whereas it is $-1/6$ for oxygen vacancies;

- It is worth emphasizing that, for extremely reducing conditions, one could even expect the electrons to take over the role of main compensating defect ($n \simeq 2[V_O^{\bullet\bullet}]$) (not indicated in Figure 2.2). In this case, the material would become n-type conducting, but this region probably lies beyond the stability range of the phase.[50]

A similar approach can be used in order to determine the defects concentration dependence as a function of Sr-doping, at a given oxygen partial pressure and temperature (Figure 2.3). A first regime, at very low Sr-content, is equivalent to the situation described by Equation (2.10). Increasing the Sr concentration leads to the formation of holes according to Equation (2.3) and to a decrease of oxygen interstitials (see Equation (2.2)). The oxygen vacancies concentration increases according to Equation (2.7). Due to the double charge, the latter takes over the role of compensation at high Sr-content. For very high doping levels, one can expect the formation of defects associates (e.g. $\{Sr'_{La}h^{\bullet}\}$, $\{Sr'_{La}V_O^{\bullet\bullet}\}^{\bullet}$, $\{2\,(Sr'_{La})V_O^{\bullet\bullet}\}$). In Figure 2.3 the case of formation of neutral associates ($\{2\,(Sr'_{La})V_O^{\bullet\bullet}\}$) is considered.

A confirmation of this point defect model has been provided by Shen *et al.* (see Figure 2.4).[67] Experimental data for oxygen deficiency and thermopower as

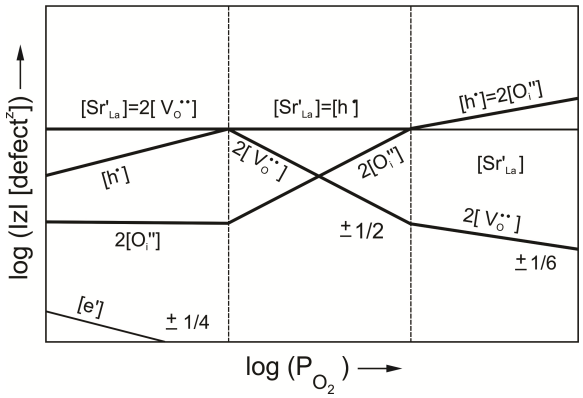

Figure 2.2. Defect concentration in La_2CuO_4 as a function of oxygen partial pressure at given Sr-content and constant temperature. Reproduced with permission from Ref. 48.

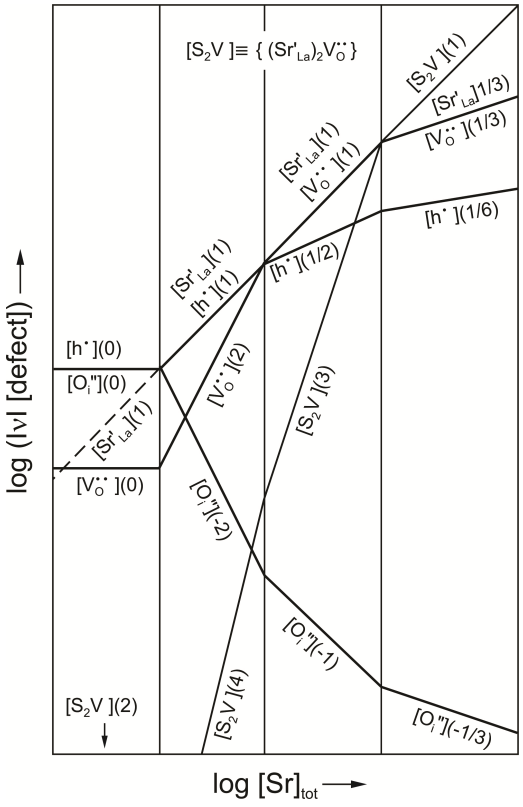

Figure 2.3. Modeled defect concentration in La_2CuO_4 as a function of Sr-doping at constant temperature and oxygen partial pressure. Reproduced with permission from Ref. 48.

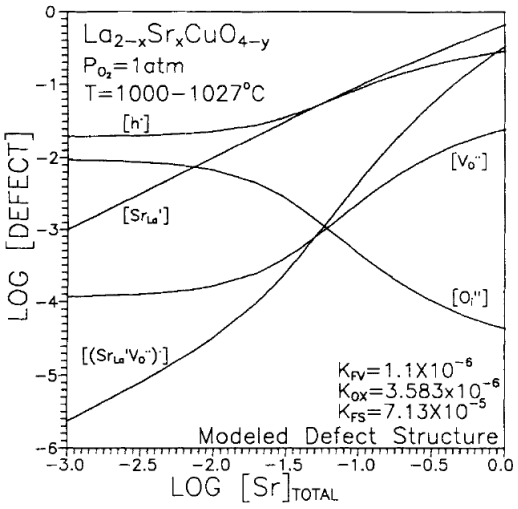

Figure 2.4. Calculated defect diagram vs dopant concentration, as obtained in Ref. 67 (reproduced with permission).

a function of dopant content have been fitted considering different possible defect mechanisms. The onset of oxygen deficiency was also investigated for different dopants (Sr, Ca, Ba): notably, it was set at $x \approx 0.15$ for Sr, Ba and at $x \approx 0.05$ for Ca. As described below (see Section 2.1.3), a relation between the superconducting properties of La_2CuO_4 and the amount of oxygen vacancies can be inferred from here.

Noteworthy, these ideal point defect models fail to predict material properties (e.g. oxygen diffusivity, oxygen deficiency or thermopower) for high dopant content suggesting that, in this situation, more complex situations characterized by activity coefficients or defect ordering effects come into play.[49,67]

The occurrence of point defects is strongly correlated with the variation of structural parameters of the La_2CuO_4. In particular, it has been shown that an increase of the Sr or oxygen concentration corresponds to an elongation of the cell in the *c*-direction. On the other hand, oxygen vacancies tend to shrink the cell.[57,59,62,66,68] As a consequence, an approximate linear relation can be found between the superconducting critical temperature and the *c*-axis lenght (see also Section 2.1.3).[63,69]

2.1.3 Superconductivity in lanthanum cuprate

Although a complete description of the electronic properties of La_2CuO_4 and of superconductors in general is beyond the scope of this thesis, a brief summary is presented here.

La_2CuO_4 forms the basis for one of the simplest layered cuprate superconductors and first discovered in 1986 by Bednorz and Müller.[70] Superconducting cuprates belong to the class of *high-temperature superconductors*, in which superconductivity occurs at temperatures which are close, or above, liquid nitrogen temperature (77 K), representing a very promising route for large scale applications. Up to date, the cuprate system Hg-Ba-Cu-O holds the record for the highest superconducting critical temperature (up to 155 K under high pressure).[71,72]

Although hole doped La_2CuO_4 is by far the most common and most studied compound in relation with high-temperature superconductivity , also an electron doped high-temperature superconducting system, obtained by oxygen vacancies and donor doping (typically Ce^{+4}) has been reported.[73–75]

Similarly to all the non-conventional superconductors such as iron-based superconductors,[76] the formation of *Cooper pairs* for superconductivity in cuprates cannot be explained as a consequence of electron-phonon interaction as described by the BCS theory.[77] Despite the great effort, a generally accepted explanation for high-temperature superconductivity is still missing.

The common element in all the high-temperature superconducting cuprates (other examples are $YBa_2Cu_3O_7$ and $Bi_2Sr_2CuO_6$) is the presence of CuO_2 planes, which are responsible for superconductivity. The surrounding blocks (for example the LaO layers in case of La_2CuO_4) are referred to as *charge reservoir*: by doping these blocks via substitutional atoms or oxygen, the carrier density of the CuO_2 planes can be tuned and high-temperature superconductivity can be induced.

According to the common electronic phase diagram for superconducting cuprates (Figure 2.5) the undoped material is an insulator with antiferromagnetic order.[39,78,79] Upon hole doping, the Néel temperature (T_N) undergoes a rapid fall-off and becomes zero at hole concentration $p \approx 0.02$. Superconductivity appears at $p \approx 0.05$ and the critical temperature for superconductivity (T_c)

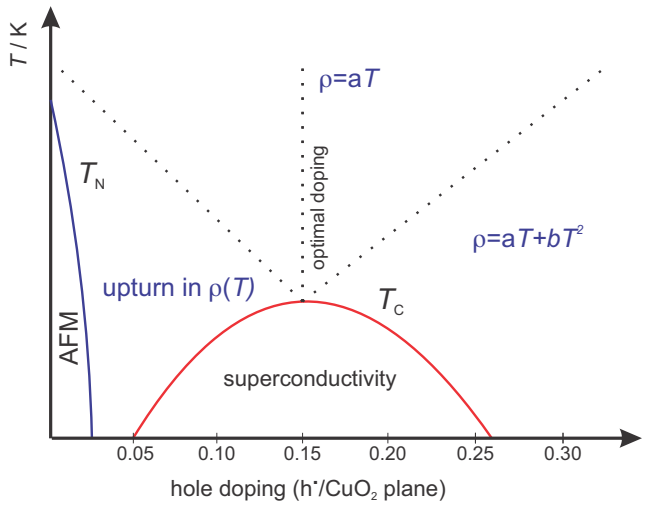

Figure 2.5. Phase diagram of hole-doped La_2CuO_4. The dashed lines represent the crossover in the in-plane $\rho(T)$ behavior. The blue (red) line describes the variation of T_N (T_c) as a function of the hole doping. The diagram is in agreement with Ref. 78.

increases for increasing doping level (underdoped region), reaching a maximum for $p \approx 0.15$ (optimal doping). If the hole concentration is further increased, the critical temperature decreases and eventually vanishes for $p \approx 0.26$ (overdoping). It is worth noticing the resistance behavior change upon doping: resistivity $\rho(T)$ is linear down to T_c for optimal doping, whereas it shows an upturn in case of underdoped material and becomes a quadratic function of T in the overdoped doping region.[38,63,78,80]

In the case of La_2CuO_4 the maximum T_c is $\approx$ 40 K and $\approx$ 48 K for bulk polycristalline and thin films respectively, and it is obtained for oxygen, Sr or Ba doping.[52,54,63,81,82] In the case of Ca doping instead, a maximum T_c of $\approx$ 20 K (for bulk polycrystalline samples) is reported.[61,83]

It is interesting here to remark some points concerning the link between the low temperature electronic phase diagram and the defect chemistry of La_2CuO_4. In particular, one can observe that reduced superconducting properties correspond to doping levels in which oxygen vacancies (or oxygen vacancies associates) become predominant. In particular, this regime is usually set at $x \geq 0.15$ and $x \geq 0.05$ for

Sr and Ca doped, respectively.[39,66,67] Moreover, it was shown that, for Ca doped La_2CuO_4, T_c can be raised up to the optimal values in the case of high pressure oxygen doping i.e. by decreasing the amount of oxygen vacancies.[60,84] This correspondence suggests that ionic defects, and in particular oxygen vacancies, play an important role in defining the electronic properties of La_2CuO_4. Moreover, it should be noticed that, when oxygen vacancies become predominant, the condition $x = p$ is no longer respected (see also Figure 2.3 and Figure 2.4) and an increase of dopant concentration does not necessarily imply an increased hole concentration.

It is also noteworthy that the superconducting properties of oxygen doped La_2CuO_4 samples show a peculiar behavior as a consequence of phase separation effects. It has been demonstrated that, supposedly under equilibrium conditions, oxygen is distributed in a non uniform fashion in $La_2CuO_{4+\delta}$: according to literature (see for example Ref. 85), for $0.1 \leq \delta \leq 0.055$, a macroscopic phase separation occurs into an oxygen-poor, antiferromagnetic, insulating phase ($\delta \approx 0.01$) and an oxygen-rich ($\delta \approx 0.055$) region, the latter being superconducting ($T_c \approx 32$ K).[68,85–88] Remarkably, increasing δ beyond 0.055 also results in a phase separated system, in which each phase is characterized by a different ordering in the interstitial oxygen distribution, resulting in locally different critical temperatures.[89–91] That is, under equilibrium conditions one always obtains step-like T_c's in $La_2CuO_{4+\delta}$.[85]

2.1.4 Defect chemistry and electrical properties of lanthanum nickelate

Due to the similar structure, the defect model for La_2NiO_4 is based on the same system of equations which has been already introduced for La_2CuO_4.[43,92–94] Nevertheless, the predicted hole (p) and oxygen interstitial ($[O_i'']$) dependences on P_{O_2} ($\propto P_{O_2}^{1/6}$, see Equation (2.10) and Equation (2.11)) are experimentally verified only in very specific conditions. In particular, the $[O_i'']$ dependence on P_{O_2} is usually lower than the predicted slope, unless strongly reducing conditions (high temperature, low oxygen pressure) are realized.[94,95] Several explanations have been formulated in this sense, taking into account defect interactions effects.[93,94,96]

Defect diagrams for some specific compositions have been proposed, but a general treatment is missing.[92,97]

As for the case of lanthanum cuprate, the c-axis parameter is first increased by the addition of dopant, then decreases as a consequence of oxygen vacancies formation.[98,99]

The most relevant aspects concerning the defect chemistry and the electrical properties of the La_2NiO_4 system can be summarized as follows:

- undoped $La_2NiO_{4+\delta}$ can be largely hyperstoiochiometrc, with δ being ≈ 0.14 in equilibrium at room temperature in air.[43–45] The oxygen content decreases for increasing Sr concentration in $La_{2-x}Sr_xNiO_4$ and oxygen hypostoichiometry is reported for compositions with $x \geq 0.5$. The oxygen vacancy content increases with the Sr concentration;[93,95]

- due to the very large oxygen excess, although being essentially an electronic (hole) conductor, ionic conductivity (through migration of oxygen interstitials) is high (the reported values for the intermediate temperature range exceed the typical values for perovskite ionic conductors). Oxygen diffusivity and, as a consequence, ionic conductivity, are highly anisotropic, with diffusion along the (a, b) plane being about one order of magnitude faster than the one along the c-axis direction;[100]

- conductivity monotonically increases for increasing x in $La_{2-x}Sr_xNiO_4$ and the material exhibits metallic behavior starting from $x \approx 0.9$. For metallic $La_{2-x}Sr_xNiO_4$, a resistivity upturn is observed at low temperature. Notably, such an upturn occurs at lower temperatures for increasing Sr content. Heavily doped $La_{2-x}Sr_xNiO_4$ eventually shows metallic behavior in the whole temperature range (typically for $x \geq 1.3$);[101,102]

- the choice of the dopant dramatically affects the structural and the electrical properties. In particular, unlike $La_{2-x}Sr_xNiO_4$, Ba- and Ca- doped lanthanum nickelates do not exhibit metallic conductivity. Rather, they stay insulating in the whole doping range.[98,103] The solubility range, which is extended up

to $x \approx 1.4$ for Sr doping, is limited to $x \approx 1.0$ for Ba and is lower for Ca ($x \approx 0.5$).[98,103,104] Also the oxygen content varies: in particular, the highest deficiency has been found for the $La_{2-x}Ba_xNiO_4$ system.[98]

2.2 Space-charge model

Space-charge situations stem from zones of an ionic crystal where, due to the presence of a crystallographic discontinuity, (e.g. a surface, a grain boundary or an epitaxial interfaces), a local deviation of the ion concentration from the bulk values (e.g. the formation of structurally necessary oxygen vacancies in the core of the grain boundaries of $SrTiO_3$, see Ref. 5) occurs leading to the local formation of an interface excess charge. The resulting interface potential ϕ_0, which differs from the bulk potential ϕ_∞, compensates the redistribution of the mobile charged defects species within the space charge region.[1,3,6,105,106]

In a space charge region, the usual electroneutrality condition, which holds in the bulk material, is no longer valid and is replaced by the general Poisson-equation. In the one-dimensional case (x direction) it is written as:[3,107,108]

$$\frac{\partial^2 \phi}{\partial x^2} = -\frac{Q(x)}{\epsilon_0 \epsilon_r} \tag{2.12}$$

with $Q(x)$ being the local charge density (per volume) in the space charge region, ϵ_0 the vacuum dielectric constant and ϵ_r the relative dielectric constant.

In order to describe the equilibrium situation, one needs to consider the electrochemical potential $\tilde{\mu}_j$ of each charge carrier j having effective charge number z_j. It is composed by a chemical term μ_j and of an electrical potential term $z_j e\phi$ according to the relation:[3,109,110]

$$\tilde{\mu}_j(x) = \mu_j + z_j e\phi(x) = \mu_j^0 + kT \ln c_j(x) + z_j e\phi(x) \tag{2.13}$$

in which the electrochemical potential at distance x from the interface is expressed as a function of the standard chemical potential μ_j^0, of the defect concentration c_j and of the electrical potential $\phi(x)$.

In equilibrium, the condition of constant electrochemical potential holds:

$$\tilde{\mu}_j(x) = \tilde{\mu}_{j,\infty} \tag{2.14}$$

with $\tilde{\mu}_{j,\infty} = \tilde{\mu}_j(x = \infty)$ being the bulk electrochemical potential.

By combining Equation (2.13) and Equation (2.14), one can express the concentration profile as a function of the potential difference $\Delta\phi(x) = \phi(x) - \phi_\infty$:

$$\frac{c_j(x)}{c_{j,\infty}} = \exp\left(-\frac{z_j e \Delta\phi(x)}{kT}\right) \tag{2.15}$$

with $c_{j,\infty}$ being the defect concentration in the bulk.

From Equation (2.12) and Equation (2.15), the Poisson-Boltzmann equation, which expresses the spatial variation of the electrical potential, can be written:

$$\frac{\partial^2\phi}{\partial x^2} = -\frac{e}{\epsilon_0\epsilon_r}\sum_j z_j c_{j,\infty} \exp\left(-\frac{z_j e \Delta\phi(x)}{kT}\right) \tag{2.16}$$

While the solutions of Equation (2.16) can be obtained numerically (e.g. see Ref. 111), two simplified models, namely the *Gouy-Chapman model* and the *Mott-Schottky model* have been developed for the descriptions of the charges behavior in the space-charge regions under specific assumptions. In both cases, an analytical solution for Equation (2.16) is found, whose substitution into Equation (2.15) allows for describing the concentration profiles.

2.2.1 Gouy-Chapman model

In this case, one considers all the charge carriers as mobile and capable of rearranging in order to compensate for the interface charge.[107,108] By setting appropriate semi-infinite boundary conditions

$$\Delta\phi(0) = \Delta\phi_0 \tag{2.17}$$

$$\Delta\phi(\infty) = 0 \tag{2.18}$$

(please note that $\Delta\phi(x) \equiv \phi(x) - \phi_\infty; \phi_\infty \equiv \phi_{bulk}$) one obtains:

$$\left(\frac{\partial\phi}{\partial x}\right)^2 = \frac{2kT}{\epsilon_0\epsilon_r}\sum_j c_{j,\infty}\left[\exp\left(-\frac{z_j e\Delta\phi(x)}{kT} - 1\right)\right] \tag{2.19}$$

Which can be analytically solved only in the case of two defects 1 and 2 with opposite charge number ($z = z_1 = -z_2$) and same bulk concentration c_∞. In this case Equation (2.19) becomes:[4,107,108]

$$\Delta\phi(x) = \frac{2kT}{ze}\ln\left[\frac{1 + \Theta\exp(-x/\lambda)}{1 - \Theta\exp(-x/\lambda)}\right] \tag{2.20}$$

with λ (Debye lenght) and Θ being respectively defined as:

$$\lambda = \sqrt{\frac{\epsilon_0\epsilon_r kT}{2z^2e^2c_\infty}} \tag{2.21}$$

$$\Theta = \tanh\left(\frac{ze\Delta\phi_0}{4kT}\right) \tag{2.22}$$

The effective extent of the space charge region is approximately estimated to be 2λ.[10] Notably, at a fixed temperature, it is dependent on the bulk defect concentration only (shrinking for higher c_∞).

2.2.2 Mott-Schottky case

In this model, one majority ionic defect (typically the dopant *dop*) having charge number z_{dop} is considered as immobile and uniformly distributed throughout the space charge region with concentration $c_{dop,\infty}$. The compensating counter-defect is depleted. Minority defects are neglected for the determination of the charge density in Equation (2.12):[107,108]

$$\frac{\partial^2\phi}{\partial x^2} = -\frac{z_{dop}ec_{dop,\infty}}{\epsilon_0\epsilon_r} \tag{2.23}$$

Defining the extent of the space charge region as λ^*, one can apply the semi-infinite boundary conditions:

$$\Delta\phi(\lambda^*) = 0 \tag{2.24}$$

$$\Delta\phi(0) = \Delta\phi_0 \tag{2.25}$$

Which finally lead to the equation:

$$\Delta\phi(x) = -\frac{z_{dop}ec_{dop,\infty}}{\epsilon_0\epsilon_r}(x-\lambda^*)^2 \tag{2.26}$$

where

$$\lambda^* = \sqrt{\frac{2\epsilon_0\epsilon_r\Delta\phi_0}{z_{dop}ec_{dop,\infty}}} = \lambda\sqrt{\frac{4z_{dop}e}{kT}\Delta\phi_0} \tag{2.27}$$

It is worth worth emphasizing that here, in contrast to the Gouy-Chapman case, the extent of the space charge region also depends on the interface potential $\Delta\phi_0$. Experimental applications of the Mott-Schottky model can be found, for example, in Ref. 5, 10.

2.3 Principles of thin film deposition

In comparison with bulk structures, thin films exhibit several peculiarities and advantages which allow for an accurate investigation of material and interface properties: (i) the material porosity can be limited, (ii) the presence of grain boundaries can be optimized, such that high quality single crystal samples can be obtained. Moreover, (iii) one can stack different materials on top of each other in a very controlled fashion, realizing multilayered systems with a predefined amount of interfaces thus focusing on interface effects (notably, interface effects are intrinsically emphasized by the quasi-two dimensional nature of the thin film structures). (iv) Modern growth methods allow for the control and the adjustment of the growth process down to the single atomic layer level. This can be used not only to achieve great film quality, but also to engineer the stoichiometry at the sub-unit cell scale. Lastly, (v) by appropriately selecting the substrate, one can introduce an additional degree for properties manipulation represented by elastic strain.

For these reasons, thin film technology has received great attention and several growth techniques, based on chemical (such as chemical vapor deposition (CVD) or atomic layer deposition(ALD)) or physical (e.g. sputtering, pulsed layer deposition (PLD), molecular beam epitaxy (MBE)) methods have been developed.

In physical deposition processes in particular, the thin film growth starts from the condensation and the chemical bonding of isolated atomic clusters on a substrate. This process is followed by film thickening due to additional deposition and ends with a fully developed film.[112] Various film microstructures can be obtained: amorphous, polycrystalline, textured or epitaxial. In contrast to the first two cases, a textured or epitaxial film is characterized by a preferred crystallographic orientation with respect to the substrate, forming a highly ordered structure with limited amount of undesired defects. In the case of epitaxial growth in particular, we observe the formation of a structure which can be considered as a single crystal having the highest quality.

Different theoretical models, based on thermodynamic or kinetic concepts, have been applied in order to describe thin film growth physics.[112–115] Their description is out of the scope of the present work, but the main concepts, with particular attention on oxides growth, are summarized below.

Growth modes

There are basically three modes in which a thin film growth can develop:[112,113,115]

- **island growth** (or Volmer-Weber), in which small stable clusters nucleate on the substrate and grow in three dimensions to form islands. Which is, the deposited atoms or molecules are more strongly bound to each other than to the substrate. This growth mode is usually undesired since it leads to rough, nonuniform films.

- **layer-by-layer growth** (or Frank-Van der Merwe). Here stable nuclei tend to be two-dimensional, resulting in the formation of planar sheets. This growth mode is usually preferred over the others, since it ensures low boundaries density, the lowest surface roughness and the most precise control over the structure composition in the growth direction.

- **layer plus island** (or Stranski-Krastanov) in which, after forming some layers in a two-dimensional fashion, Frank-Van der Merwe growth becomes unfavorable and islands form.

The pertinent approach to describe the three modes of film growth is the consideration of surface energy (or, more precisely, of surface tension γ).[112] Assuming that there are no kinetic limitations and defining as γ_{SV}, γ_{SF} and γ_{FV} the surface tension of the substrate (S) - vapor (V) interface, the surface tension of the substrate-film (F) interface and the surface tension of the film-vapor interface, respectively, the island growth takes place if:[115]

$$\gamma_{SV} < \gamma_{SF} + \gamma_{FV} \tag{2.28}$$

whereas the condition for layer-by-layer growth is:

$$\gamma_{SV} \geq \gamma_{SF} + \gamma_{FV} \tag{2.29}$$

Straski-Krastanov growth can be interpreted as the situation in which Equation (2.29) initially holds but then during the growth, due for example to elastic strain, γ_{FV} progressively increases until the condition described by Equation (2.28) is fulfilled and the island growth mode is triggered.

Substrate temperature

In general, higher substrate temperature leads to an increase of both the critical aggregates size (i.e. the dimension of the smallest stable nuclei) and of the energy barrier during the nucleation process. Moreover, it promotes particles surface-diffusion. Therefore, the formation and the growth of few large crystallites or even monocrystals is favored over the stabilization of a large amount of small particles.[112,114] Moreover in the case of oxides, the presence of kinetic barriers to oxidation prevents the formation of the desired phase at low temperatures.[116]

Gas pressure

This parameter, which is particularly important in the case of the growth of oxides, has severe implications. From the one side, one needs an environment, i.e. the gas of choice and a certain working pressure, which ensures enough oxidation power at the deposition temperatures. On the other side, the high scattering

between the particles directed to the substrate and the gas molecules may be detrimental for the growth process, or even make it impossible. In particular in the case of MBE, a Knudsen regime (i.e. ballistic path) has to be maintained during the growth, in order to limit the reaction of the constituting elements before they reach the substrate and to maintain a precise control of the deposition rate. This sets a maximum operating pressure at $\approx 10^{-4}$ torr.[117] Furthermore, several in-situ monitoring tools (such as the RHEED system, see Section 3.2.1), need to be operated under good vacuum conditions. This makes the use of many common gases, (e.g. O_2 or N_2O) impossible for many compounds: for example, for the MBE growth of superconducting cuprates, thermodynamic considerations have demonstrated that a maximum temperature of ≈ 300 °C could be employed if O_2 was used, a value which is far below what is needed for an epitaxial growth (550-750 °C).[117] Therefore, other gases with stronger oxidation power must be employed: among them, ozone (O_3) has been successfully used for the growth of superconducting oxides by MBE.[116,118]

Growth rate

Thermodynamical considerations attribute to a low growth rate a similar role as to high substrate temperatures.[112,119] Moreover, a slow growth kinetics allows for a more precise in-situ control of the deposition process.

Choice of the substrate

Chemical and structural considerations must accompany the choice of the suitable substrate for the growth of a film. On the one hand the two phases should be chemically compatible in order to avoid the formation of secondary phases, on the other hand a strong interfacial bonding is wanted.[115,117,120] As the latter usually implies similar bonding types, oxide substrates are the typical choice in case of oxide thin films.

Another crucial parameter for the choice of the substrate is the film-substrate

lattice misfit, which can be defined as

$$f = \frac{a_f - a_s}{a_f} \times 100 \tag{2.30}$$

with a_f and a_s being the film and the substrate lattice parameters perpendicular to the growth direction (in the simplified case of tetragonal structures). Provided that a chemical bond occurs between the substrate surface and the film atoms at the interface, i.e. crystallographic continuity occurs, interatomic distances in the film in the direction parallel to the substrate surface (*in-plane*) are directly affected by the substrate lattice parameter. This induces a strain state whose magnitude is defined by f. The implications are numerous: (i) the preferred growth orientation is the one that ensures the minimum f, (ii) layer-by-layer growth conditions can tolerate a low amount of elastic strain, after which energy is released by the generation of islands or misfit dislocations, (iii) if conditions for epitaxial growth are maintained, one can induce an additional degree of freedom for tailoring the material functionalities represented by the elastic strain in the film.

Chapter 3

Experimental methods

3.1 Oxide Molecular Beam Epitaxy

Molecular Beam Epitaxy (MBE) is one of the most advanced techniques for the deposition of thin films. Extensively employed in the synthesis of semiconductors, it has been developed as a suitable technique for the synthesis of oxides especially in relation with high-temperature superconducting materials starting from the early 90's.[121–123] MBE technique has been employed for the synthesis of all the samples which has been studied in the present work.

Molecular Beam Epitaxy is based on the evaporation, obtained from resistive thermal sources (Knudsen cells) or from electron-beam sources, of metallic elements. The atomic flux is conveyed, by using appropriate geometry, in the direction of a substrate, where the cationic species combine in order to form the desired phase. Mechanical shutters, placed in front of each element source, are operated in order to provide each depositing specie in the correct order and amount. A highly reactive ozydizing gas, such as oxygen plasma or ozone, is employed for the growth of oxides. The use of molecular oxygen is normally prevented by the need to minimize scattering of the evaporated atoms in the background gas. This sets an upper pressure limit in the chamber in order of $\approx 10^{-4}$ Torr during the growth process, which is typically too low to obtain oxidation simply by molecular oxygen (see Section 2.3).[116,117]

Based on MBE, a particular growth technique called atomic-layer-by-layer MBE (ALL-MBE), has been developed.[118,124] In contrast with the classical deposition techniques, which are based on the simultaneous deposition of all the different species constituting the growing phase, in ALL-oxide MBE only the species which serve for the deposition of a single atomic layer are allowed to reach the film surface. Once the atomic layer is formed, if the subsequent atomic layer has a different composition then the atomic flux of the specific cations is varied accordingly by means of mechanical shutters; afterwards, the deposition of the next atomic layer starts, and the growth eventually proceeds by forming each atomic layer at a time.

The main advantages of the oxide MBE method can be summarized as follows:

- **Great versatility in the choice of the compound.** A typical MBE system is equipped with several (ten, in our case) independent metal sources, which can be used in order to realize a number of compositions without any change in the chamber configuration;

- **Lowest undesired cationic intermixing** between layers as a consequence of surface impingement by the incoming particles. The particles kinetic energy can be estimated in ≈ 0.1 eV, much lower than the usual values for the other synthesis method (e.g. ≈ 10 eV for the pulsed laser deposition (PLD) process);

- **Excellent growth control.** The low gas pressure used for the growth process makes it possible to employ several surface analytical tools such as reflection high-energy electron diffraction (RHEED), low energy electron diffraction (LEED) etc. which provide crucial informations on the growth process in real time. This, together with a very low growth rate, allows for an excellent deposition control and for readily correcting the growth parameters (e.g. growth temperature, pressure, composition) in-situ;

- **Atomic resolution.** In the particular case of ALL-oxide MBE, one can carefully select the composition of each atomic layer. Thanks to this, one can

not only realize heterostructures very precisely and with minimized thickness, but even engineer the composition at the sub-unit cell level.

The MBE method requires a very careful control of the growth parameters, in particular with respect to the ratio between the cations being deposited, which is directly dependent on the timing of each source shuttering. This makes the MBE growth process particularly challenging in comparison with other deposition techniques, in which instead the stoichiometry is already defined at the material source level (e.g. the target in pulsed laser deposition or sputtering). Even a light off-stoichiometric growth would eventually result in the presence of undesired precipitates in the film. Appropriate calibration tools, such as quartz crystal microbalance (QCM) are used to measure the source fluxes prior to growth but, due to their limited accuracy, a continuous tuning of the growth parameters during the process is required. For this purpose, several monitoring tools (e.g. RHEED) are employed.

The MBE (and especially the ALL-MBE) technique is particularly suited for the realization of multilayered systems, in which different phases are stacked on top of each other, and of superlattices, in which a fixed structure (superlattice unit, having typical thickness of few nanometers), is repeated for a predefined number of times.

3.1.1 Setup description

Aim of this section is to provide a detailed description of the oxide MBE setup which has been used to synthesize the samples for this project. For more details please refer to Ref. 125.

The oxide MBE system which is installed at MPI-FKF has been designed and built by DCA Instruments (Turku, Finland) according to a cluster tool modular configuration similar to other oxide MBE systems.[126] It is equipped with two growth chambers, identical in construction and capable of working in parallel without interference. Two other smaller chambers, i.e. a load-lock and a storage chamber, are used for samples loading (and unloading) and storage, respectively.

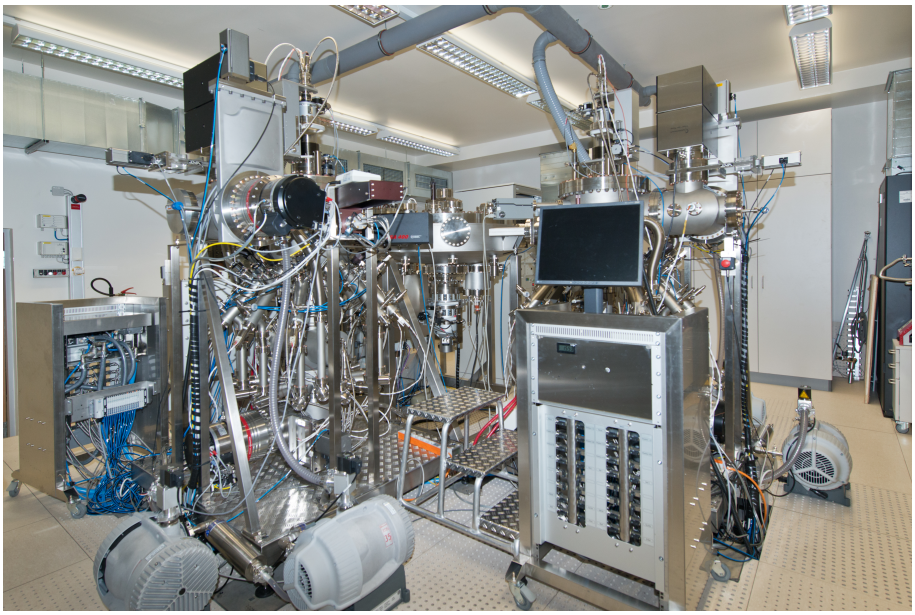

Figure 3.1. Photo of the dual chamber oxide MBE system installed at the Max-Planck Institute for Solid State Research. Reproduced with permission from Ref. 125.

A ultra-high vacuum central distribution chamber (CDC) serves for the fully automated transfer of the samples between the load-lock chamber, the storage chamber and the two growth chambers.

A photo of the MBE system is shown in Figure 3.1.

Each deposition chamber, whose sketch is provided in Figure 3.2, is equipped with 10 water cooled spools, positioned symmetrically around the chamber line, each of whom houses a resistive heated elemental source and a software-actuated pneumatic shutter for the control of the flux. In addition, each growth chamber is equipped with a four pockets electron-beam evaporator directly located below the substrate, which can be used for evaporating refractory metals. The growth chambers are provided with an internal liquid nitrogen cooled cryogenic panel surrounding the substrate area, and their geometry is optimized for a maximum substrate size of 3". The substrate manipulator has motorized full rotation and vertical translation. Pumping is provided by an ion-pump and a corrosive version turbo-pump with scroll-type backing pump. A differential pumping module, placed underneath the growth chamber, is connected to each of the system elements (e.g.

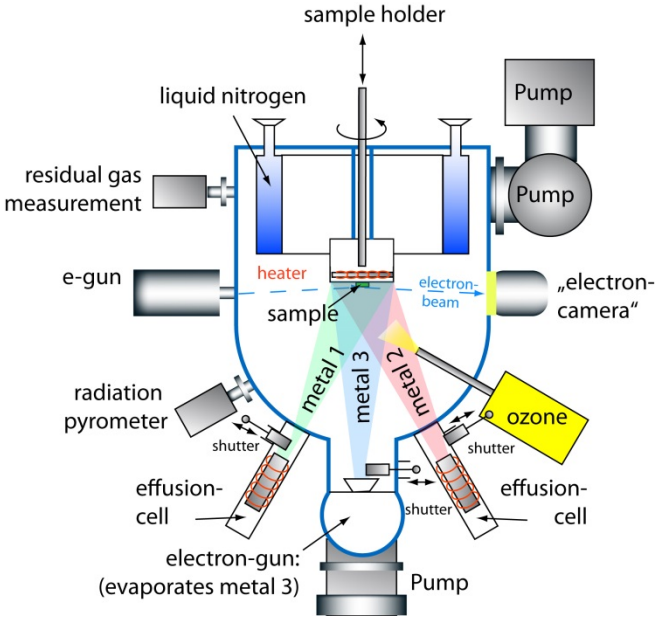

Figure 3.2. Sketch of the MBE growth chamber. Reproduced with permission from Ref. 125.

growth chamber, sources, calibration and monitoring tools). Chamber pressure and gas composition are measured by several ion gauges (strategically positioned in the growth and in the differential modules), and by a residual-gas analyzer (RGA) serving the growth chamber, respectively. The modular configuration allows for insulating each element (e.g. each elemental source) from the growth chamber by the use of gate valves. This way, using the differential pumping module one can vent and pump each of system elements without breaking the vacuum in the growth chamber. This makes the maintenance operations extremely efficient, and allows the growth processes to be carried out even when some maintenance is in progress.

3.1.2 Growth process

Prior to the deposition process, each source is heated up from its idle point to a temperature corresponding to a convenient element vapor pressure, which ensures the desired growth rate (typically few Å/min). Each source deposition

rate is calibrated via a QCM system. After the calibration, the substrate is heated by a SiC resistive element (operating up to 1200 ℃); the substrate temperature is controlled by a radiation pyrometer. A nozzle, positioned in front of the substrate, ensures the delivery of ozone from the ozone delivery system.

Distilled ozone is produced by a plasma generator system and is stored in liquid form in an insulated glass still ($T \approx -140$ ℃), where it is absorbed by silica gel spheres. The still temperature is adjusted by means of liquid nitrogen cooling and a heating element: this allows for a controlled evaporation of the gas during the delivery to the chamber. A typical pressure in the growth chamber during a deposition is $\approx 10^{-6} - 10^{-5}$ Torr. Even though pure ozone is produced, due to its extremely short life-time, radical oxygen and molecular oxygen form very easily once the gas is delivered to the chamber, therefore the growth is eventually performed in a mixture of the different species. The delivery efficiency is crucial, since the maximum pressure is limited by two factors: (i) the requirement of a ballistic path for the atoms moving from the source to the substrate, (ii) technological limitations (e.g. pumping system efficiency, possible oxidation of the metallic components of the system). In Figure 3.3, an example of the gas composition in the growth chamber during a growth process is shown: one can see that a mixture of molecular oxygen (32 u), radical oxygen (16 u) and ozone (48 u) is present, together with impurity gases such as hydrogen (2 u) and nitrogen (28 u).

The growth process is based on the ALL-MBE method: once an atomic layer is formed, the flux of the corresponding element is interrupted and is subsequently followed by the deposition of the next layer. This process is made possible by an alternated actuation of the sources shutters by a pneumatic system which is software-controlled. Note that the shutters actioning time is in the order of $\approx 10^{-1}$ s.

Each growth chamber is equipped with a k-space kSA 400 RHEED system, whose electron gun is operated between 25 keV and 30 keV with typical emission filament current ≈ 1.5 A. A phosphor screen collects the diffracted image which, by means of a CCD-camera, is sent to a computer and further analyzed by a specific acquisition and analysis software. Based on the analysis of the RHEED patterns,

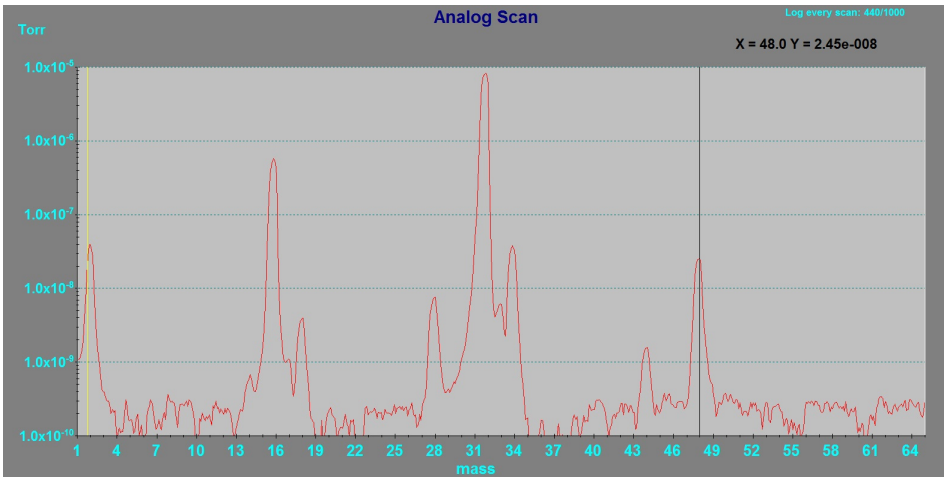

Figure 3.3. Typical gas composition in the growth chamber as obtained by the Residual Gas Analyzer (RGA) system. The partial pressure of each gas is shown as a function of its molecular mass.

the operator can optimize the growth parameters (i.e. substrate temperature, ozone pressure and shutters timing) in real time.

I personally took part in the system installation and optimization during the time of the present project, and I have been responsible for the growth of most of the samples which have been studied.

Substrate preparation. The usual substrate preparation procedure comprises cleaning in ultrasonic bath for about 15 min first in acetone then in isopropanol. Afterwards, a suspension of strontium ruthenate ($SrRuO_3$) in isopropanol is routinely applied on the backside of the substrates (simply using a brush) prior to the loading in the MBE chamber. This allows one to obtain, upon ispropanol evaporation, a thin layer of black $SrRuO_3$ sticking on the backside of the substrate whose purpose is to adsorb the radiation coming from the heater during the MBE process, thus improving the heating efficiency. The substrates are fixed to the substrate holder (*puck*) by using a tantalum wire. Usually one single substrate is mounted on each puck but, for some specific experiments, pucks which are able to host up to 4 substrates can also be used. After the growth, the $SrRuO_3$ layer is removed by simple wiping with a wet lab tissue.

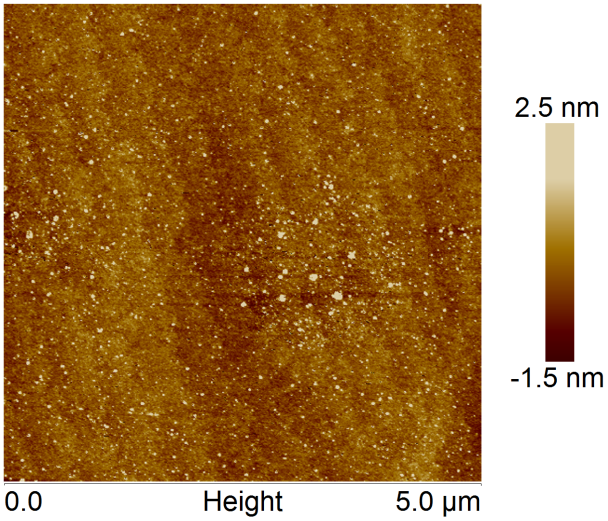

Figure 3.4. Representative AFM micrograph for a $LaSrAlO_4$ "as received". Root mean squared (R_{ms}) roughness is 0.5 nm.

The typical size of the substrates that has been used for the growth processes is 10×10×0.1 mm. Single crystal substrates of different oxides have been employed (see also Section 4.1.1). Most of them have been provided by Crystec GMBH, but in same cases, due to the limited availability, also substrates from Crystal GMBH have been used for process testing or during the phases of growth optimization. In Figure 3.4, a representative AFM micrograph for a $LaSrAlO_4$ "as received" is presented.

3.2 Diffraction

Diffraction techniques are widely implemented for the study of the structure of thin films, both as in-situ monitoring tools and as analytical techniques. An exhaustive theoretical explanation of crystals diffraction can be found in Refs. 127, 128.

Conditions for crystal diffraction are fulfilled when the radiation wavelenght λ is comparable to the interatomic distance, therefore X-rays or an electron beam in the eV-keV energy range are suitable. In particular, both are extensively used for

ex-situ analysis (X-ray diffraction, selected area electron diffraction in transmission electron microscopy), whereas the last in particular can be easily implemented for the in-situ monitoring of the growth process.[129]

Diffraction techniques are based on the analysis of the constructive interference pattern formed by radiation which interacts elastically with a crystal structure. Given a wave incident a crystal (having wave vector $\vec{k}^0$) and the elastically scattered beams (wave vectors $\vec{k}$, with $|\vec{k}^0| = |\vec{k}|$), constructive interference occurs in those directions by which the scattering wave vector $\Delta\vec{k} = \vec{k} - \vec{k}^0$ corresponds to a vector of the crystal reciprocal lattice $\vec{G}$ ($\Delta\vec{k} = \vec{G}$). This allows for retrieving precise informations about the crystal structure once the diffraction pattern is given. A particularly useful tool in this sense is provided by the Ewald sphere, which is centered on the crystal and has radius $|\vec{k}| = 2\pi/\lambda$: the intersection of the diffracted beams with the Ewald sphere directly represents the reciprocal lattice.[130]

3.2.1 In situ monitoring by reflection high-energy electron diffraction

In-situ monitoring techniques are based on the quasi two-dimensional diffraction of radiation from the growing thin surface, by which one can get informations about the surface composition and its morphology. The most common techniques are low energy (LEED) and reflection high-energy (RHEED) electron diffraction. In LEED, electron energy between 10-500 eV (wavelenght $\approx 10^{-1} - 10^{0}$ Å), having a penetration depth of only few Å, is used in a perpendicular geometry whereas, in case of RHEED, typical electron energies are between 10-100 keV (wavelenght $\approx 10^{-2}$ Å). Here, surface sensitivity is achieved by using grazing incident angles (0.1°to 5°). Such a geometry makes the RHEED technique particularly easy to be implemented in growth chambers.[129]

Notably, the reciprocal lattice representation of a 2D-crystal (surface) is an array of rods, which intersects the Ewald sphere in points.[115,129] The presence of imperfections, such as roughness or substrate steps, together with instrumental limitations such as imperfect collimation or wavelenght spread, transforms the interference spots into the streaks which are usually detected.[115,131,132]

The informations that can be inferred from a RHEED pattern can be summarized as follows:

- **Two-dimensional ordering.** If the growing surface is flat and has crystalline order, then diffraction streaks form. It is worth mentioning that, especially in the case of ionic crystals, surfaces are not a simple truncation of the bulk structure; rather, they reconstruct in order to minimize the surface energy related to the presence of dangling bonds. As a consequence, a periodic rearrangement of the atoms i.e. a superstructure, whose periodicity is larger than the atomic planes distance, may appear yielding an additional diffraction pattern (more densely spaced than the fundamentals reflections).[129] In Figure 3.5, a typical RHEED pattern for La_2CuO_4 is reported.

- **Surface coverage.** The surface rougness variation during the growth can be investigated by recording the time-dependent intensity of the diffracted beam, which is known to oscillate according to the film surface coverage.[112,129] Usually, for this analysis, the specularly reflected beam (specular spot), which has the highest intensity, is considered (for an example, please refer to the time evolution of the RHEED specular spot during a typical growth of La_2CuO_4, which is reported in Figure 4.4).[122]

- **Formation of 3-D crystallites.** In the case of formation of islands on the film surface, electron may pass through such structures: in this case, the surface diffraction pattern is replaced by a 3-dimensional transmission pattern characterized by spots instead of streaks.[129] In this case, one can retrieve informations about the islands crystal structure (thus about their composition) by analyzing the characteristic diffraction pattern (see for example Figure 4.3).

3.2.2 X-ray diffraction

X-ray diffraction is commonly implemented for the study of the 3D-crystal structure of thin films. In this case, the diffraction condition can be simplified by

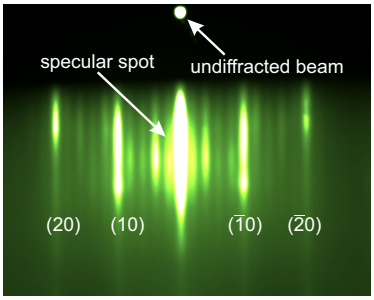

Figure 3.5. Example of RHEED pattern for La_2CuO_4. One can notice the presence of additional diffraction streaks between the main diffraction lines, which are ascribable to surface long-range atomic order (superstructure).

thinking of the diffracted wavefront as having been specularly reflected off atomic planes having interatomic distance d.[115] Constructive interference then occurs if the reflected beams are in phase, i.e. their path difference is an integral multiple of the beam wavelength λ. With θ being the angle between the incoming waves and the crystallographic planes, the condition for constructive interference is expressed by the Bragg equation:

$$2d \sin\theta = n\lambda \tag{3.1}$$

From the θ angles which give constructive interference, the interatomic distance can be obtained.

In order to retrieve a more precise evaluation of the d lattice parameter, refinement via the Nelson-Riley function, which takes into account possible sample misalignments, can be used.[133] Here, the lattice parameter is defined by the y-intercept of the linear fitting obtained by plotting d as a function of the Nelson-Riley function

$$\left(\frac{\cos^2\theta}{\sin\theta} + \frac{\cos^2\theta}{\theta}\right) \tag{3.2}$$

In the particular case of thin films, together with the stacking of the atomic planes, other types of ordering exist, giving rise to diffraction effects. In particular, additional peaks are present around the main Bragg peaks: they are the Laue

fringes, which stem from the overall crystalline orderer volume and whose distance is linked to the sample thickness, and the superlattice peaks, which reflect the presence of an alternation of different phases in the case of periodic multilayers (see for example Figure 4.34).

These additional peaks can be treated with the following formula:[134]

$$\frac{2\sin\theta}{\lambda} = \frac{1}{\bar{d}} \pm \frac{n}{\Lambda} \tag{3.3}$$

in which n is an integer that labels the order of the satellite peak around the main Bragg peak and Λ is the modulation lenght (e.g. the film thickness or the superlattice unit thickness). In the case of a single phase film, in which only the Laue fringes are present, we simply have $\bar{d} = d$. For the case of superlattices, the superlattices fringes must be analyzed by taking

$$\bar{d} = \frac{\Lambda}{N_A + N_B} \tag{3.4}$$

Here, N_A and N_B are the number of atomic planes of material A and B in a superlattice unit, respectively.

The diffractometer used for the investigations of the samples during this project (model Bruker D8) uses a Bragg-Brentano reflection geometry equipped with a monochromator and a Cu-filament source (λ = 1.54060 Å). In such a geometry, a typical scan, called $2\theta/\omega$, is performed by changing both the source and detector positions with respect to the sample: the incident angle ω and the diffracted angle 2θ are coupled in order to ensure the optimal beam collimation thus maximum intensity.

3.3 X-ray reflectivity

Analysis of X-ray reflectivity (XRR) is a powerful tool in order to get informations about thin films morphology. An exhaustive description of this technique can be found in Refs. 135, 136. This technique is based on the specular reflection of X-rays at grazing incident angles. In such a configuration, for angles larger than the critical angle, the incident beam is partially reflected and partially refracted by

the film surface: the path difference between the reflected and the refracted beam, which exits the film after further reflection by the substrate, gives rise to interference. As a consequence, one can observe an oscillating intensity behavior of the outcoming beam as a function of the incident angle (the so-called Kiessig fringes), with maxima occurring when the condition for constructive interference is fulfilled. By analyzing the Kiessig fringes, one can easily obtain the film thickness (up to ≈100 nm) in the case of single phase film using the approximated relation:[136]

$$d \simeq \frac{\lambda}{2\Delta\alpha} \tag{3.5}$$

with $\Delta\alpha$ being the distance between two consecutive minima or maxima and λ being the wavelength of the incident beam. Based on a similar approach, one can perform analysis of multilayered structures, given that each constituting phase is characterized by different density thus different refraction index. In this case, the analysis of the reflectivity curve requires the use of simulations, which are typically based on the Parratt equation (see for example Figure 4.35).[137]

By doing this, one can not only get informations on the total and the single layers thickness, but also on the surface and the interface roughness, parameters which can be retrieved by analyzing the intensity loss upon beam-sample interaction (in particular, the reflected beam intensity decreases more rapidly for increasing incident angles in the case of rough interfaces).

3.4 Atomic force microscopy

Atomic force microscopy (AFM) is a technique for the atomic-scale analysis of the surface morphology, which provides useful informations about the quality of the samples.[138] A smooth film surface is usually the result of layer-by-layer growth, absence of secondary phases and, in the case of multilayers, sharp interfaces. On the contrary, the composition of secondary phase outgrowths can sometimes be inferred by simply analyzing their morphology (see for example Figure 4.3). AFM analysis has been routinely performed on our samples, as a complementary tool to RHEED for surface analysis.

AFM is based on the forces (such as Van der Waals, electrostatic forces) which build up between the film surface and a sharp tip mounted at the end of a cantilever spring.[112] While moving in plane thanks to a piezoelectric controller, the sharp tip follows the morphology of the surface and by doing so it deflects the cantilever. A collimated laser beam which is reflected by the top side of the cantilever (in correspondence of the sharp tip) into a detector allows to quantitatively map the height variations of the surface (i.e. the roughness).

AFM can operate in *contact mode*, in which repulsive forces generated by the contact between tip and sample are measured, *non-contact mode* or *tapping mode*. In the second mode an oscillation of the tip at its resonance frequency is induced: tip-surface interaction tend to disturb such oscillation, and the system adjustes the tip-surface distance in order to maintain a constant frequency. From here, informations about the surface morphology are obtained. In the third mode, called *tapping mode*, the oscillation frequency is increased and an alternated tip-sample contact is realized. This way, more accurate informations are retrieved with respect to the non-contact mode, while a less destructive (for the tip) situation is realized compared to the contact mode.

For our measurements, Digital Instruments atomic force microscope with Nanoscope III controller, operated in *tapping* mode, has been used.

Together with surface imaging, also quantitative informations about the roughness can be obtained, such as:

- *root mean squared roughness,* R_{ms}

$$Rms = \sqrt{\frac{1}{L}\int_0^L Z(x)^2 dx}$$

- *aritmetic average roughness,* R_a

$$Ra = \frac{1}{L}\int_0^L |Z(x)| dx$$

- *maximum roughness,* R_{max}

$$R_t = max[Z(x)] - min[Z(x)]$$

with L being the evaluation length and $Z(x)$ the profile height function.

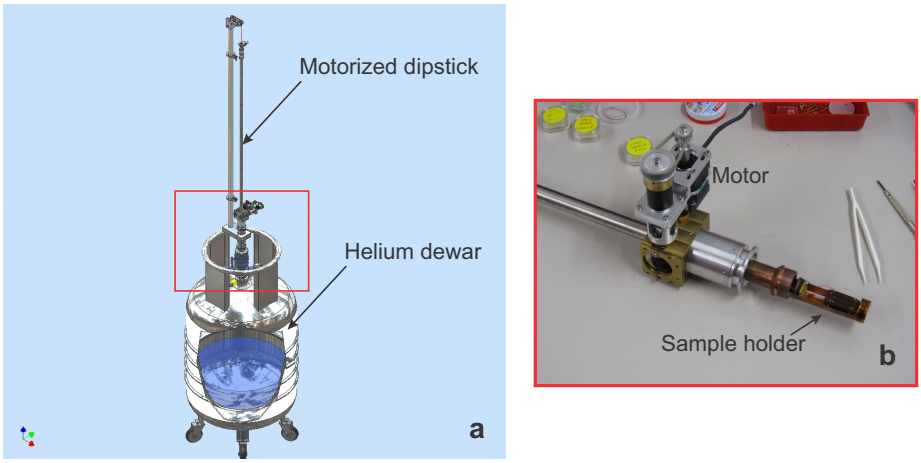

Figure 3.6. In (a), schematic representation of the home-built system for low temperature resistivity and mutual inductance measurements (image by G. Cristiani). In (b), photo of the sample holder, which is situated at the tip of the dipstick (see red rectangular in (a)).

3.5 Measurements of superconducting properties

In order to detect the superconducting properties of the samples, measurements have been performed at temperatures down to liquid helium temperature ($\approx$ 4 K). For this purpose, a home-built system has been realized. Samples are mounted on the tip of a metal stick and are deeped into a liquid helium dewar. The movement of the stick is motorized and controlled via software (Labview) in order to maintain the desired rate of temperature variation (typically about 0.1 ℃/s). The temperature is measured by a diode-type temperature sensor which is placed right under the sample holder, connected to a Lakeshore 340 Temperature Controller. Such a system allows for the simultaneous measurement of the electrical and magnetic properties of the samples (details are given below).

I personally contributed in building parts of the device.

3.5.1 Mutual inductance

This measurement is based on the detection of the diamagnetic transition of a material entering the superconducting state and has been routinely used in order to define the transition temperature T_c. A full explantion of the technique can be found in Ref. 30.

Two Cu coils (drive and pick-up, respectively) facing each other are positioned above and below the sample (transmission geometry). An alternated current (60 μA at a frequency of f=1.6 kHz) is driven through the drive coil, generating an oscillating magnetic field: at temperatures above the superconducting transition temperature, the superconducting material has no screening effect on such a field therefore a voltage is induced at the pick-up coil ends. When the film becomes superconducting (diamagnetic), the magnetic field is screened and the measured induced voltage turns to zero.

The setup is equipped with a SR850 DSP lock-in Amplifier and two Agilent 34401A Multimeter.

This type of measurement is particularly convenient as it does not require the deposition of metal contacts on the sample surface, providing an immediate measurement tool, right after taking the sample out of the growth chamber.

3.5.2 Electrical conductivity

Electrical conductivity measurements have been performed in Van der Pauw geometry.[139] 0.5x0.5 mm^2 platinum or gold electrodes are first deposited by sputtering or evaporation on samples corners. Contact spheres are pressed on the electrodes by a spring-loaded probe (pogo pins), and DC measurements are carried out using a Keithley 2000 multimeter and a Keithley 2400 sourcemeter. In such a configuration, a DC current, typically in the range 1 μA to 100μA is driven in the sample through two contacts placed on the same side of the sample, whereas the voltage drop V between the other two contacts is measured on the opposite side (parallel configuration). By employing such a 4-points measurement configuration, one can exclude the contribution of the voltage drop due to the flow of

the current through the contacts.[115] In order to rule out any possible contribution due to thermopower effects, current direction is continuously switched (with 1 Hz frequency) and the resistance is calculated as follows:

$$R = \frac{2V}{I^+ + I^-} \tag{3.6}$$

where I^+ and I^- represent the current values which are applied in sequence with opposite directions. During the measurements, resistance values are recorded as a function of temperature at a fixed time interval (typically 500 ms).

The analysis of the resistivity data has been routinely performed in agreement with Ref. 31. The resistivity curves $\rho(T)$, which have been obtained by the measurements, are fitted using a quadratic polynomial function $\rho_{fit}(T) = a + bT + cT^2$ in the temperature interval 50 K $<$ T $<$ 270 K, or in any case in the T region in which $\rho(T)$ exhibit metallic behavior. By intercepting $\rho_{fit}(T)$ with three curves obtained as $0.9\rho_{fit}(T)$, $0.5\rho_{fit}(T)$, $0.1\rho_{fit}(T)$, three different superconducting transition temperature values ($T_{\mathrm{c},0.9}$, $T_{\mathrm{c},0.5}$ and T_{c}, respectively) are defined (see Figure 3.7).

Notably, the width of the superconducting transition ($T_{\mathrm{c},0.9}$-T_{c}) can be related to the sample compositional homogeneity and to the amount of structural defects e.g. presence of misfit dislocations, secondary phase precipitates.[31]

3.6 Transmission Electron Microscopy

Transmission electron microscopy (TEM), together with the analytical techniques such as energy-dispersive X-ray spectroscopy (EDXS) and electron energy-loss spectroscopy (EELS) provides structural information with atomic layer resolution. Therefore, it represents a very important tool for our analyses in order to correlate the functional properties with the local interface structure. For this reason, a representative selection of samples has been analyzed by the Stuttgart Center for Electron Microscopy at the Max-Planck Institute for Solid State Research.

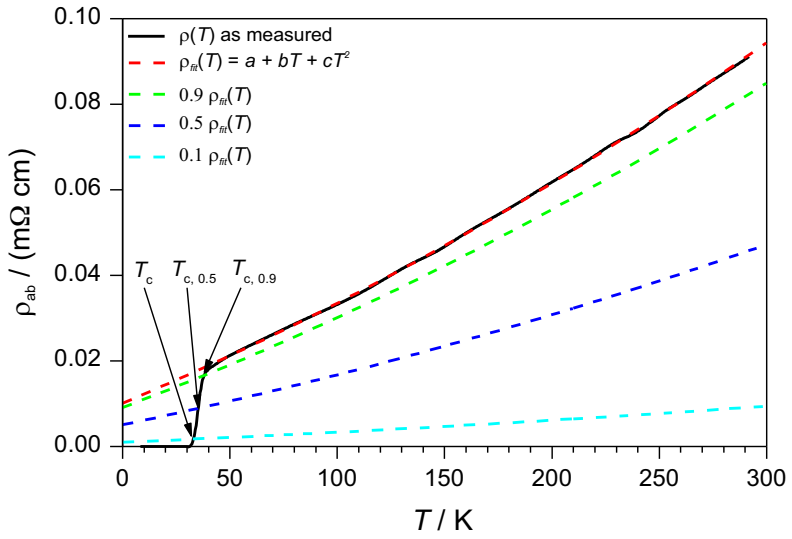

Figure 3.7. Definition of T_c from the resistivity curve. Taken from Ref. 140.

In scanning transmission electron microscopy (STEM), thin specimens, prepared by mechanical tripod polishing and argon ion milling at liquid nitrogen temperature, are traversed by a highly energetic electron beam (up to 200 keV), whose spot size ($\leq$ 1Å) is small compared to the distance of neighboring atom columns.

Different STEM techniques have been applied. In particular, high-angle annular dark-field (HAADF) has been employed for imaging. In this technique, which is also called Z-contrast imaging, the image intensity of individual atomic columns is determined by the atomic number Z of the elements constituting the column ($I \propto Z^{1.5-1.8}$) and the specimen thickness.[141] Therefore, this image mode is particularly useful for analyzing cationic positions and distribution (in particular for heavy elements), as well as to provide information about the presence of structural imperfections.

Besides imaging, spectroscopic methods have been employed. By EELS one analyzes the energy loss resulting from the inelastic interaction between the incoming electron beam and the specimen. The EELS spectrum contains information about the chemical composition of the atomic columns.[142] Moreover, one can also

investigate the electronic structure (e.g. electronic charge carrier concentration, valence state).[143,144] Complementary informations about the chemical composition can be obtained by EDXS, which is based on the analysis of the X-ray radiation emitted by the atoms upon interaction with the electron beam.

For the electron microscopy and spectroscopy measurements, a JEOL ARM 200CF microscope equipped with a cold field-emission electron source, a DCOR probe corrector (CEOS GmbH), a large solid angle SDD-type JEOL Centurio EDXS detector, and a Gatan GIF Quantum ERS spectrometer have been employed. The typical operating voltage is 200 kV, with a semi-convergence angle (α) of 21 mrad, resulting in a probe size of 0.8 Å (1 Å for the analytical analysis). HAADF images have been acquired using a $109 - 270$ mrad collection angle. A collection semi-angle (β) of 68.5 mrad has been used for EELS measurements. The STEM analysis has been carried out at specimen regions where the thickness is below 30 nm ($t/\lambda < 0.4$ as measured by low-loss EELS using a log-ratio method).

A detailed description of TEM techniques can be found for example in Ref. 145.

Chapter 4

Results and discussion

4.1 Single phase films growth optimization

The first step towards the realization of heterostructures for our study has been the optimization of the growth process of single phase systems. In the following sections, the main findings and results are summarized.

4.1.1 Growth of lanthanum cuprate

Lanthanum cuprate (La_2CuO_4) is, due to its layered structure, an excellent oxide for atomic-layer-by-layer growth by MBE as already demonstrated in the past.[146,147] Nevertheless, its synthesis presents several critical aspects related to the narrow stability window of the compound under typical MBE growth conditions and to the need of a very precise adjustment of the stoichiometry. The latter is related to the extremely high sensitivity of high-temperature superconductivity towards the presence of secondary phases and, in general, towards crystallographic disorder.

Optimal growing conditions. It has been found that severe oxidizing conditions (i.e. high ozone pressure, together with relatively low growth temperatures) are required in order to obtain the correct La_2CuO_4 phase. This has to be attributed in particular to the oxidation state of Cu (+2) in La_2CuO_4 which indeed

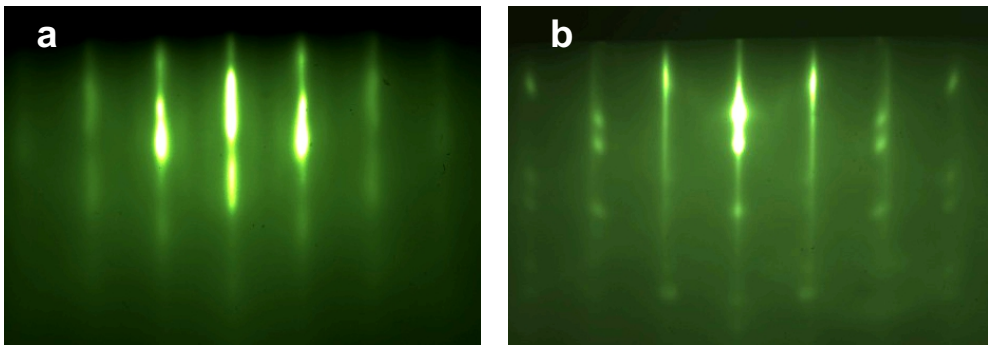

Figure 4.1. a) RHEED pattern (along the (100) direction) for La_2CuO_4 showing increased roughness due to island growth at low deposition temperatures ($T \leq 590$ °C). b) RHEED pattern for La_2CuO_4 showing phase decomposition due to high temperature ($T \geq 660$ °C).

defines the stability limits for the compound.[117] However, by excessive temperature decrease (typically below 600 ℃) layer-by-layer growth mode tends to be substituted by islands growth; at the same time, the pressure in the MBE chamber cannot be deliberately increased due to technical and process limitations (see Section 3.1). The primary importance of these aspects can be inferred by analyzing Figure 4.1, in which two RHEED patterns are shown, corresponding to (a) low-temperature growth, and to (b) decomposition due to too high growth temperature (i.e. low degree of oxidation), respectively. Both are characterized by spots which are indicative of poor crystalline properties. In particular for the first case such spots are mainly aligned to the main streaks, indicating the presence of 3-dimensional islands of La_2CuO_4. In the second case instead one can observe that RHEED diffraction spots, whose spacing does not correspond to the typical diffraction figure of La_2CuO_4, are present, suggesting that secondary phases caused by phase decomposition are formed (see Section 3.2.1 for a complete description of the RHEED diffraction patterns). Notably, the two growth processes were carried out by employing the maximum pressure allowed in the system ($P = 3 \times 10^{-5}$ Torr) and by using only slightly different temperatures (590 °C and 660 °C, respectively). This testifies the narrow window in which the compound can be correctly synthesized.

Upon optimization, which involved also some modifications of the ozone delivery system (e.g. replacement of the delivery pipes, modifications of the pumping system), we were able to obtain single phase defect-free La_2CuO_4 and $La_{2-x}Sr_xCuO_4$ (with various doping levels). The growth parameters were commonly set as $P \approx 2 - 3 \times 10^{-5}$ Torr and $T \approx 600 - 650$ ℃.

Stoichiometry adjustment. As mentioned above, the growth optimization requires not only to find the optimal thermodynamics conditions, but also to adjust the stoichiometry correctly (in particular the La/Cu ratio). Due to the limited accuracy of the calibration of the cation fluxes and due to the natural oscillations of the fluxes during the growth process, the fine tuning has to be manually operated during the growth, relying on the informations provided by the RHEED pattern. Even light off-stoichiometry would eventually result in the growth of secondary phases. In Figure 4.3 we report the RHEED patterns corresponding to a growth in Cu excess (a), La excess (c), and optimal stoichiometry (f). For an immediate comparison, the corresponding AFM micrographs obtained from the analysis of samples resulting from such growth conditions are reported. The first case (Cu-rich) is the most severe, since we found that, once Cu-based secondary phases are formed, they cannot be dissolved by any further adjustment: the final functional properties of the sample, also due to the electrically conductive character of such oxides, are deeply affected. In order to avoid the formation of these clusters, one needs to adjust the stoichiometry promptly, prior to their appearance in the RHEED. Usually, a sign of a Cu-rich growth is the progressive reduction of the RHEED oscillation intensity, together with the observation of a peculiar superstructure (Figure 4.2). The second case instead (La-rich), can usually be recovered (i.e. the particles can be dissolved), as long as the dimensions of the outgrowths is limited, by decreasing the La/Cu ratio. In any case, lanthanum-based oxide phases are normally not conductive so their presence in the film, if limited, is acceptable. Apart from the formation of spots in the RHEED, indication of La-rich growth is given by a weakening of the superstructure. In (e), finally, the RHEED pattern of stoichiometric La_2CuO_4 is shown: one can clearly

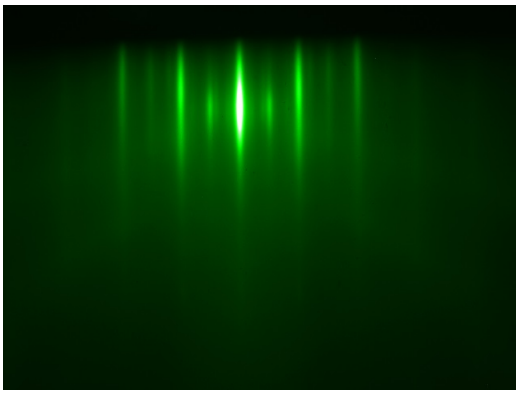

Figure 4.2. RHEED pattern (along the (100) direction) for off-stoichiometric (Cu-rich) La_2CuO_4 (to be compared with the RHEED pattern of La_2CuO_4 which is grown in optimal conditions reported in Figure 4.3f). If not promptly corrected with an adjustment of the Cu/La ratio, this pattern would eventually evolve in the one shown in Figure 4.3a.

see the typical superstructure (4 lines between the main diffraction streaks) which represents one of the most important indications concerning the growth quality. The resulting AFM micrograph shows a smooth surface, whose R_{ms} roughness is comparable with the substrate roughness (about 0.5 nm).

Choice of the substrate. As described in Section 2.3, the appropriate choice of the substrate is of primary importance in order to obtain epitaxial growth. Chemical compatibility and a limited lattice mismatch between substrate and film are required. In principle, a wide range of oxide substrates is suitable for the growth of La_2CuO_4 (whose lattice parameter can be approximated in 3.801 Å by considering the La_2CuO_4 lattice as pseudotetragonal having lattice constant $a_0 = (a^2 + b^2)^{1/2}$).[146] An exhaustive list of substrates having suitable lattice parameter can be found in Ref. 148, but it has been demonstrated that the best superconducting properties for La_2CuO_4 are obtained for epitaxial films grown on (001) oriented $LaSrAlO_4$ (lattice parameter $a = 3.754$ Å), which ensures the growth of a c-axis oriented structure under compressive strain ($f = -1.2\%$, see Section 2.3). It is well established that these conditions lead to the highest T_c for the La_2CuO_4 system.[82,149] Although some tests have been performed also on

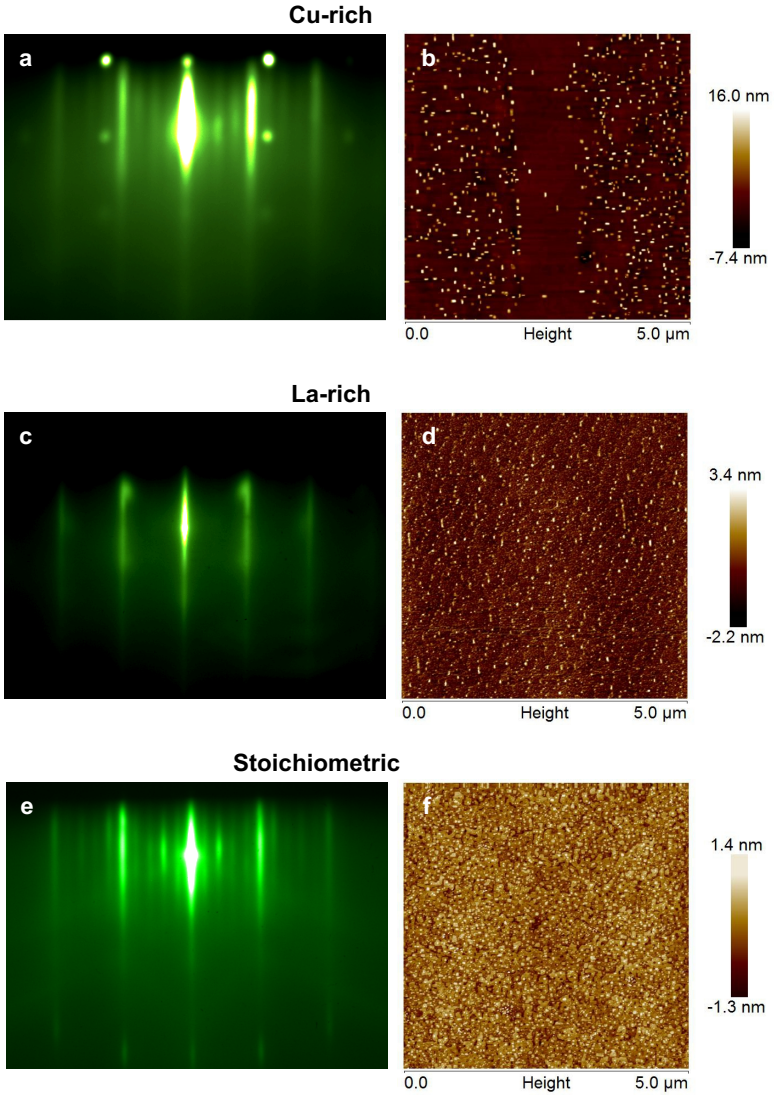

Figure 4.3. RHEED pattern for the different situations which may be encountered during the growth of La_2CuO_4 as a consequence of a different stoichiometry ratio (La/Cu) (panels a, c, e). The resulting final film topography, as measured by AFM, is reported for comparison in panels (b), (d), (f).R_{ms} roughness values are 2.7 nm, 0.9 nm and 0.5 nm for the micrographs shown in (b), (d), (f), respectively.

$SrTiO_3$ (100) and LSAT ($La_{0.18}Sr_{0.82}Al_{0.59}Ta_{0.41}O_3$) (100), $LaSrAlO_4$ (001) has been far the most used substrate in the present work and all the results reported here have been obtained for films grown on it. In figure Figure 3.4, a representative AFM micrograph for $LaSrAlO_4$ is shown.

Final properties

At the end of the optimization phase, we were able to routinely obtain defect-free, epitaxial La_2CuO_4 and $La_{2-x}Sr_xCuO_4$ with various thicknesses, up to ≈ 100 nm. Notably, we were able to synthesize superconducting $La_{2-x}Sr_xCuO_4$ down to 2 u.c. having $T_c \approx 20$ K which, up to date, represents the record for $La_{2-x}Sr_xCuO_4$ films without capping layers.[150–152]

In Figure 4.4, the time evolution of the specular spot oscillation for optimally grown LCO is reported. Each oscillation maximum corresponds to the formation of a complete La_2CuO_4 block (i.e. at the end of the deposition of a CuO_2 plane), whereas the minima, in which the film has maximum roughness, is reached at the end of the LaO layers deposition. Oscillation intensity is nicely maintained throughout the growth process.

In Figure 4.5, $2\theta/\omega$ XRD fullscan of a La_2CuO_4 film is reported, showing pronounced diffraction peaks up to the (00 14) index, indicative of high crystalline order. In Figure 4.6, a plot of the T_c values as a function of the c-axis parameter (calculated from XRD measurement according to Equation (3.2)) is presented. Films have been grown on different substrates and have various thickness. One can see that, in agreement with literature (cf. Section 2.1.2) an approximate linear relation is maintained between c and T_c.

A representative AFM micrograph is reported in Figure 4.3f.

We were able to obtain superconducting $La_2CuO_{4+\delta}$ with T_c up to ≈ 40 K by interstitial oxygen intercalation upon ozone post-annealing in the growth chamber ($P \approx 4 \times 10^{-5}$, $T \approx 650$ °C for about 15 minutes, followed by ozone cooling down to room temperature). Insulating La_2CuO_4 was obtained by simply stopping the ozone delivery during cooling after the growth, typically at about 200 °C, and by letting the sample cool down in vacuum to room temperature. Notably, upon

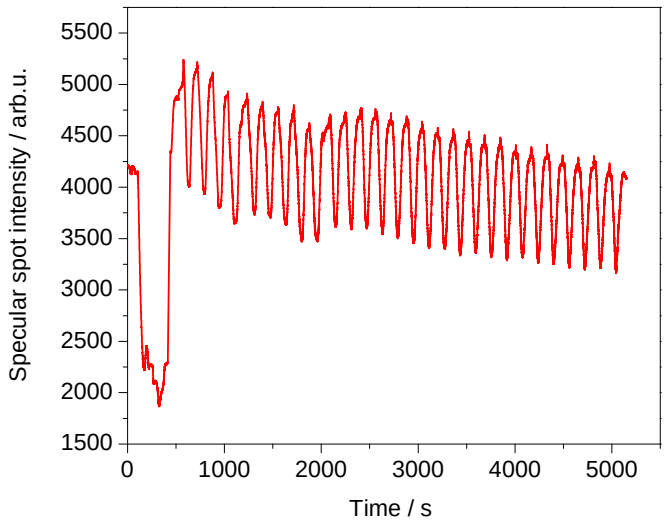

Figure 4.4. Time evolution of the RHEED specular spot during the optimal growth of La_2CuO_4.

ozone annealing, the same samples could be easily turned back into optimally doped superconductor.

In Figure 4.7, the electrical properties of insulating La_2CuO_4 and superconducting $La_2CuO_{4+\delta}$ grown in our system are reported.

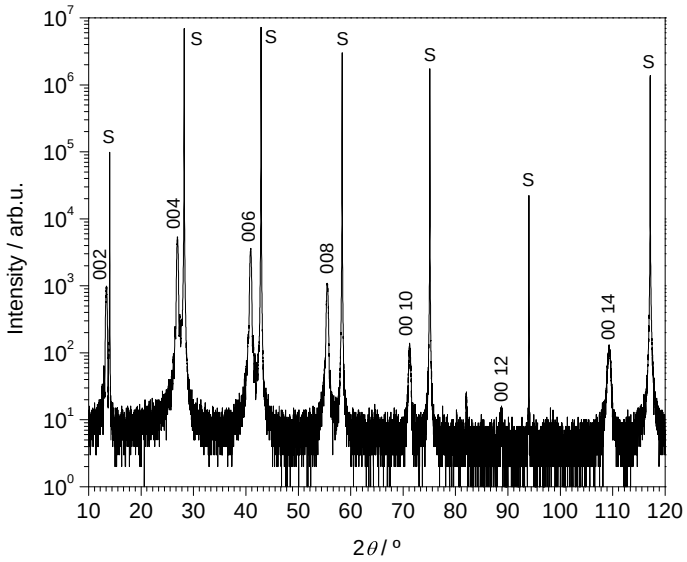

Figure 4.5. XRD fullscan for 40 u.c. La_2CuO_4 on $LaSrAlO_4$ (001) (S).

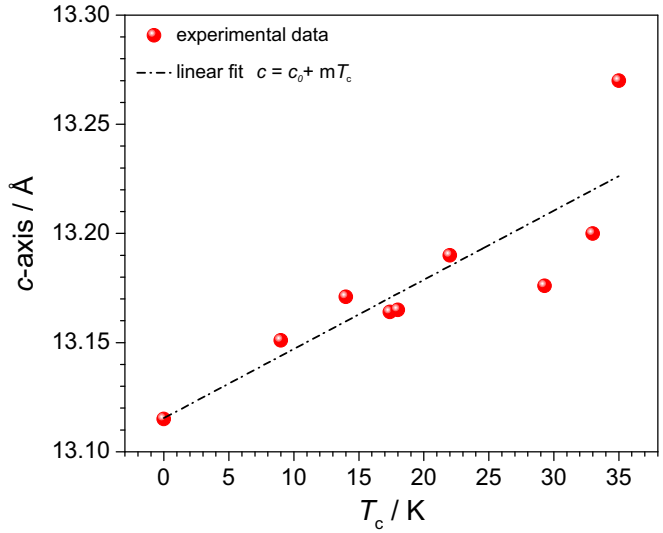

Figure 4.6. Out-of-plane lattice parameter c versus T_c for various La_2CuO_4 films which were grown in our MBE system. Red circles indicate the experimental data point, the dotted black line is the linear fit ($c_0 = 13.115 \pm 0.015$; m$= 0.032 \pm 0.007$; adjusted R-square 0.7).

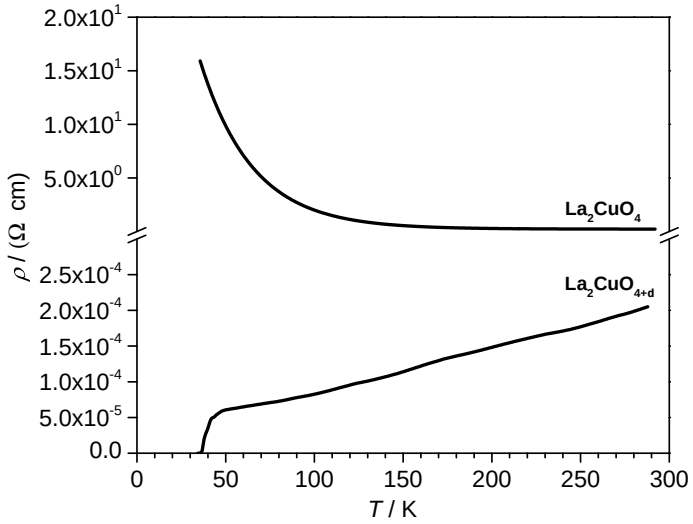

Figure 4.7. Resistivity versus temperature for insulating La_2CuO_4 and superconducting $La_2CuO_{4+\delta}$ grown in our system. Taken from Ref. 125.

4.1.2 Growth of lanthanum strontium nickelate

The synthesis of thin films of $La_{2-x}Sr_xNiO_4$ with various doping content has been reported several times, as the material has been extensively studied especially in relation to: (i) potential application in electrochemical devices due to its mixed oxygen-hole conduction mechanism (ii) structural similarities with high-temperature superconducting materials (iii) peculiar electrical behavior due to insulator-metal transition at $x \approx 0.9$ (see also Section 2.1.4). According to literature, syntheses have mainly been performed by chemical vapour deposition,[153,154] reactive sputtering[155] or pulsed laser deposition,[156–158] but the use of the MBE method is limited to few cases (to the best of our knowledge, dealing with the study of superlattices of La_2NiO_4 and La_2CuO_4).[159]

For the process optimization, we used $SrTiO_3$ (100), $LaSrAlO_4$ (001) and LSAT ($La_{0.18}Sr_{0.82}Al_{0.59}Ta_{0.41}O_3$) (100) substrates. No remarkable difference was found with respect to the final properties of the films.

Synthesis of La_2NiO_4

As to undoped lanthanum nickelate (La_2NiO_4), the main problem to overcome in this study was the possibility that undesired Ruddlesen-Popper (R-P) phases ($La_{n+1}Ni_nO_{3n+1}$ with $n > 1$, see Section 2.1.1) could form in the case of non-optimal growth conditions. Indeed, it was found that the synthesis process was strongly dependent on operating temperature and pressure. This can be explained by the fact that R-P phases with higher n are characterized by a higher Ni oxidation number (in particular, for La_2NiO_4 ($n = 1$) Ni has formal valence +2, for $LaNiO_3$ ($n = \infty$) it is +3, whereas phases with $2 < n < 3$ have a mixed Ni valence). Therefore, less oxidizing conditions (low pressure, high temperature) are expected to favor the formation of phases with lower n. This was experimentally verified, as one can see by comparing the results of XRD scans of two thin films of 40 u.c. La_2NiO_4 (≈ 500 Å), which were grown on $SrTiO_3$ (100) at comparable temperature but by varying the ozone growing pressure in the chamber by one order of magnitude from $P = 2 \times 10^{-6}$ Torr to $P = 2 \times 10^{-5}$ Torr (black line an red line in Figure 4.8, respectively): in both cases, the resulting structures are *c*-axis oriented, but higher crystallinity results from the the one grown at lower pressure, as indicated by the sharper and more intense diffraction peaks. This finding can be explained in light of the presence, at high deposition pressures, of secondary R-P undesired crystallites which are embedded in the structure, determining broader and weaker XRD peaks. Notably, due to the similar crystal structure and to the comparable in-plane lattice parameter of the different R-P phases, the in-situ RHEED analysis (Figure 4.9) does not provide useful informations on the presence of such precipitates. Moreover, the growth of La_2NiO_4 (and more in general of $La_{2-x}Sr_xNiO_4$) is made even more complicated by the fact that it is not characterized by the appearance of superstructure streaks in the RHEED diffraction pattern, which instead in other systems represent a very precious tool for the growth optimization (see for example the case of La_2CuO_4 in Section 4.1.1).

Based on ex-situ XRD analysis, the optimal growth conditions for La_2NiO_4 were found to be 600 °C $< T <$ 660 °C and $P = 1 - 2 \times 10^{-6}$ Torr.

In Figure 4.10 an AFM micrograph for La_2NiO_4 grown on $LaSrAlO_4$ (001)

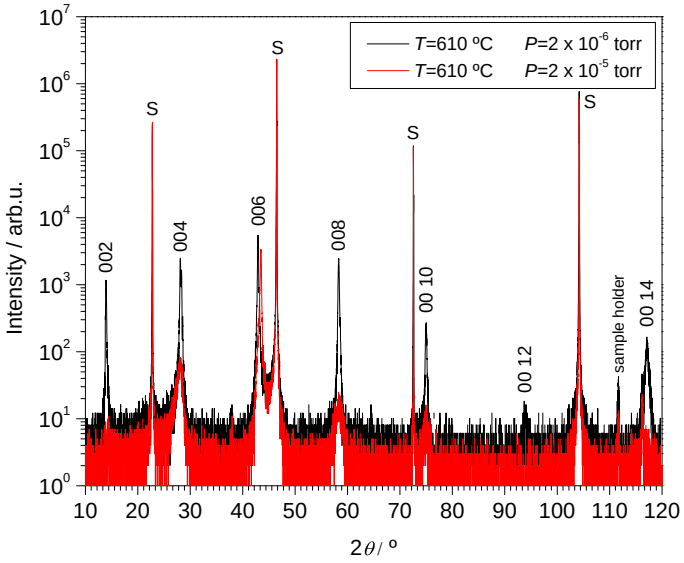

Figure 4.8. XRD scan for two thin films of 40 u.c. La_2NiO_4 on $SrTiO_3$ (100), grown at $T = 610$ °C and pressure $P = 2 \times 10^{-6}$ Torr (black line) and $P = 2 \times 10^{-5}$ Torr (red line).

under optimal conditions is presented. The surface is atomically smooth.

Synthesis of $La_{2-x}Sr_xNiO_4$

In order to synthesize Sr-doped lanthanum nickelate ($La_{2-x}Sr_xNiO_4$) correctly, we found that a higher oxidizing environment was required for increasing Sr doping levels. In this case, wrong growing conditions lead to the formation of secondary phases arising from decomposition. The latter were clearly detectable by RHEED, as can be seen in Figure 4.11.

By appropriately tuning the growth conditions, we were able to synthesize $La_{2-x}Sr_xNiO_4$ with different doping level, spanning the whole solubility range of Sr ($0 \leq x \leq 1.4$). Temperatures in the range $600 \leq T \leq 660$ °C and pressures $\approx 1 \times 10^{-6}$ Torr were used for insulating and low conducting $La_{2-x}Sr_xNiO_4$ ($x < 0.5$), whereas $T \approx 600$ and $P \approx 2 - 3 \times 10^{-5}$ Torr were used for metallic $La_{2-x}Sr_xNiO_4$ ($x \geq 0.9$).

A representative XRD $2\theta/\omega$ scan for a sample of $La_{2-x}Sr_xNiO_4$ ($x = 1$),

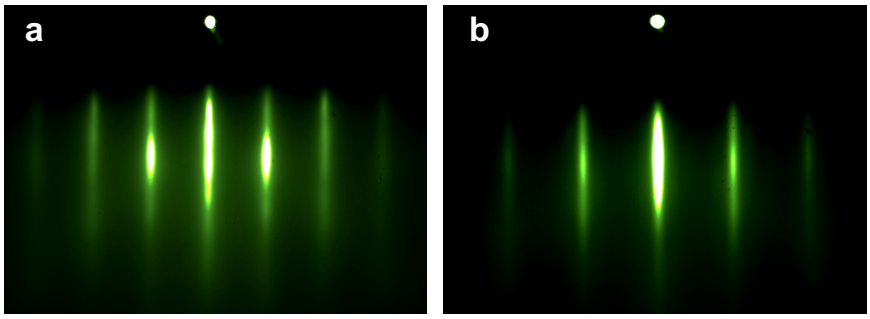

Figure 4.9. RHEED pattern ((100) direction) of La_2NiO_4 on $SrTiO_3$ (100), grown at $T = 610$ °C and pressure $P = 2 \times 10^{-5}$ Torr (a) and $P = 2 \times 10^{-6}$ Torr (b). No remarkable difference can be observed between the two. The respective XRD patterns are shown in Figure 4.8.

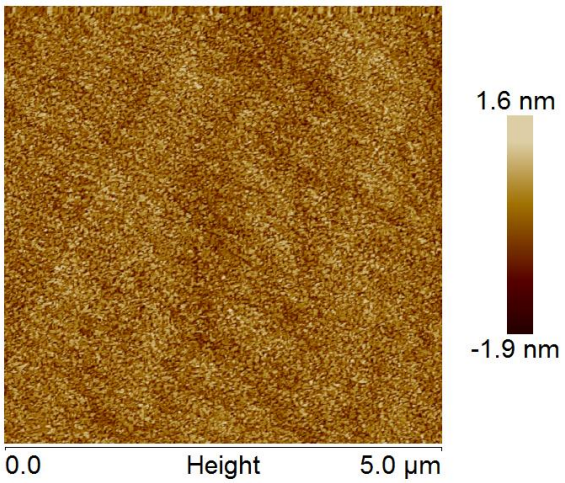

Figure 4.10. AFM micrograph for a film of La_2NiO_4 grown on $LaSrAlO_4$ (001) substrate. $R_{ms} = 0.5$ nm.

epitaxially grown on LSAT (100) in optimal growth conditions ($T \approx 600$ °C, $P \approx 3 \times 10^{-5}$ Torr), is presented in Figure 4.12. In Figure 4.13, the evolution of the out-of-plane-axis lattice parameter c as a function doping level, for a set of grown samples, is presented. It decreases monotonically for increasing x due to the increasing amount of oxygen vacancies which results in the shrinking of the cell in the c-direction (see Section 2.1.4).

An example of AFM micrograph obtained from $La_1Sr_1NiO_4$ is shown in Figure 4.14. Although no secondary phase outgrowths are present, a certain roughness ($R_{ms} \approx 0.8$ nm) is detectable. This is a typical finding for the $La_{2-x}Sr_xNiO_4$ films that we synthesized.

The electrical properties of a representative set of $La_{2-x}Sr_xNiO_4$ thin films are shown in Figure 4.15. As expected, resistance decreases for increasing x. In the range $0.5 < x < 1$, the material undergoes a transition from an insulator to a metal.

The results described above are consistent with the literature data (cf. Section 2.1.4), demonstrating that the optimization of the growth of $La_{2-x}Sr_xNiO_4$ with different doping level was achieved successfully. Nevertheless, it should be mentioned that, as one can see from the comparison of the AFM micrographs (cf. Figure 4.10 and Figure 4.14) and the XRD data (cf. Figure 4.8 and Figure 4.12), a general worsening of the samples quality in terms of surface roughness and crystallinity was observed between La_2NiO_4 and highly doped $La_{2-x}Sr_xNiO_4$. Even though it can not be excluded that the growth conditions could be improved further (in our case, setup limitations prevented us from employing higher working pressures, arguably the key process parameter), it should be kept in mind that highly doped $La_{2-x}Sr_xNiO_4$ is intrinsically highly defective due to the very large amount of oxygen vacancies (see Section 2.1.4). This, together with the high elastic strain induced by the dopant substitution, is likely to affect crystallinity. Moreover, this could also influence the quality of the layer-by-layer growth process, being eventually detrimental for the morphology of the surface.

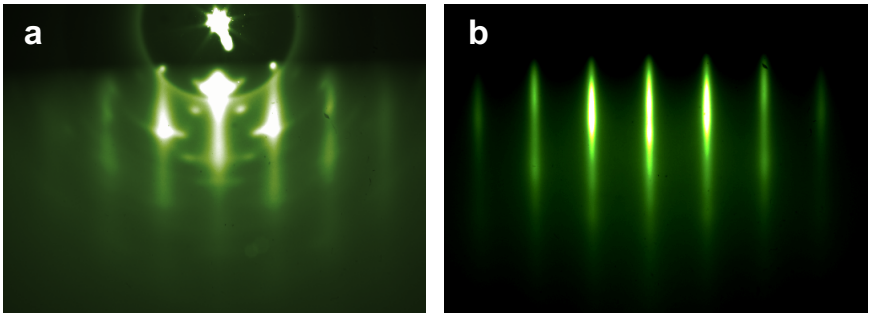

Figure 4.11. RHEED diffraction pattern (along the (100) direction) recorded at the end of the growth of 40 u.c. $La_1Sr_1NiO_4$. Low operating pressure (2.5×10^{-6} Torr) leads to the formation of secondary phases as shown in (a). In (b), pattern observed during a growth at 2.5×10^{-5} Torr (optimal growing conditions).

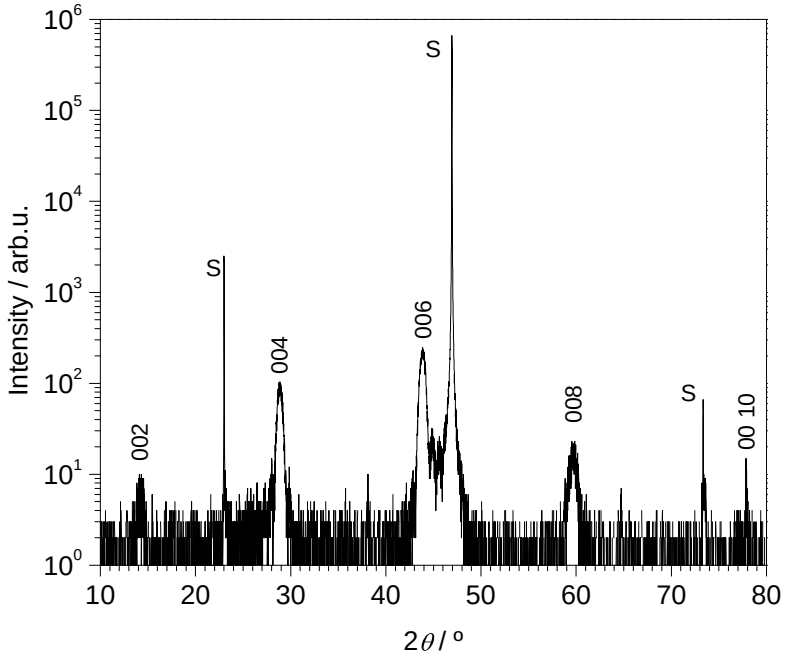

Figure 4.12. XRD $2\theta/\omega$ scan of 13 nm thick $La_1Sr_1NiO_4$ on LSAT(100) (S).

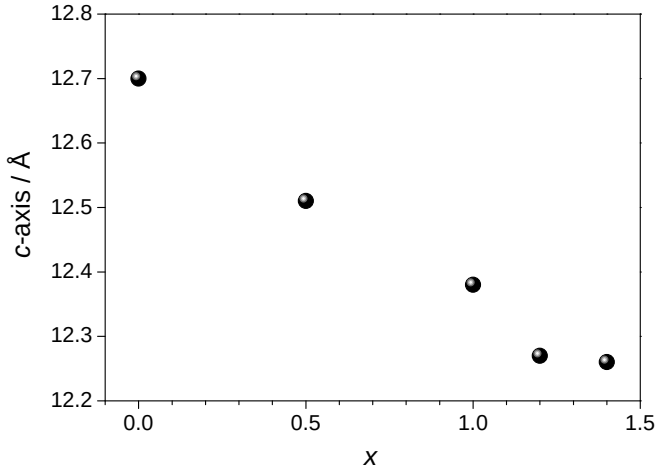

Figure 4.13. *c*-axis value, obtained by applying the Bragg equation for each peak position and subsequent refinement with Nelson-Riley function (see Section 3.2.2), for thin films of $La_{2-x}Sr_xNiO_4$ grown on LSAT (100) substrate.

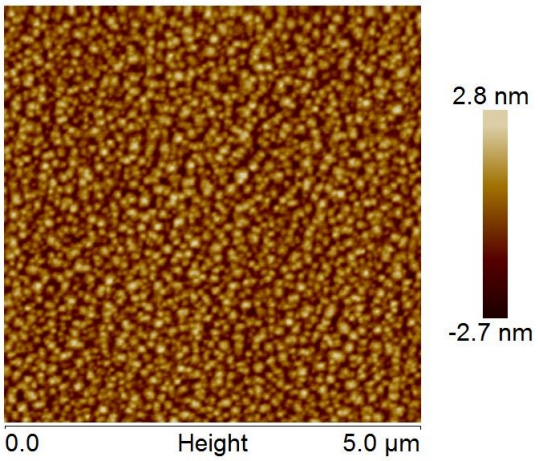

Figure 4.14. AFM characterization for a film of $La_1Sr_1NiO_4$ on $LaSrAlO_4$ (001). R_{ms} roughness is 0.8 nm.

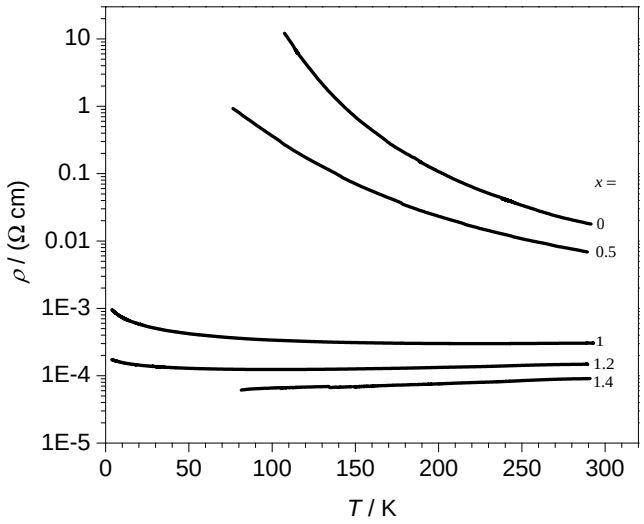

Figure 4.15. Resistivity versus temperature for $La_{2-x}Sr_xNiO_4$ with different doping levels. Reproduced from Ref. 125.

4.2 La_2CuO_4 / $La_{2-x}Sr_xNiO_4$ interface

After the first discoveries of electron accumulation at epitaxial interfaces between insulating materials such as $LaTiO_3$ / $SrTiO_3$ and $LaAlO_3$ / $SrTiO_3$,[17,26] a number of investigations disclosed the occurrence of high electrical conductivity (and, in few cases, superconductivity) in similar systems.[18,27,160–163] Most of the attention however has been addressed to simple perovskite systems (in which superconductivity may appear at $T < 1$ K), with the exception of the investigation of the metallic $La_{2-x}Sr_xCuO_4$ / insulating La_2CuO_4 interface (see Gozar *et. al.* Ref. 30), where high-temperature superconductivity at ≈ 40 K was found as a consequence of local hole redistribution.[32] Here, we explore the possibility of inducing high-temperature superconductivity in a complex oxide (namely La_2CuO_4) as a consequence of space-charge effects occurring at the interface with $La_{2-x}Sr_xNiO_4$.

By comparing the chemical models of La_2CuO_4 (see Section 2.1.2) and of $La_{2-x}Sr_xNiO_4$ (see Section 2.1.4), a chemical potential gradient for holes and oxygen vacancies (as well as for Sr) is expected to be present at the interface between these two compounds due to the abundance of such defect species in $La_{2-x}Sr_xNiO_4$. As a consequence, in order to establish equilibrium conditions (i.e. constancy of

the electrochemical potential, see Section 2.2), especially holes and oxygen vacancies (which are highly mobile, see Ref. 49) are expected to migrate in the direction of La_2CuO_4 determining the formation of a negatively charged region at the $La_{2-x}Sr_xNiO_4$ side of the interface. This transfer direction is expected owing to the large oxygen vacancies and holes concentration irreversibly brought in by Sr-doping. For compensation, a region where positively charged defects (i.e. holes and oxygen vacancies) are accumulated, establishes in La_2CuO_4.

The situation, which is schematically depicted in Figure 4.16, finally leads to the occurrence of high-temperature superconductivity in La_2CuO_4 at the interface due to interfacial hole doping.

It should be noticed that the occurrence of a space-charge situation due to ionic transfer has already been reported in literature in systems such as BaF_2 / CaF_2 or LiF / TiO_2.[13,164] As far as oxygen defects are concerned, it was only demonstrated for grain boundaries.[5]

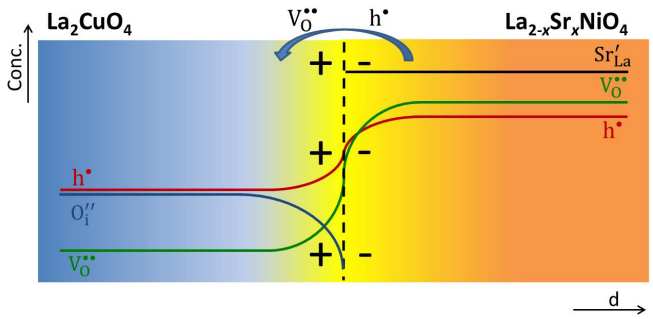

Figure 4.16. Schematic representation of the space-charge scenario at the La_2CuO_4 / $La_{2-x}Sr_xNiO_4$ interface. An electrostatic space-charge potential builds up at the interface as a consequence of the positive charge carriers migration from the $La_{2-x}Sr_xNiO_4$ to the La_2CuO_4, eventually resulting in the accumulation of holes on the La_2CuO_4 side of the interface.

4.2.1 Properties of La_2CuO_4 /$La_{2-x}Sr_xNiO_4$ heterostructures

Heterostructures made of $La_{2-x}Sr_xNiO_4$ and La_2CuO_4 have been realized. The similar crystal structure (and in particular the comparable in-plane lattice parameter of the two phases, see Section 2.1.1), together with the low surface roughness (cf. AFM micrographs in Figure 4.3f and Figure 4.10), make them particularly suitable for the realization of bilayer and superlattice structures. The advantage of superlattice over the bilayer structures consists in the presence of several interfaces in the same sample, with the subsequent magnification of boundary effects. Moreover, this allows for a "statistic" approach i.e. higher reliability on the result coming from a single sample, and for introducing additional degrees of freedom e.g. by varying the spacing between interfaces. On the other hand, by studying a bilayer, one can investigate the properties of a precisely located single interface; in this case though, results can be affected by sample imperfections, therefore a higher amount of samples is desired.

Synthesis and structural properties

The growth of multilayered heterostructures presents, in general, the difficulty that it has to be carried out under conditions which are suitable for both phases, since an approach in which the growth parameters are continuously varied during the growth is difficult to pursue practically and may lead to the decomposition of one of the phases. After the analysis of the growing parameters for La_2CuO_4 and $La_{2-x}Sr_xNiO_4$ single phase thin films, which has been described above (see Section 4.1.1 and Section 4.1.2), we selected $T \approx 600$ °C and $P \approx 2.5 \times 10^{-5}$ Torr as the most suited conditions for the growth of this type of structures. In order to avoid any contribution to the electrical properties of La_2CuO_4 arising from the presence of oxygen interstitials in the bulk, the samples were routinely cooled in vacuum from 200 °C down to room temperature after the growth (see Section 4.1.1). As substrate, $LaSrAlO_4$ (001) was used (see Section 4.1.1).

In Figure 4.17, the RHEED patterns acquired during the deposition of a

La_2CuO_4 /$La_{2-x}Sr_xNiO_4$ multilayer are shown. One can observe the typical features of layer-by-layer growth: specular spot oscillations are maintained throughout the process and no island outgrowths are observed. The transition between La_2CuO_4 and $La_{2-x}Sr_xNiO_4$ is sharp, resulting in negligible oscillation dampening. Moreover, the RHEED patterns from the La_2CuO_4 grown on top of $La_{2-x}Sr_xNiO_4$ (Figure 4.17d and Figure 4.17e) show typical superstructure lines, which is a sign of long range crystalline order (see Section 3.2.1 and Figure 4.3), already from the second monolayer (panel e). These observations indicate the high-quality of the growth process.

In Figure 4.18, the XRD characterization of a lanthanum cuprate / lanthanum strontium nickelate ($La_{0.7}Sr_{1.3}NiO_4$) superlattice is shown. The high crystalline quality and interface sharpness are demonstrated by the pronounced Bragg peaks (up to the 00 14 reflection order) and by the presence of strong satellite peaks, as highlighted in (b), which shows a magnification of the (004) diffraction peak. Finally, a representative AFM micrograph for $La_{2-x}Sr_xNiO_4$ / La_2CuO_4 superlattice is depicted in Figure 4.19. No secondary phase outgrowths are visible.

Electrical properties of superlattices

A set of samples has been realized in order to study the electrical properties of the multilayer $La_{2-x}Sr_xNiO_4$ / La_2CuO_4 structure as a function of the doping level of the lanthanum nickelate x. In particular, superlattices having nominal composition

$$1 \times La_{1.56}Sr_{0.44}CuO_4 + S \times [2.5 \times La_{2-x}Sr_xNiO_4 + N \times La_2CuO_4]$$

have been synthesized. Here S the number of superlattice unit repetitions (please note that the thickness of the constituting phases is expressed in number of unit cells). A thin buffer layer (1 u.c. metallic $La_{1.56}Sr_{0.44}CuO_4$) was routinely deposited on the substrate in order to facilitate the growth process by improving the film / substrate interface.[165] Notably, by limiting the thickness of $La_{2-x}Sr_xNiO_4$ to 2.5 u.c., a lower interface roughness can be expected.

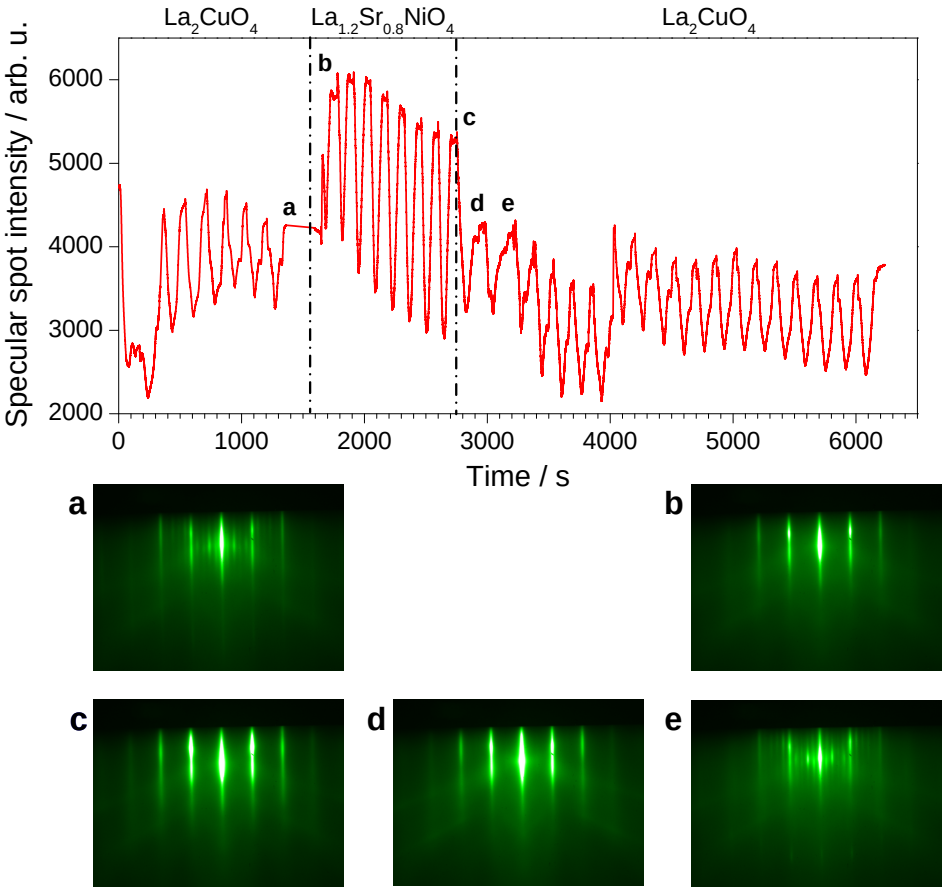

Figure 4.17. Time evolution of the RHEED specular spot intensity recorded during the deposition of a trilayer structure of 4 u.c. La_2CuO_4 / 4 u.c. $La_{1.2}Sr_{0.8}NiO_4$ / 10 u.c. La_2CuO_4 on $LaSrAlO_4$ substrate. Different diffraction patterns can be recognized. In particular, the bottom La_2CuO_4 layer exhibits the typical features of the phase, including the superstructure lines between the main streaks (a). During the growth of $La_{1.2}Sr_{0.8}NiO_4$, no secondary phases outgrowths are detected (panel (b) and (c)). The top La_2CuO_4 layer grows epitaxially (d) and exhibit finite superstructure lines starting from the second monolayer (e). The absence of the superstructure in (d) is indicative of a certain crystallographic disorder at the interface. During the entire growth, pronounced RHEED oscillations are maintained.

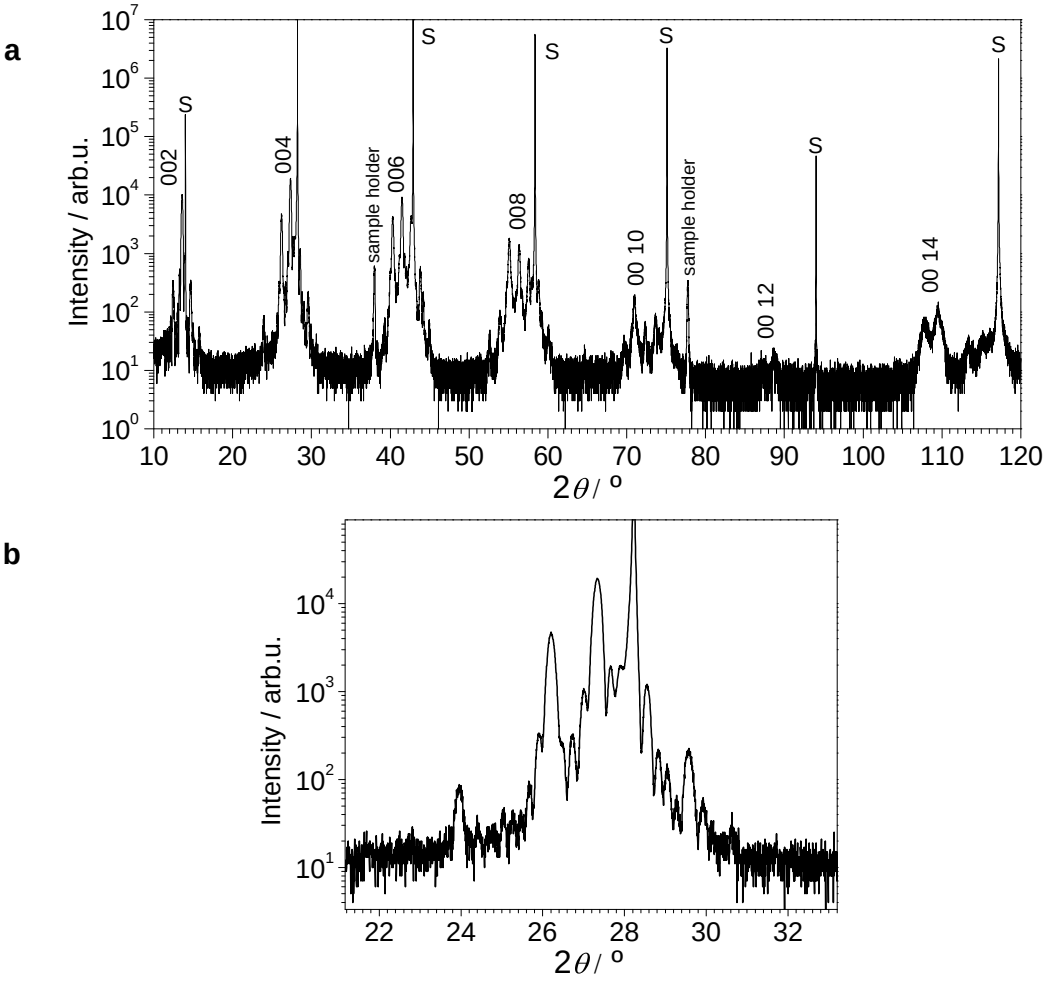

Figure 4.18. a) XRD fullscan pattern of a $La_{2-x}Sr_xNiO_4$ / La_2CuO_4 superlattice ($S = 5$, $N = 3.5$). b) Magnification of the 004 Bragg peak.

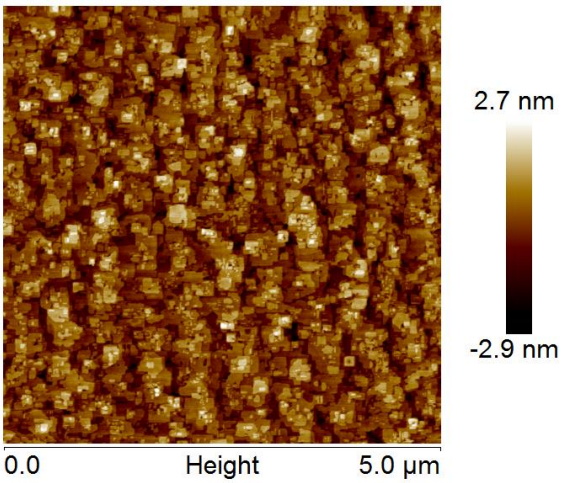

Figure 4.19. AFM micrograph for a $La_{2-x}Sr_xNiO_4$ / La_2CuO_4 superlattice ($S = 8$, $N = 1.5$). Roughness R_{ms} =0.8 nm.

Dependence on *x*. The resistance data for a set of samples having different doping level x of $La_{2-x}Sr_xNiO_4$ are shown in Figure 4.20. Remarkably, for increasing x, the samples do not only exhibit reduced resistance, as one would expect given the increasing metallic character of the $La_{2-x}Sr_xNiO_4$ phase, but they also show high-temperature superconductivity. Given that the vacuum treatment performed on the samples allows one to rule out the presence of oxygen interstitials in bulk La_2CuO_4 (far from the interface), we can conclude that high-temperature superconductivity is induced in La_2CuO_4 as a consequence of an interface effect. Notably, any contribution to superconductivity stemming from $La_{2-x}Sr_xNiO_4$ can easily be excluded by observing that the single phase material does not exhibit superconducting behavior (see Section 2.1.4). In Figure 4.21, the T_c values as a function of the doping level are summarized. Superconductivity is found for $x > 0.5$, reaching the plateau value of $\approx$ 35-40 K for $x > 0.8$.

Dependence on *N*. The dependence of T_c on the La_2CuO_4 thickness N has also been analyzed. The doping level (x=1.3) was kept constant. Notably, by choosing such a high x value, we were able to better highlight the role of cationic intermixing at the interface (see the TEM study in Section 4.2.1). The results, summarized

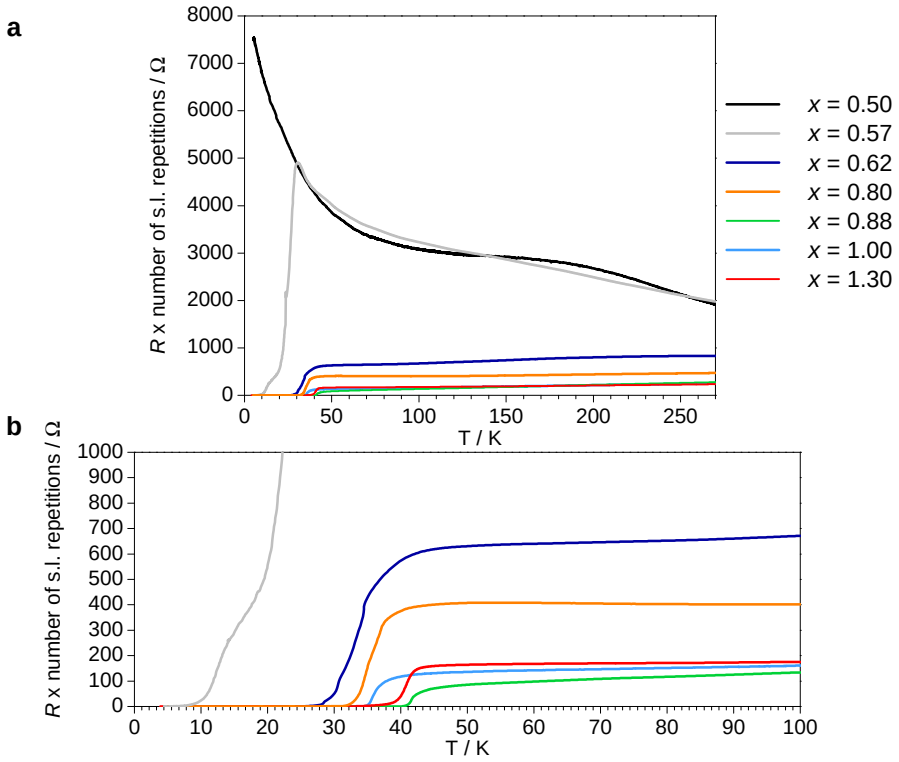

Figure 4.20. a) R versus T for superlattice structures ($N = 2.5$) on $LaSrAlO_4$ substrate. The measured resistance values are normalized by multiplication with the number of superlattice repetitions. b) Magnification of the low resistance region, showing in greater details the superconducting transition.

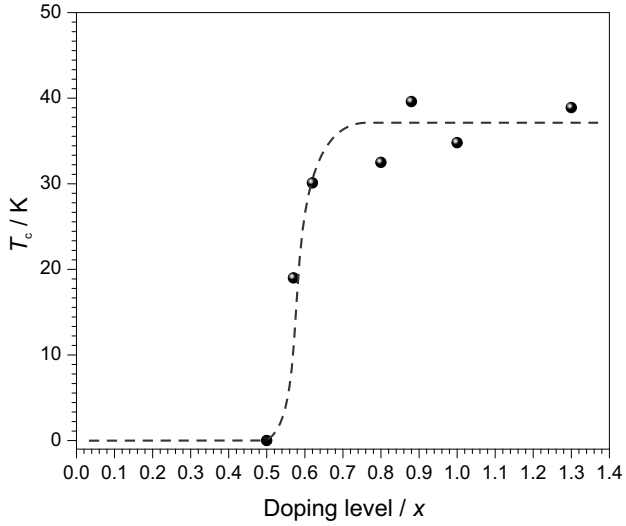

Figure 4.21. T_c values as a function of the lanthanum nickelate doping level x for the superlattices whose resistance curve is shown in Figure 4.20. The dotted line is a guide to the eye.

in Figure 4.22, show that an optimal thickness exists (comprised between 2.5 u.c. and 5.5 u.c.) giving rise to the highest T_c ($T_c \approx 40$ K). A small La_2CuO_4 thickness is detrimental for superconductivity, probably as a consequence of a certain crystallographic disorder which is present in the proximity of the interface as also indicated by the RHEED pattern during the growth (see Figure 4.17d). For a large La_2CuO_4 thickness, the T_c values predictably approach the bilayer T_c limit of ≈ 20 K (see following paragraph and Section 4.2.3). In Figure 4.23, all the resistance versus temperature curves are reported.

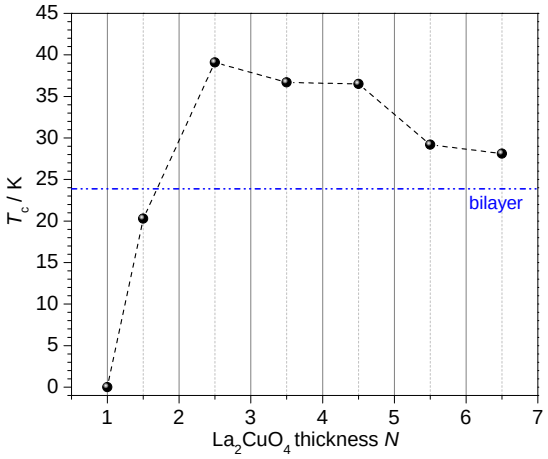

Figure 4.22. T_c values as a function of La_2CuO_4 thickness N in superlattice structures. The dotted blue line is the maximum T_c value measured for a $Sr_{1.3}La_{0.7}NiO_4$/ La_2CuO_4 bilayer.

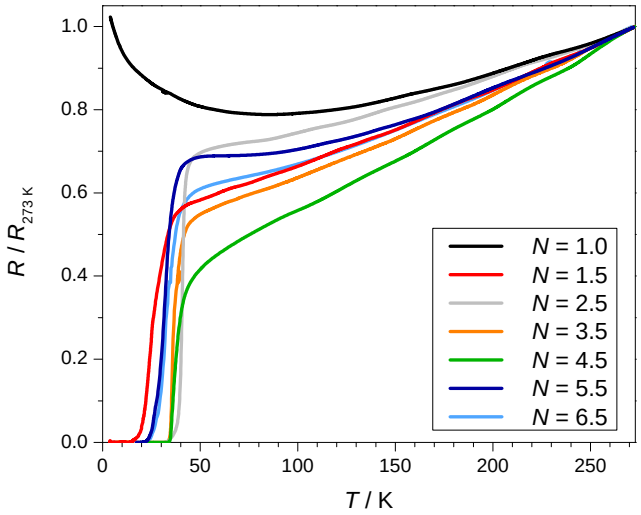

Figure 4.23. Resistance versus temperature curves for $Sr_{1.3}La_{0.7}NiO_4$ / La_2CuO_4 superlattices (see also Figure 4.22). In order to allow for a better comparison, resistance values have been normalized to the resistance value at 273 K.

Electrical properties of bilayers

The properties of bilayers consisting of

$$4 \text{ u.c. } La_2CuO_4 + 4 \text{ u.c. } La_{2-x}Sr_xNiO_4$$

have been studied. In particular in order to verify whether the sequence of the layers matters for yielding superconductivity (i.e. La_2CuO_4 deposited as a bottom or top layer), we systematically compared the electrical behavior of structures characterized by reverse sequence of the layers (maintaining the same nominal composition of the phases). In Figure 4.24, the electrical properties of such films are shown, for various doping levels of lanthanum nickelate. In Table 4.1, the T_c values are summarized. Focusing on the case in which $x = 1.3$ (composition which has also been analyzed by TEM, see Section 4.2.1), one can clearly see that T_c is independent on the sequence in which the layers are deposited ($T_c \approx 23$ K). Which is, La_2CuO_4 hole doping level at the interface is, in both cases, equal (or close) to the optimal. By decreasing x, one can see that, in the case of the La_2CuO_4 / $La_{2-x}Sr_xNiO_4$ bilayer, the critical temperature is only marginally affected as long as $x \geq 0.8$, with T_c varying from 23.9 K to 18.9 K by decreasing x. The variation of the T_c-onset ($T_{c,0.9}$) is more pronounced, decreasing from 41 K for $x = 1.3$ to 34.8 K for $x = 0.8$. This is indicative of a higher degree of doping inhomogeneity or of an increased amount of structural disorder in La_2CuO_4 when x in $La_{2-x}Sr_xNiO_4$ is higher, as also described in Section 3.5.2. For $x = 0.7$, only $T_{c,0.9}$ could be measured ($T_c < 4$ K).

In the opposite situation (La_2CuO_4 as top layer), the occurrence of high-temperature superconductivity seems to be promoted also for low doping levels ($T_c = 32.4$ K for $x = 0.7$), but it should be mentioned that, in this case, the critical x could not be defined precisely (for example, superconducting transition was measured for some samples with x as low as 0.4). This could be ascribed to the difficulties that we encountered in controlling the growth of $La_{2-x}Sr_xNiO_4$ especially in relation to the cationic stoichiometry (see Section 4.1.2). This can be considered as an accidental factor working in same cases (e.g. in the case of Ni-poor stoichiometry eventually resulting in an accumulation of the excess La

and Sr on the surface of the growing film) in favor of intermixing of the phases, this way promoting the occurrence of high-temperature superconductivity (see Section 4.2.2). Remarkably, increasing the doping level resulted, in the case of La_2CuO_4 as top layer, in worse electrical properties, in terms of both metallicity (i.e. slope of the resistance curve) and T_c. This might be due to the increased roughness of $La_{2-x}Sr_xNiO_4$ for higher doping level (as described in Section 4.1.2) determining an increased disorder the $La_{2-x}Sr_xNiO_4$ / La_2CuO_4 interface.

Notably, the study of the superlattices (see Figure 4.21) revealed that $T_c > 30$ K occurs for $x \approx 0.6$ or higher, providing a reliable indication of the x value that can be taken as threshold for the occurrence of high-temperature superconductivity in La_2CuO_4.

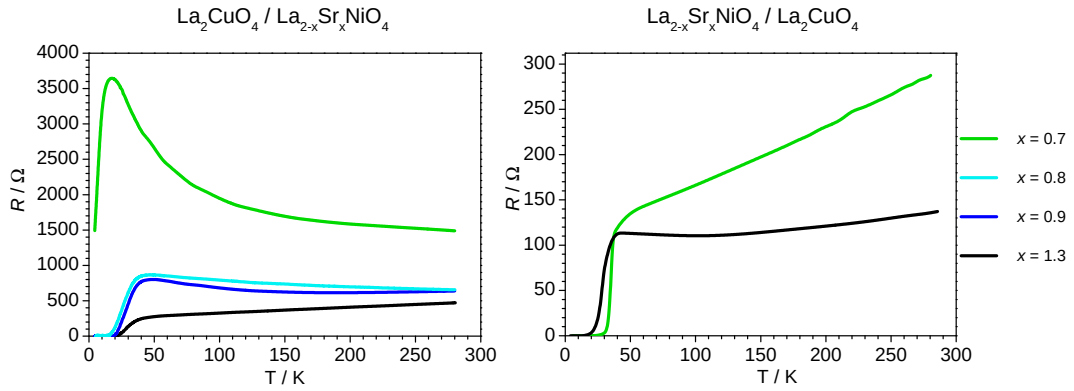

Figure 4.24. Electrical properties of bilayers made of 4 u.c. La_2CuO_4 and 4 u.c. $La_{2-x}Sr_xNiO_4$ as a function of temperature for different doping levels. In (a), results from structures having La_2CuO_4 as a bottom layer. Results from the opposite structure (La_2CuO_4 grown on $La_{2-x}Sr_xNiO_4$) are shown in (b).

La_2CuO_4 / $La_{2-x}Sr_xNiO_4$			$La_{2-x}Sr_xNiO_4$ / La_2CuO_4	
doping level	$T_{c,\,0.9}$ (K)	T_c (K)	$T_{c,\,0.9}$ (K)	T_c (K)
0.7	10.7	< 4 K	45.3	32.4
0.8	34.8	18.9	not grown	
0.9	36.8	22.4	not grown	
1.3	41.0	23.9	34.9	23.2

Table 4.1. T_c summary for bilayers of $La_{2-x}Sr_xNiO_4$ and La_2CuO_4 (resistance curves are reported in Figure 4.24.

TEM characterization

In order to investigate the structural aspects of the $La_{2-x}Sr_xNiO_4$ / La_2CuO_4 interface, a selection of samples was studied by TEM.[1] In Figure 4.25, the results of the interface elemental analysis, as measured by EELS across a $Sr_{1.3}La_{0.7}NiO_4$ region (nominal thickness 2.5 u.c.) and the neighboring La_2CuO_4 layers in a superlattice structure, are depicted. The EELS profile (Figure 4.25b) is obtained by integrating the signal over the region shown in Figure 4.25a, in which a spatial compositional map is presented. The single atomic column resolution allows for analyzing the local composition: in particular, each maximum in the Cu intensity curve shows the position of the CuO_2 planes; similarly, the maxima of the blue curve are assigned to the NiO_2 planes. The La intensity oscillations (in green) are, as expected, in opposition of phase (i.e. the La intensity maxima correspond to the Cu (or Ni) minima and vice versa, reflecting the nominal alternation of AO layers and BO_2 planes as described in Section 2.1.1). One can observe a certain Cu/Ni intermixing, which is limited to one atomic plane at each side of the $Sr_{1.3}La_{0.7}NiO_4$. This can be explained by simply considering the intrinsic roughness, which in the best of the cases is as low as the substrate roughness, about 0.5 nm, namely half a u.c. (see also the final roughness of the heterostructures, Figure 4.19). Most

[1] The observations and analyses were performed by Dr. Yi Wang at the StEM group (Prof. Van Aken) at the Max Planck Institute for Solid State Research (Stuttgart).

importantly, the data show that a certain Sr amount spreads (for about an additional half u.c.) from the nickelate into the cuprate phase particularly at the top interface (the one in the growth direction), whereas the bottom interface seems to be sharper (the extension of the Cu/Ni and the Sr/La intermixing area is here comparable).

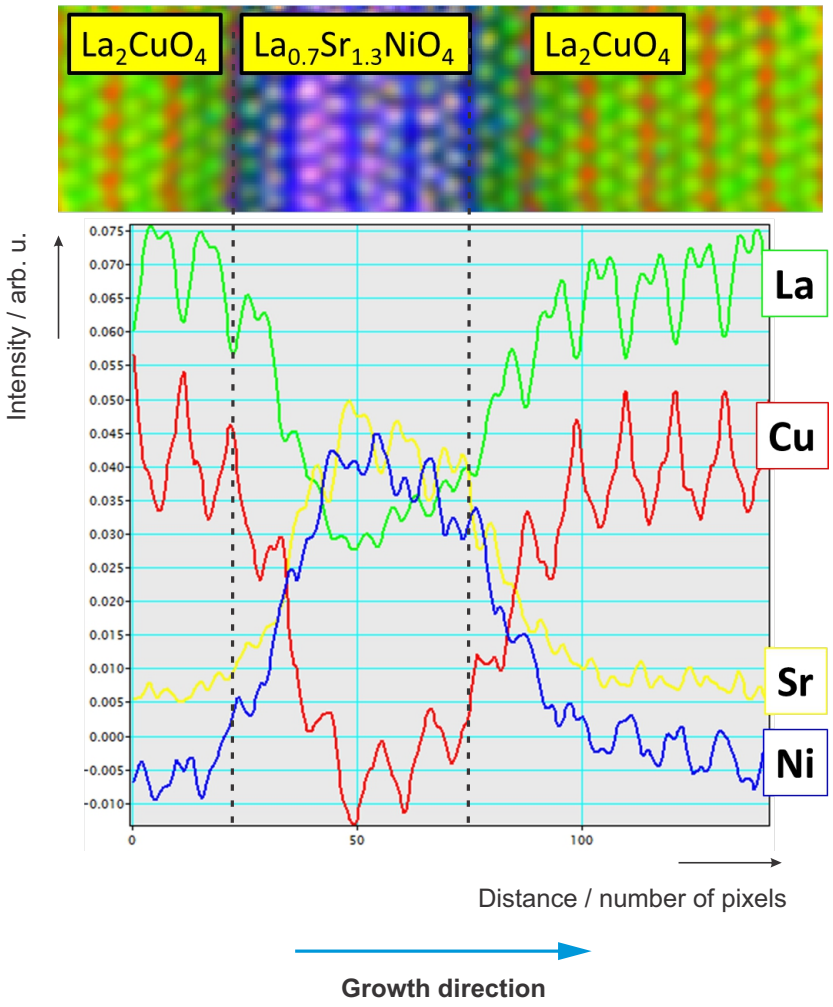

Figure 4.25. a) Spatial map of the different elements over a $La_{0.7}Sr_{1.3}NiO_4$ region of 2.5 u.c., i.e. 5 NiO_2 planes, and the neighboring La_2CuO_4 layers. b) TEM-EELS profile showing the intensity profiles for the different elements. The black dotted lines mark the nominal position of the interfaces.

4.2.2 Discussion

In the light of the experimental findings described above, several explanations may be considered for rationalizing the observed high-temperature superconductivity at the interface between $La_{2-x}Sr_xNiO_4$ and La_2CuO_4.

Cationic intermixing at the interface

According to the TEM data, a certain cationic redistribution occurs at the interfaces (see Figure 4.25). Even though it is very limited, yet, a role in the occurrence of high-temperature superconductivity could be attributed to unintentional Sr doping of La_2CuO_4 , as depicted in Figure 4.26. This is especially true for what concerns the situation in which $La_{2-x}Sr_xNiO_4$ is underneath La_2CuO_4, where we can identify about 1 u.c. of Sr-doped La_2CuO_4. On the other hand, the opposite situation (i.e. La_2CuO_4 underneath $La_{2-x}Sr_xNiO_4$) results in a sharper interface, the width of the region affected by the Sr diffusion being comparable with the Cu/Ni intermixing width. Cationic intermixing at epitaxial interfaces has been reported several times in literature and represents one of the key aspects in this type of systems since it may deeply affect, or even be mainly responsible for the interface functionalities. Therefore, great effort is put in discerning its role for example in the well-studied case of the $LaAlO_3$ / $SrTiO_3$ interface (in which La from $LaAlO_3$ could act as a donor dopant for $SrTiO_3$) and also in related structures. As a matter of fact, a certain intermixing is often observed, but its width and its role in the system properties are currently under debate.[20,25,166–170] In this sense, our case is particularly interesting since it exhibits an asymmetric behavior for the two interfaces, whose intermixing width depends on sequence of the layers. Such a finding has been highlighted only in few cases (e.g. $LaVO_3$ / $SrTiO_3$ superlattices and $LaMnO_3$ / $SrMnO_3$ superlattices).[171,172]

Whether or not Sr intermixing alone is sufficient for explaining high-temperature superconductivity in the present case, is controversial. In particular, the following further aspects need to be taken into account:

- **Comparable electrical properties for the two interfaces.** The study

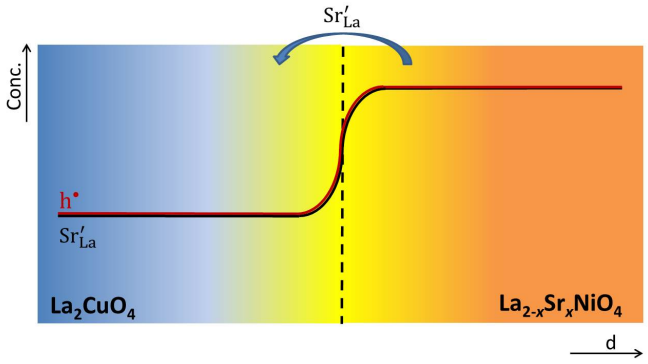

Figure 4.26. Interfacial doping of La_2CuO_4 by Sr/La redistribution (schematic).

of $La_{2-x}Sr_xNiO_4$ / La_2CuO_4 bilayers showed that the electrical properties of the interfaces are only partially affected by the sequence of the layers. On the other hand, TEM analysis showed that Sr preferably migrates in the growth direction, suggesting that the $La_{2-x}Sr_xNiO_4$ / La_2CuO_4 interface undergoes a more extended cationic redistribution than in the opposite case (La_2CuO_4 / $La_{2-x}Sr_xNiO_4$ bilayer). Therefore, a discrepancy between structural and electrical properties is present.

- **Doping level.** High-temperature superconductivity ($T_c > 30$ K) was found for doping levels as low as $x = 0.62$ in the case of superlattices (see Figure 4.21). This is more than twice as low as the composition analyzed by TEM. In such a case it is reasonable to expect a less pronounced Sr-diffusion from the nickelate into the cuprate. Despite this, high-temperature superconductivity is only marginally affected.

- **Cu/Ni intermixing**. The presence of Ni in the CuO_2 planes is expected to determine a decrease of T_c.[173–175] Therefore, one could infer that the first La_2CuO_4 layers next to the $La_{2-x}Sr_xNiO_4$ phase, where most of the Sr but also some Ni is present, have depressed superconducting properties. This suggests that high-temperature superconductivity may occur in La_2CuO_4 layers which are not the closest to the interface, but rather in those where the Sr concentration is lower (or negligible).

For this reasons, the following alternative scenarios need to be considered.

Electron transfer. From the experimental data, it is evident that the key parameter for the appearance of superconductivity is the doping level of $La_{2-x}Sr_xNiO_4$. By Sr-doping, one introduces holes in the $La_{2-x}Sr_xNiO_4$ system, which, in the single phase form, even undergoes a insulator-to-metal transition at a critical doping level of $x \approx 0.9$ as reported by literature[156] and as confirmed in this study (see Figure 4.15). Remarkably, this is very similar to the doping level at which the superconducting state is fully developed in our structures. This allows one to consider electron transfer as a possible explanation for high-temperature superconductivity: in order to maintain constant hole electrochemical potential (see Section 2.2), delocalized holes are transferred from the metallic $La_{2-x}Sr_xNiO_4$ to the La_2CuO_4 phase and high-temperature superconductivity appears due to hole doping in La_2CuO_4. At the $La_{2-x}Sr_xNiO_4$ side of the interface, such a situation determines the presence of a negatively charged region due to an excess of charged ionic defects (Sr'_{La}), which is compensated by excess holes at the La_2CuO_4 side as depicted in Figure 4.27. High-temperature superconductivity is eventually induced by pure p doping of La_2CuO_4. This scenario, which is inspired by the concept of p-n junction typical of semiconductors, has found experimental proof also in the field of oxides.[26,28] In particular, the case of metallic $La_{2-x}Sr_xCuO_4$ / insulating La_2CuO_4 bilayers,[30,31] in which high-temperature superconductivity is induced in La_2CuO_4 as a consequence of hole transfer, is in line with the considerations made for the present case.

Ionic space charge. The scenario described above, taking into account hole transfer, neglects the role of other ionic charged species. Such assumption may not be valid in our case, since $La_{2-x}Sr_xNiO_4$ is rich of oxygen vacancies $V_O^{\bullet\bullet}$. As described above (see Figure 4.16), the condition of electrochemical potential constancy for $V_O^{\bullet\bullet}$ results in a rearrangement of such ionic specie across the interface: in particular, if oxygen vacancies are depleted in $La_{2-x}Sr_xNiO_4$ at the interface, this results in a negative space charge potential. Its compensation requires positive charges, i.e. $V_O^{\bullet\bullet}$ and in particular $h^{\bullet}$, to be enhanced on the La_2CuO_4 side,

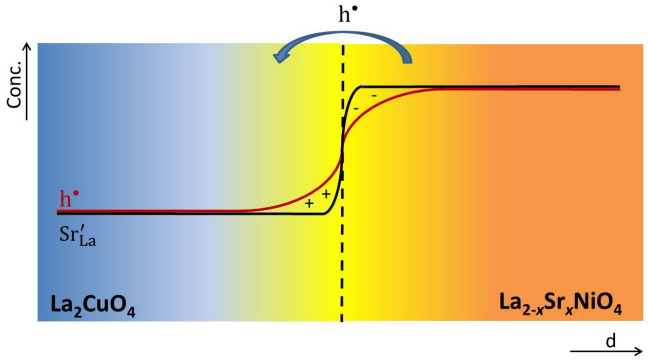

Figure 4.27. Schematic description of hole transfer from $La_{2-x}Sr_xNiO_4$ to La_2CuO_4, with formation of two charged regions at the interface as a consequence of disproportion between Sr'_{La} and $h^{\bullet}$ concentration. The concentration profiles are depicted in blue (red) for Sr'_{La} ($h^{\bullet}$).

eventually giving rise to high-temperature superconductivity due to hole accumulation. Notably, $V_O^{\bullet\bullet}$ is a minority defect in La_2CuO_4.

Realistic scenario. At least for what concerns the La_2CuO_4 / $La_{2-x}Sr_xNiO_4$ interface, in which Sr redistribution is limited, it seems reasonable to consider the space-charge scenario as responsible for high-temperature superconductivity. Compared to the case in which only holes or oxygen vacancies redistribute from the nickelate into the cuprate, the diffusion of Sr would result in a lower space charge potential as a consequence of negatively charge defects (Sr'_{La}) migration. In the opposite case instead ($La_{2-x}Sr_xNiO_4$ / La_2CuO_4 interface), one should take into account the non-negligible cationic intermixing, which can be accounted for high-temperature superconductivity. The realistic picture, a "mixed" situation in which space-charge effects occurr at the La_2CuO_4 / $La_{2-x}Sr_xNiO_4$ interface, whereas the $La_{2-x}Sr_xNiO_4$ / La_2CuO_4 interface is dominated by cationic intermixing, is illustrated in Figure 4.28.

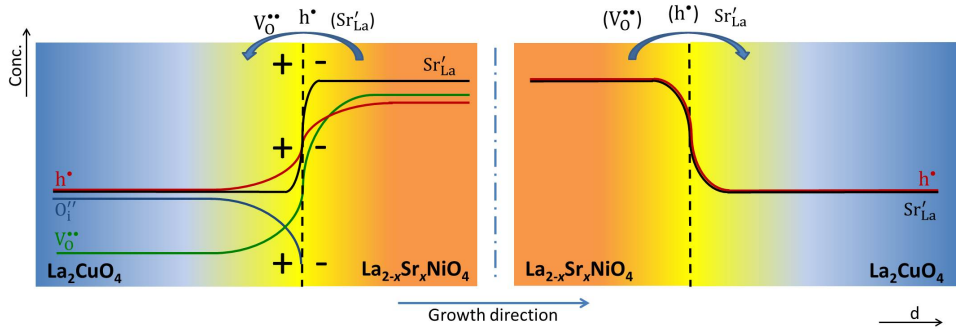

Figure 4.28. Schematic picture of the realistic situations occurring at the cuprate/nickelate interfaces considered here: the bottom interface (i.e. La_2CuO_4 / $La_{2-x}Sr_xNiO_4$ layers sequence) is dominated by space-charge effects, whereas at the top interface ($La_{2-x}Sr_xNiO_4$ / La_2CuO_4 layers sequence) Sr redistribution is predominant.

4.2.3 Further considerations

In the following, further interesting aspects of the nickelate / cuprate interface, which have been disclosed during our studies, are pointed out.

$La_{2-x}Ba_xNiO_4/La_2CuO_4$ heterostructures

The use of Ba as a dopant, instead of Sr, for lanthanum nickelate, has some potential advantages for the study of interface effects:

- **Different cationic radius.** Due to the larger ionic radius and atomic mass (see Table 2.2), one could expect a different diffusivity for Ba compared to Sr. Whether this would be lower or higher is not straightforward, as one might expect at first diffusion to be be facilitated for lighter elements i.e. for Sr over Ba, but on the other hand, studies on ionic crystals have frequently found increasing diffusivity for larger atoms, probably as a consequence of the greater polarizability.[176,177] At any rate, a comparison of the interface intermixing in the two cases and the respective electrical properties would provide useful informations. Moreover, the ionic radius affects the in-plane lattice parameter of lanthanum nickelate, which is larger for the Ba-doped phase than for the Sr-doped one.[98] Due to epitaxial strain, we expect, as

a consequence, higher in-plane tensile strain in La_2CuO_4 if coupled with Ba-doped nickelate. This is a well-known factor working in favor of high-temperature superconductivity in La_2CuO_4.[82,149]

- **Different oxygen vacancies concentration.** Studies on lanthanum nickelate pellets have demonstrated that a higher level of oxygen deficiency is found for Ba-doped samples than for Sr-doped ones.[98] Therefore by comparing the effect of different dopants, one might also gain insight into the role of $V_O^{\bullet\bullet}$ at the interface (see"ionic space charge" case in Section 4.2.2).

In Figure 4.29, we compare the electrical properties of two bilayers having similar structure La_2CuO_4 / $La_{1.3}M_{0.7}NiO_4$, in which M=Sr (black curve), Ba (red curve). Notably, according to these preliminary data, improved electrical properties result from using Ba as a dopant for the nickelate.

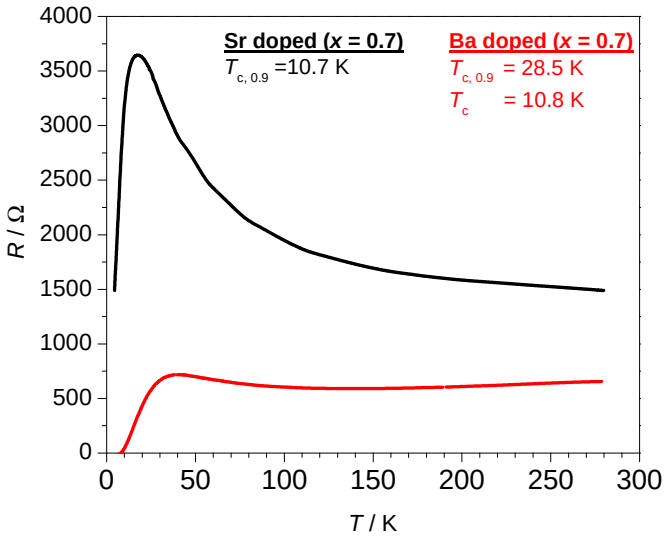

Figure 4.29. Resistance versus temperature for 4 u.c. La_2CuO_4 / 4 u.c. $La_{1.3}M_{0.7}NiO_4$ (M=Sr, Ba) on $LaSrAlO_4$ substrate.

Lattice parameter

The average out-of-plane axis parameter of $La_{0.7}Sr_{1.3}NiO_4$ / La_2CuO_4 superlattice structures ($\bar{d}_{exp}$) has been obtained applying Equation (3.2) to the XRD main diffraction peaks, and has been compared with the theoretical value $\bar{d}_{th}$ obtained according to Equation (3.4):

$$\bar{d}_{th} = \frac{\Lambda}{N+M} = \frac{c_{La_2CuO_4} \times N + c_{La_{0.7}Sr_{1.3}NiO_4} \times M}{N+M} \tag{4.1}$$

in which N and M are the numbers of La_2CuO_4 and $La_{0.7}Sr_{1.3}NiO_4$ unit cells in the superlattice unit, respectively. Please note that in the investigate superlattices M is constant, namely $M = 2.5$.

For the calculation of $\bar{d}_{th}$, the c-axis parameter for La_2CuO_4 was set as $c_{La_2CuO_4} = 13.25$ Å, which is the typical value for optimally doped lanthanum cuprate (see Figure 4.6), whereas $c_{La_{0.7}Sr_{1.3}NiO_4} = 12.45$ Å, in agreement with literature.[156] Please note that the resulting $\bar{d}_{th}$ is likely to be overestimated, since only few layers of La_2CuO_4 in the structure are expected to be superconducting (the remaining layers, insulating, are characterized by lower lattice parameter). Note also that the value taken for $c_{La_{0.7}Sr_{1.3}NiO_4}$ is higher than the one that was obtained for the single phase films investigated here (probably as a consequence of a higher concentration of oxygen vacancies) (cf. Figure 4.13).

The outcome is shown in Figure 4.30. Interestingly, a discrepancy between $\bar{d}_{exp}$ and $\bar{d}_{th}$ is present, with $\bar{d}_{exp} > \bar{d}_{th}$. This could be due to the smeared Sr distribution that we observed, eventually affecting the c-axis parameter as described in the previous sections (see for example Figure 4.13 and Section 2.1.2), but it could also indicate that a certain adjustment of the out-of-plane lattice parameter between the two phases occurs as a consequence of electrostatic interactions in the ionic crystal structure.[69] While it is well-known that the different phases adapt their in-plane lattice parameter to each other in epitaxial structures (epitaxial strain), less is known about the out-of-plane adjustments ("Madelung strain").[69] Therefore, it would be interesting to investigate (e.g. by means of TEM imaging) the local distance between each atomic layer in order to highlight a possible effect of "out-of-plane strain" induced by the epitaxial superlattice structure.

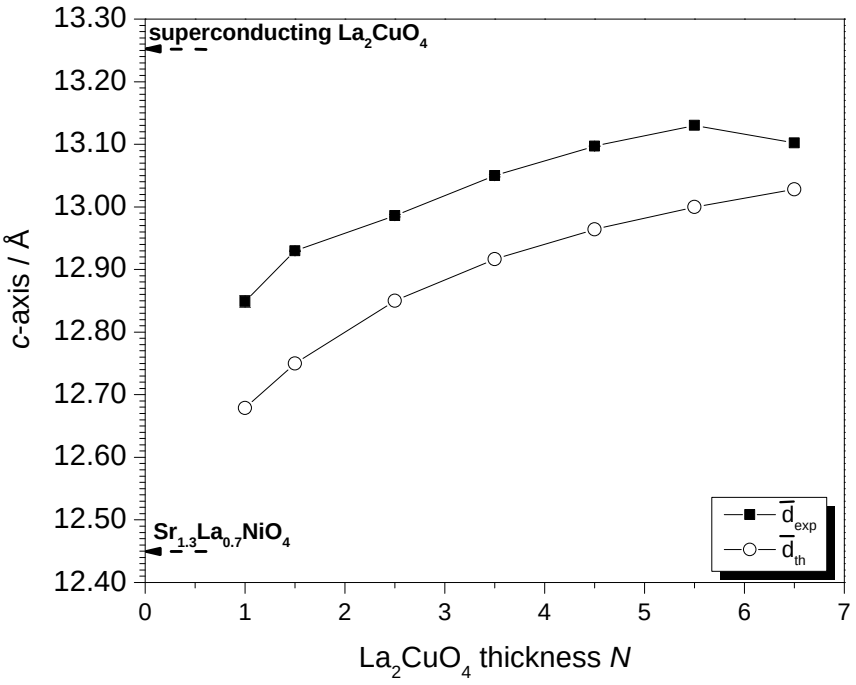

Figure 4.30. Average lattice spacing in $La_{0.7}Sr_{1.3}NiO_4$ / La_2CuO_4 superlattices as obtained by XRD ($\bar{d}_{exp}$) and theoretically ($\bar{d}_{th}$).

Noteworthy, given the strong influence of the out-of-plane lattice constant on the final T_c value in La_2CuO_4 (see Figure 4.6), these structural aspects could be put in relation (i) with the lower T_c which was measured for the bilayers with respect to the superlattices; (ii) in the case of the superlattices, with the tendency of T_c to decrease for large La_2CuO_4 thicknesses (see Figure 4.22).

4.3 Two-dimensionally doped lanthanum cuprate

The part of the project that will be described in the following is inspired by the concept of delta-doping, which can be defined as the introduction of a very thin slab of doped material in an undoped matrix with the purpose of modifying its structural properties. Delta-doping technique has been extensively implemented in semiconductor technology but has been much less exploited in oxides.[178] In this context, investigations have been mainly performed on delta-doped $SrTiO_3$ in which, by confining the doped phase (typically Nb- or La-doped $SrTiO_3$), improved properties were obtained.[179–181] The limits for the dimension of the delta-doped slab and for the dopant concentration are represented by the substitution of a full, single atomic layer with a single layer of dopant in the undoped structure: such an approach (single-layer delta doping) has been successfully implemented in few cases in simple perovskite structures and has demonstrated its power for tuning electrical conductivity and magnetic properties. For example, the substitution of single layer of SrO with LaO in $SrTiO_3$ was shown to induce electronic redistribution in proximity of the doped layer.[26] A similar effect was observed upon substitution of SrO with GdO in $SrTiO_3$.[182] With respect to magnetic materials, one example is given by the work by Santos *et al.*, in which a metallic ferromagnetic region was formed in superlattices made by single unit cell layers alternation of $LaMnO_3$ (antiferromagnetic insulator) and $SrMnO_3$ (antiferromagnetic metal) as a consequence of charge spread from the metallic to the insulating phase.[183]

However, none of the examples given in literature demonstrated the potential of delta-doping with respect to superconductivity since, to the best of our knowledge, all the reported delta-doped oxide superconducting systems ($SrTiO_3$ /Nb:$SrTiO_3$ / $SrTiO_3$ and La_2CuO_4 /$La_{1.85}Sr_{0.15}CuO_4$ / La_2CuO_4) already exhibit superconductivity also in the bulk form (single phase Nb:$SrTiO_3$ and $La_{1.85}Sr_{0.15}CuO_4$, respectively).[184,185]

Here, we implemented atomic-layer delta-doping in lanthanum cuprate by substituting specific single layers of LaO with SrO. This doping mode can be referred to as two-dimensional or heterogeneous doping, in contrast to the zero-dimensional (also called homogeneous) case in which instead the dopant is ran-

domly dissolved in the matrix. The comparison between zero-dimensional and two-dimensional doping in La_2CuO_4 is given in Figure 4.31. In the first case, Sr is randomly placed in the lanthanum cuprate matrix: the system obeys the electroneutrality condition which predicts the negatively charged Sr defects to be compensated by electron holes and oxygen vacancies located in proximity of each dopant ion (Debye-Hückel situation) thus being homogeneously distributed in the material. Viceversa, by confining the dopant in atomic layers, these play the role of negatively charged surfaces. The situation is governed by space-charge conditions (Gouy-Chapman) which, as a consequence of the built-up (negative) potential, predict the redistribution of the mobile charge carriers within the space charge region. In particular, a sharp increase of the positive defect concentrations (i.e. holes and oxygen vacancies) and the depression of the negative ones (i.e. oxygen interstitials) is expected. The two situations can be formally discussed as follows:[186]

$$\frac{z_k \delta c_k}{\delta q_{\mathrm{dop}}} < 0 \tag{4.2}$$

$$\frac{z_k \delta c_k}{\delta \Sigma_{\mathrm{int}}} < 0 \tag{4.3}$$

Equation (4.2) is valid for the homogeneous case, whereas Equation (4.3) applies to the heterogeneous doping case. For both, z_k is the defect charge number, c_k its concentration. In Equation (4.2), q_{dop} is the effective charge of the dopant (< 0 for Sr substituting La), which is replaced in Equation (4.3) by the effective charge density of the doped layer Σ_{int}.

The two situations are charge-wise similar (they both are expected to give rise to an increase (depression) of positively (negatively) charged defects upon Sr doping), but they are spatially very different as, in the heterogeneous case, a defect concentration gradient is expected for the mobile species. Moreover, in this case the hole distribution does not spatially follow the distribution of the dopant.

Notably, two-dimensional doping presents, with respect to the zero-dimensional case, the possibility of structuring a material at wish (i.e. by defining the position of the doped layer) and to dope the material avoiding the crystallographic

disorder induced by the ionic dopant random distribution, possibly improving the material performance.

4.3.1 Synthesis of two-dimensionally doped La_2CuO_4

The unique possibility of defining the composition of each atomic layer which is given by the ALL-MBE method (see Section 3.1) was employed to the realize two-dimensionally Sr doped La_2CuO_4. In particular, superlattices in which predefined LaO layers were substituted by SrO were synthesized. The nominal composition of the heterostructures can be written as

$$S \text{ x } [(\text{SrO}-\text{LaO}-\text{CuO}_2) + N \text{ x } [(\text{LaO}-\text{LaO}-\text{CuO}_2)]$$

with S being the number of repetitions of a superlattice unit and N the number of La_2CuO_4 blocks (i.e. half a u.c.), deposited as spacing between two Sr-containing La_2CuO_4 blocks. All the samples were grown on $LaSrAlO_4$ (001) substrate.

A two-dimensional representation of the crystal structure is depicted in Figure 4.36a.

The growth conditions were the typical ones for La_2CuO_4, i.e. $T \approx 600$ °C and $P \approx 2.5 \times 10^{-5}$ Torr. Vacuum cooling, starting from $T = 200$ ℃, was carried out in order to exclude any contribution to conductivity due to the insertion of oxygen interstitials. High quality samples were synthesized, as one can infer from the RHEED analysis reported in Figure 4.32. Figure 4.32a displays the time evolution of the specular spot intensity, while the RHEED patterns during different stages of the deposition are shown in Figure 4.32b to Figure 4.32e. The deposition of the SrO atomic layer does not lead to the appearance of any diffraction signal except the one which is typical for La_2CuO_4 (Figure 4.32b), indicating that no secondary phases (e.g. rock-salt SrO, see Ref. 187) are formed. Rather, SrO is deposited as atomic layer in the cuprate matrix. The oscillation amplitude obtained during the deposition of the subsequent LaO and CuO_2 atomic layers is reduced for the initial layers and recovers at a distance of about 4 constituting blocks, i.e. about 2 unit cells, from the SrO layer. Typical diffraction pattern for La_2CuO_4, i.e. 4 extra-bands between the main diffraction streaks (see Figure 4.3e),

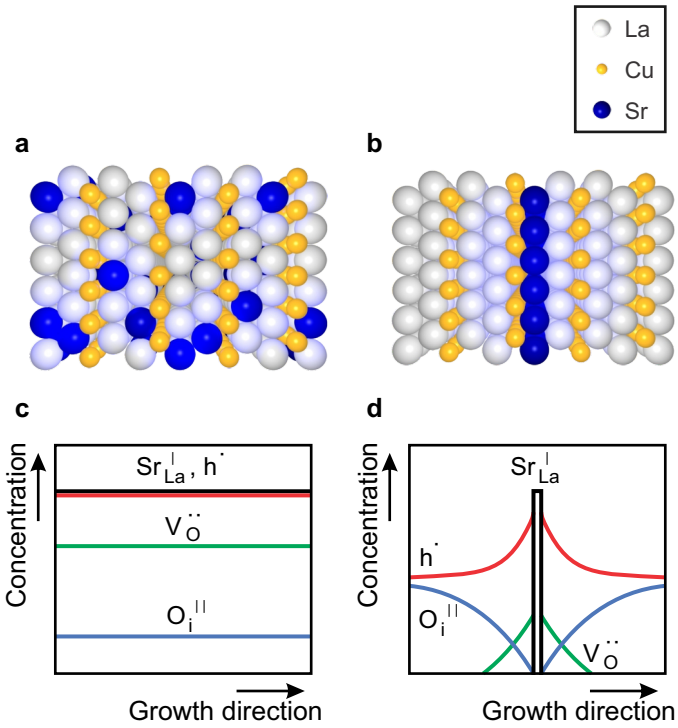

Figure 4.31. In panels (a) and (b) the crystal structures of homogeneously and heterogeneously doped La_2CuO_4 (oxygen atoms are omitted for clarity), respectively, are schematically depicted. In (c) the resulting defect diagram for homogeneous doping, fulfilling the electroneutrality condition, is presented. In (d), expected defect distribution for heterogeneous doping, highlighting the presence of a hole accumulation layer in proximity of the 2-dimensional SrO layer.

is always present (Figure 4.32d and Figure 4.32e), apart from the first two layer after SrO (Figure 4.32c refers in particular to the second layer). This is suggestive of an increased crystallographic disorder at the first layers on top of SrO.

A typical AFM micrograph is reported in Figure 4.33, showing that no secondary phase outgrowths are present. Terraces, which are due to the substrate morphology, are clearly visible and testify that layer-by-layer conditions are maintained throughout the whole growth process.

In Figure 4.34, XRD $2\theta/\omega$ scan is presented. It shows that the structure is c-axis oriented, highly crystalline (see the presence of high index diffraction orders). The magnification of the (004) peak (Figure 4.34b) shows clear superlattice reflections. Finally, an example of XRR analysis, including simulation (using the Parratt formalism see Section 3.3), is reported in Figure 4.35. Very good agreement between the real and the expected thickness is found, confirming the precise control of the growth process.

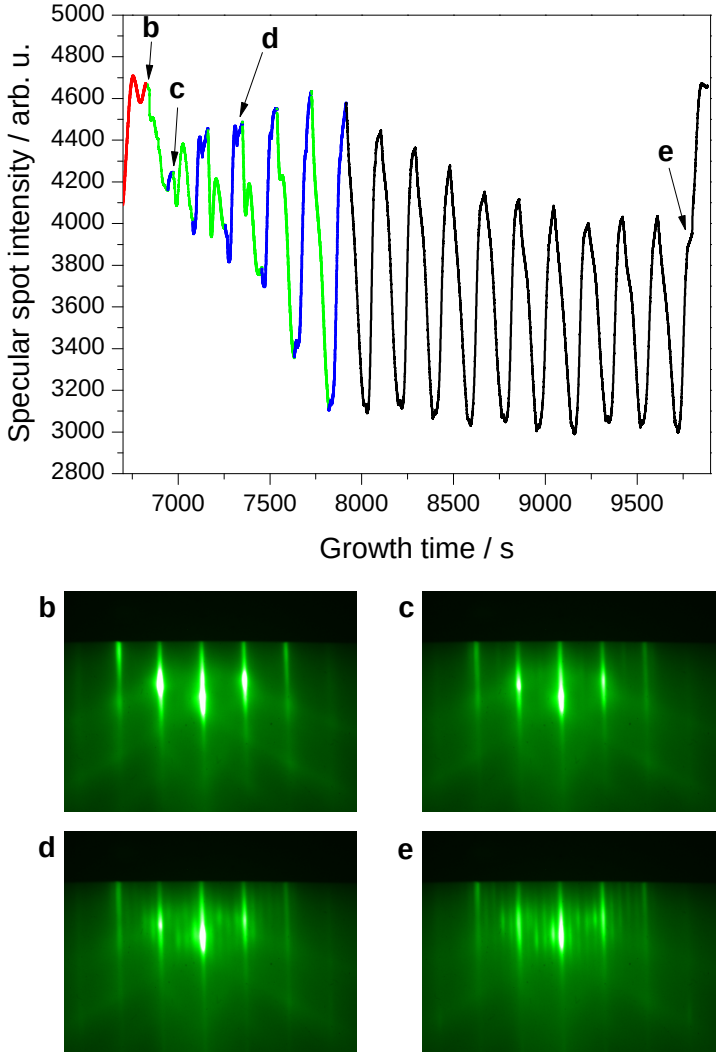

Figure 4.32. RHEED in-situ analysis during the growth of a two-dimensionally doped superlattice period [(SrO-LaO-CuO2 + 15 x (LaO-LaO-CuO2)]. a) Specular spot intensity evolution recorded during the growth of a single superlattice. The different stages of atomic layer deposition are marked with different colors for the first layers (SrO=red, LaO=green, CuO2=blue). Diffraction patterns along the (100) direction, recorded at the end of the deposition of the SrO layer (b), and CuO_2 different layers are reported ((c) to (e)). Reproduced from Ref. 140.

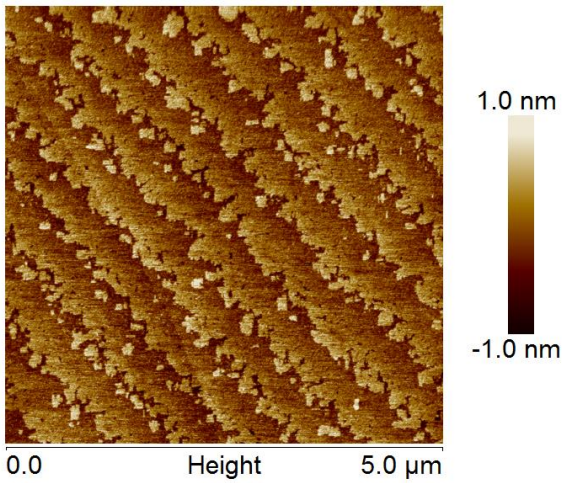

Figure 4.33. 5x5 μm AFM scan of the film surface of two dimensionally-doped La_2CuO_4. R_{ms} is 0.3 nm. Reproduced from Ref. 140.

4.3.2 Results and discussion

Electrical properties

Low temperature electrical conductivity measurements were performed as described in Section 3.5, for several superlattice structures having different spacing N and similar total thickness $\approx$ 400 Å. The results are reported in Figure 4.36b and Figure 4.36c, which show the resistivity data as a function of T and the average T_c value as a function of N, respectively.

Remarkably, despite the nominal composition is not superconducting, being formed by alternating metallic and insulating La_2CuO_4 blocks, the samples exhibit high-temperature superconductivity. Several interesting features can be highlighted from the analysis of the data. First, in-plane resistivity increases for larger N: this suggests that the conducting (and superconducting) phase is located in proximity of the SrO layer (as, by increasing the spacing between the SrO layers, a phase with insulating character is introduced). Second, a certain dependence of T_c with N is evident: an optimal spacing interval N exists ($5 \leq N \leq 9$) to which the maximum T_c ($\approx$ 35 K) corresponds. For lower spacing, T_c decreases: a high hole concentration leading to overdoping (see Section 2.1.3), or structural distor-

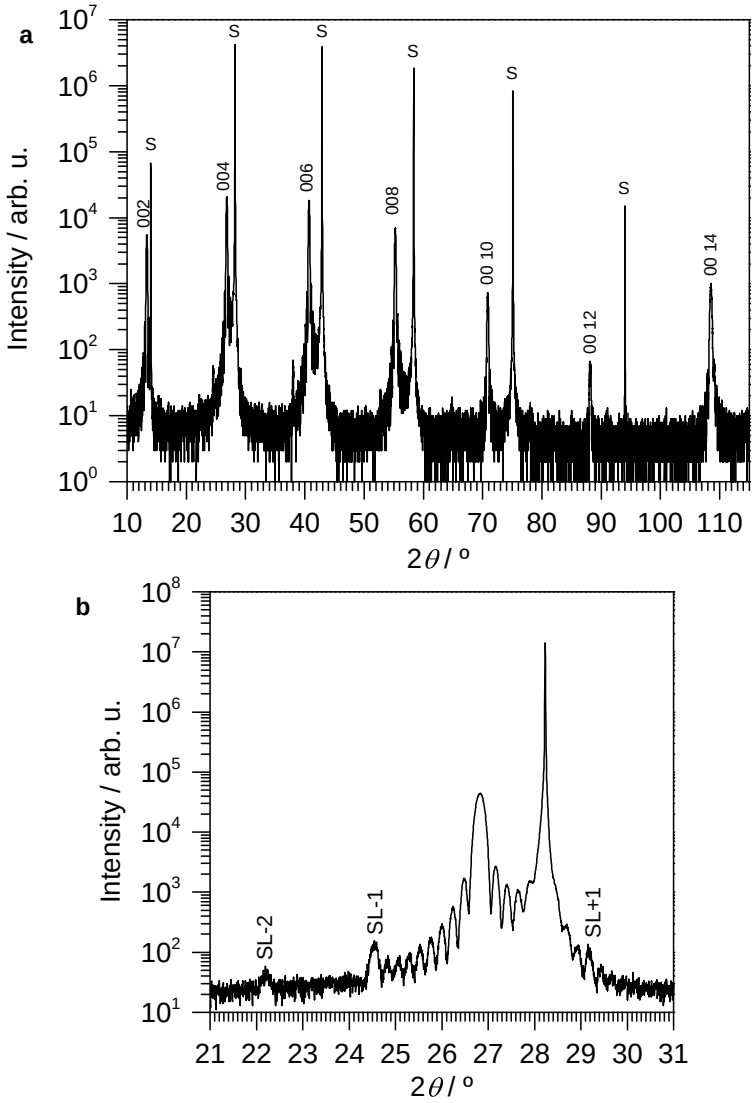

Figure 4.34. XRD of two-dimensionally doped La_2CuO_4 superlattice with structure 10 x [(SrO−LaO−CuO_2 + 5 x(LaO−LaO−CuO_2)]. In (a), fullscan, in (b), magnification around the (004) diffraction peaks. Reproduced from Ref. 140.

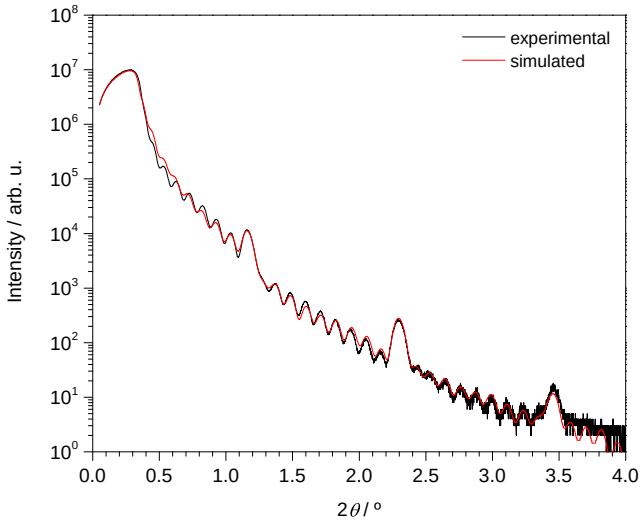

Figure 4.35. Low-angle XRR scan of a thin film of two-dimensionally doped La_2CuO_4 [(SrO-LaO-CuO2) + 5 x (LaO-LaO-CuO2)] x 10 on $LaSrAlO_4$ (001) substrate (black line). The data simulation (red line) results in an average period thickness of 38.56 Å, to be compared with an expected thickness of 39.84 Å. Reproduced from Ref. 140.

tions induced by the SrO layers (see the RHEED patterns analysis in Section 4.3.1) can be both considered as responsible . For higher spacing, T_c saturates at $\approx$ 25 K (please refer to Section 4.3.3 for a possible explanation of this finding).

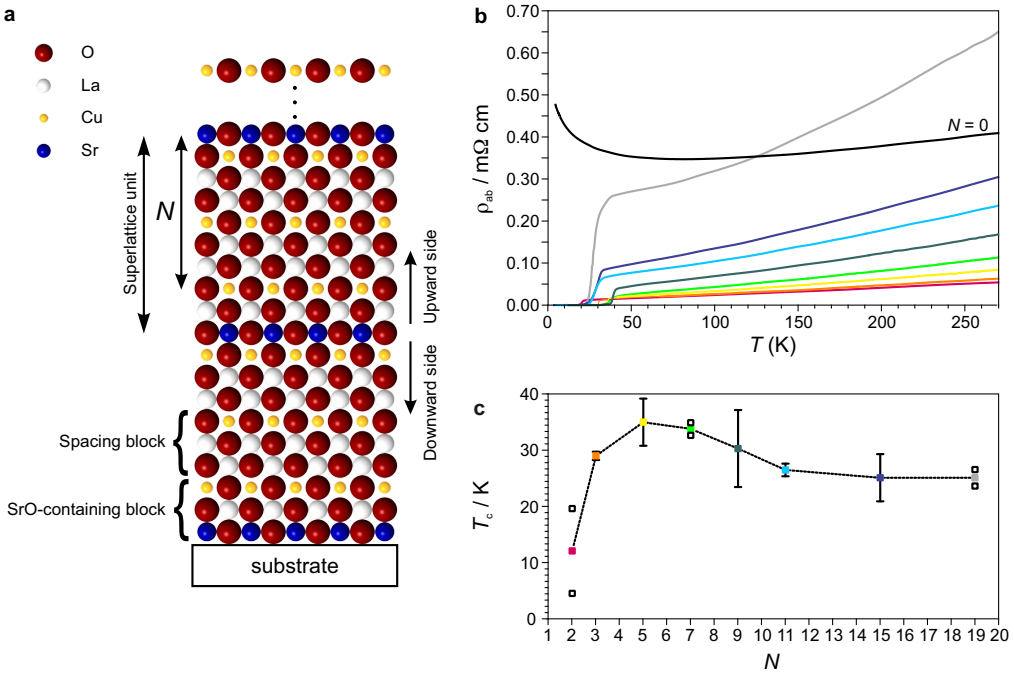

Figure 4.36. a) Sketch of two-dimensionally doped La_2CuO_4. b) Resistivity versus temperature for a set of superlattices having general structure S x [(SrO−LaO−CuO_2) + N x [(LaO−LaO−CuO_2)], for different N (colors are defined as in (c)). c) T_c versus spacing N. The closed symbols refer to the average values, the error bar indicates the standard deviation of the measurements set. For those compositions (value of N), in which a set of two samples was considered for the determination of the average critical temperature, both T_c data points are shown in the diagram (open square symbols). Reproduced from Ref. 140.

TEM characterization

TEM characterization was performed on a representative selection of samples.[2]

Figure 4.37 summarizes the analysis which was performed in order to clarify the cationic distribution. In Figure 4.37a a HAADF image is presented: one can observe the absence of any extended structural defects such as misfit dislocations or antiphase boundaries. Moreover, an alternation between brighter and darker areas, originating from the inhomogeneous Sr distribution (which, due to the lower atomic number, gives darker contrast with respect to La), can be detected. In Figure 4.37b, the HAADF intensity, integrated for the region shown in (a), is presented. Each intensity oscillation (light green line) corresponds to an atomic column. By enveloping the maxima (blue line in Figure 4.37b), one can retrieve more precise informations about the extension of the Sr-doped areas: remarkably, a certain redistribution is present, i.e. Sr is not perfectly confined into a single atomic layer.

More precise insights could be obtained by spectroscopic methods (EDXS and EELS), results of which are presented in Figure 4.37c (linescan over the whole area shown in a) and Figure 4.37d (linescan over the dark blue line of Figure 4.37a), respectively. Single atomic column resolution (step-size $\approx$ 2 Å) allows one to highlight that Sr not only underwent a spatial redistribution, but also that its concentration profile is highly asymmetric. In particular, while the downward side of the interface (i.e. the side facing the substrate, cf. Figure 4.36a) is sharp (the redistribution width is 0.9 ± 0.2 nm), the upward side (in the growth direction), shows a Sr distribution profile which extends for 2.3 ± 0.4 nm. Such a feature, which is ascribable to thermal diffusion and to the growth kinetics for the downward side and the upward side of the interface, respectively, will be analyzed in detail in Section 4.3.4.

TEM spectroscopy also allowed for a quantitative analysis of Sr concentration. In particular, by appropriately scaling the EDXS Sr-L and La-L intensity

[2]Observations and analyses were processed by Dr. Yi Wang at the StEM group (Prof. Van Aken), Max Planck Institute for Solid State Research (Stuttgart).

in the substrate region (where [Sr]/[La]=1), we could obtain the concentration ratio of the two cationic species in each atomic column: the maximum [Sr]/[La] is 0.21 ± 0.02.

EELS analysis allowed us to obtain a direct measurement of the Sr and hole distribution profiles, by averaging the Sr-$L_{2,3}$ edge (for Sr) and the oxygen-K (O-K) edge pre-peak (for holes), which were obtained over several Sr-containing regions. In particular the O-K edge pre-peak, which is also called mobile carriers peak (MCP),[33] is ascribed to the electronic transitions from O_{1s}-core-level to hole states with p symmetry in the valence band and therefore its intensity is proportional to the hole concentration.[33,143] The MCP intensity, which was retrieved upon subtraction of a reference spectrum taken from undoped, insulating La_2CuO_4 (Figure 4.38), is plotted together with the Sr-$L_{2,3}$ edge intensity in Figure 4.39. Interestingly, by comparing the two profiles, one observes that, while the resulting Sr distribution is asymmetric (as already detected by the EDXS analysis), the hole profile is symmetric around the nominal position of the SrO layer. This is indicative of clear decoupling between ionic dopant and mobile electronic charges.

EELS analysis was also used in order to obtain quantitative informations about the Sr and holes distribution profiles, i.e. the number per formula unit that can be assigned to each La_2CuO_4 *unit-block* (constituted by a CuO_2 plane and the surrounding $La_{1-x}Sr_xO$ charge reservoir layers). By averaging the data points of the plots shown in Figure 4.39 in order to assign a single Sr-$L_{2,3}$ and MCP intensity value to each unit-block, and by normalizing the sum of the intensities in order to fulfill the nominal stoichiometry and electroneutrality, we were able to obtain the Sr and hole concentration profiles as depicted in Figure 4.40. Remarkably, at the upward side hole and Sr profiles almost perfectly overlap, as one would expect for a classical homogeneous doping situation, whereas at the opposite side there is a clear decoupling between holes and Sr ions. In particular, to the excess of negative charge in the first unit-block (the one to which the CuO_2 plane marked with $P_{Cu} = -1$ belongs), corresponds an excess positive charge at planes $P_{Cu} = -2, -3$. This finding points towards the presence of an heterogeneous doping mode at the backward side interface and has been further confirmed independently by

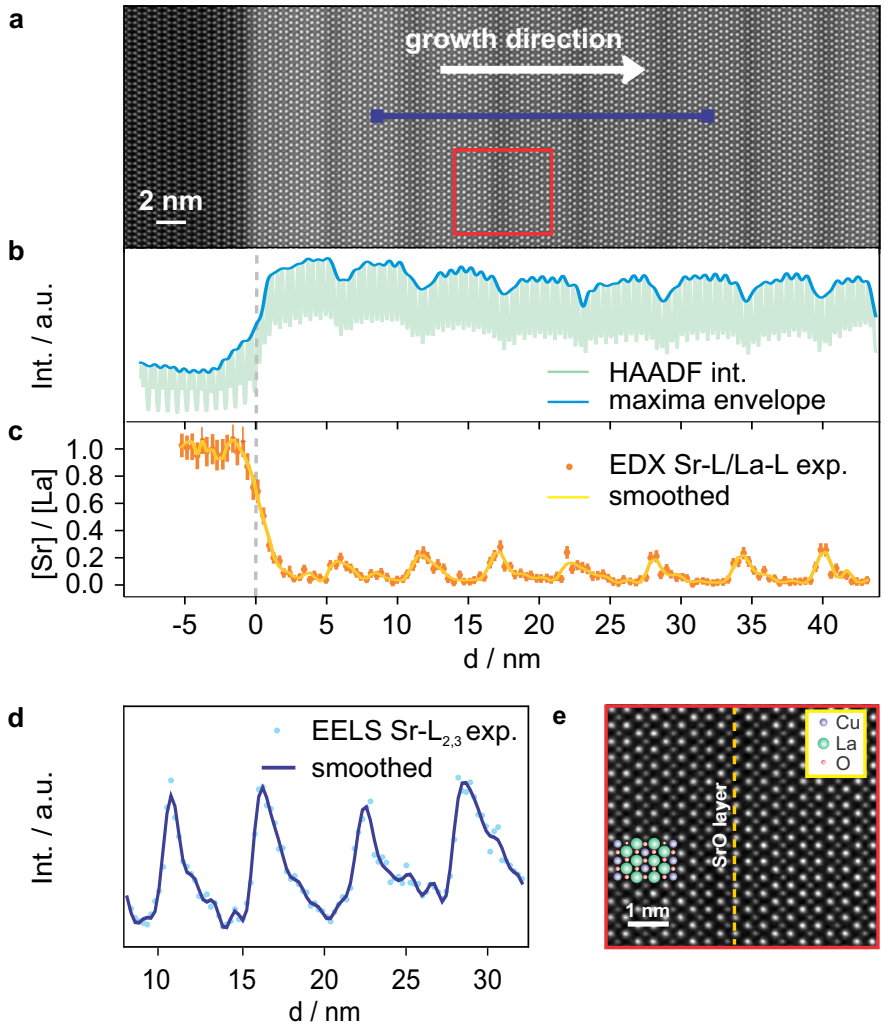

Figure 4.37. a) HAADF analysis of two-dimensionally doped La_2CuO_4 ($S = 8$, $N = 7$). The intensity modulation (quantitatively reported in panel (b)), highlights the alternated Sr-doped and pure La_2CuO_4 areas. In figure (e), a magnification of the area identified by the red square in (a), showing the atomic arrangement, is presented. c) [Sr]/[La] profile, extracted from analysis of La-L and Sr-L EDX lines. The error bars indicate the standard error. d) Result of the integration of the EELS Sr-$L_{2,3}$ line profile acquired along the line marked in dark blue in panel (a). The error bars are the standard error. Reproduced from Ref. 140.

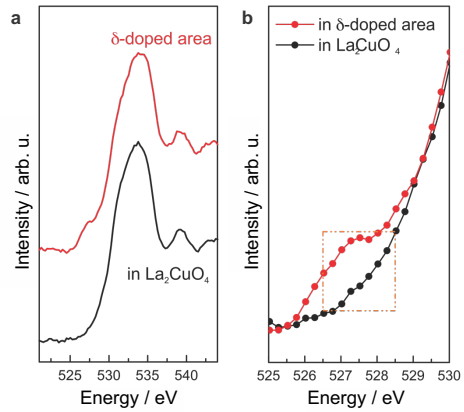

Figure 4.38. a) Oxygen-K edge from two-dimensionally doped La_2CuO_4 (red), and from La_2CuO_4 (black), respectively, highlighting the differences in the near-edge fine structure. In the hole-enriched region, a pre-peak can be clearly seen. b) Magnification of the pre-peak region. Reproduced from Ref. 140.

complementary tests, as described below. At the upward side instead, Sr and holes profiles are coupled, as one would expect in the case of an homogeneous doping mode.

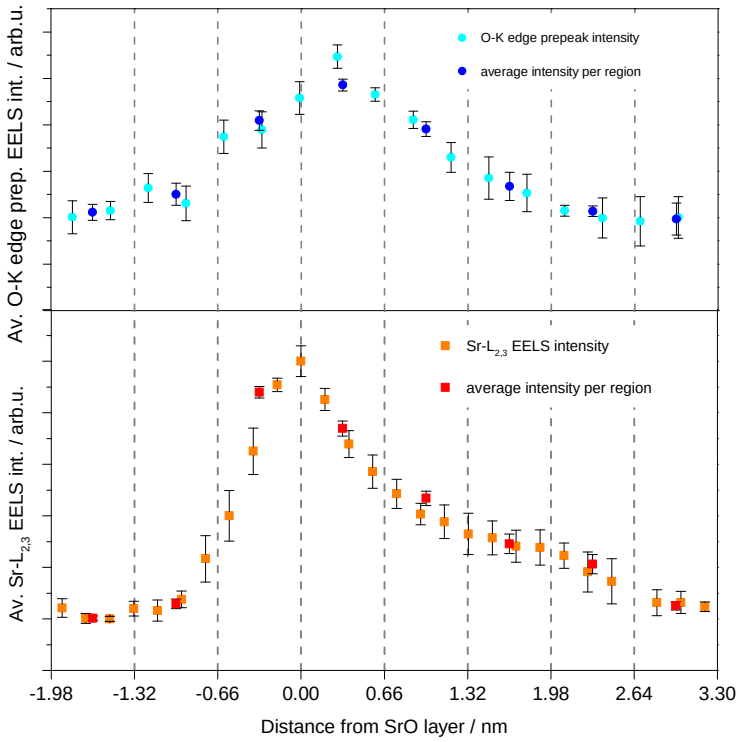

Figure 4.39. STEM-EELS analysis of the O-K edge pre-peak and of the Sr-$L_{2,3}$ edge. Experimental data for holes (O-K edge pre-peak) and Sr (Sr-$L_{2,3}$ edge), obtained by averaging the intensity profiles of different line scans, are indicated in light blue and orange, respectively (the standard error is indicated by error bars). The dashed lines mark the regions corresponding to each (La,Sr)O$-CuO_2-$(La,Sr)O unit-block. The data obtained as weighted mean for each region are shown in dark blue (for holes) and red (for Sr). For the holes, the intensity is expressed as the result of the subtraction of the reference spectrum referring to undoped La_2CuO_4 . The error bars result from the averaging process. Reproduced from Ref. 140.

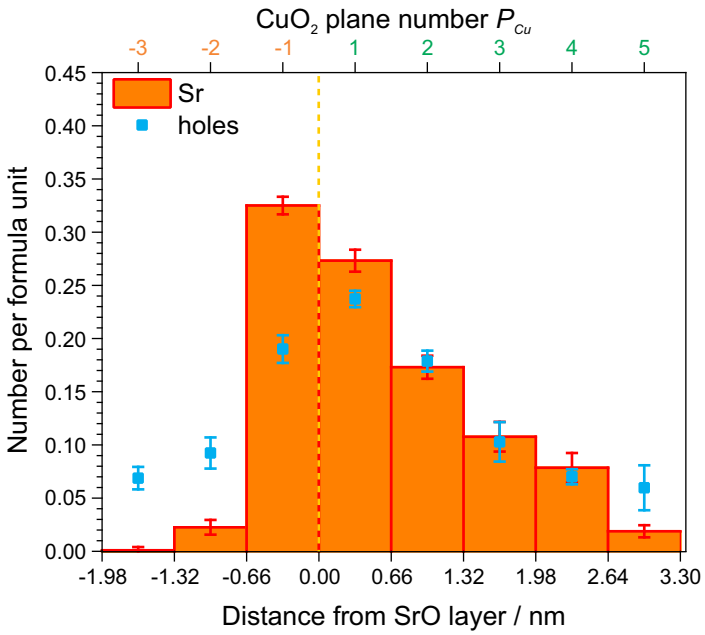

Figure 4.40. Sr and holes per formula unit, as obtained by STEM-EELS data analysis. Reproduced from Ref. 140.

Zinc-tomography

Zn-tomography is a successful technique for the spatial mapping of superconductivity. It is well-known that the substitution of Cu with Zn leads to a strong reduction of T_c in cuprates.[188,189] This has been applied in recent years in an epitaxial system based on lanthanum cuprate, in order to precisely locate the superconducting layers.[32] This technique is known in literature as "Zn-tomography" and is based on the measurement of the residual T_c which persists after the insertion of a small amount of Zn (about 3% a.t.) in selected CuO_2 planes. Since such a doping procedure leads to the reduction of T_c only of the doped CuO_2 plane (as long as the Zn concentration is kept low enough to make diffusion to neighboring planes negligible), then the plane (or the planes) whose Zn-doping gives the highest reduction of T_c can be identified as the responsible for high-temperature superconductivity .

We first tested the feasibility of such a technique on ultra-thin (2 u.c.), opti-

mally doped $La_{1.84}Sr_{0.16}CuO_4$, which has $T_c \approx 20$ K. Upon Zn-doping we observed a dramatic reduction of T_c (≈4 K), as shown in Figure 4.41. It should be noticed that, by reducing the thickness to 2 u.c., we could minimize possible extrinsic effects on T_c due to the formation of secondary phases such as ZnO.

We applied the "Zn-tomography" technique in a set of samples of two-dimensionally doped La_2CuO_4, in which only one SrO layer was inserted. The formal structure is:

$$[8\,\mathrm{x}(\mathrm{LaO}{-}\mathrm{LaO}{-}\mathrm{CuO_2}) + (\mathrm{SrO}{-}\mathrm{LaO}{-}\mathrm{CuO_2}) + 8\,\mathrm{x}(\mathrm{LaO}{-}\mathrm{LaO}{-}\mathrm{CuO_2})].$$

The outcome is shown in Figure 4.42, in which the average residual T_c (solid squares) is plotted as a function of the CuO_2 plane doped by Zn. The numbering of the CuO_2 is made in agreement with Figure 4.40.

The result highlights several interesting aspects. Let us first focus on the backward side of the interface, which we analyzed upon suppression of T_c of the upward side (to obtain this, all the CuO_2 planes belonging to that region were doped by Zn). We found that this region, despite the sharp Sr profile, is superconducting ($T_c \approx 25$ K, red band in Figure 4.42b). Interestingly, the selective doping of the different CuO_2 planes indicates that the strongest T_c suppression is obtained when the second plane ($P_{Cu} = -2$ in Figure 4.42) is doped by Zn, providing a precise indication that this plane is the major source for high-temperature superconductivity at the backward side. This is in very nice agreement with the spectroscopic results (Figure 4.40), which indeed indicated the right hole concentration for superconductivity for $P_{Cu} = -2$ (≈ 0.1 holes/CuO_2). Even the quantitative agreement is good since, to such a hole concentration, $T_c \approx 25$ K is expected, which is corresponding to the actual T_c of the backward side.[32,63] Most importantly, since a very low Sr content (≈ 0.02) was obtained from EELS analysis (Figure 4.39) (far lower than the threshold required for the superconducting transition in $La_{2-x}Sr_xCuO_4$), this tells us that homogeneous doping cannot be accounted for high-temperature superconductivity at the downward side. Rather, a heterogeneous doping mode has to be considered. It is also worth noticing that the confinement of high-temperature superconductivity to a single CuO_2 plane,

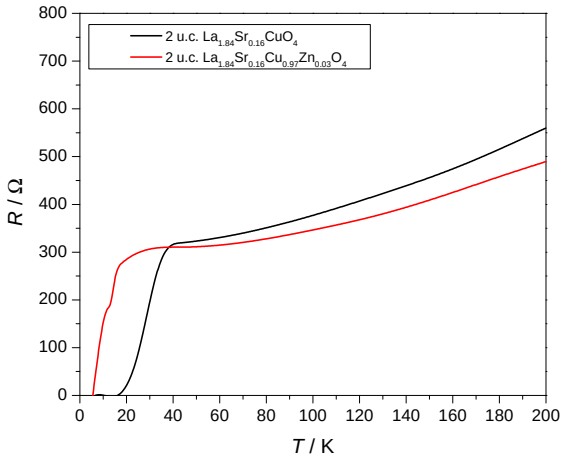

Figure 4.41. Resistance versus temperature for 2 u.c. thick $La_{1.84}Sr_{0.16}CuO_4$ and with $La_{1.84}Sr_{0.16}Cu_{0.97}Zn_{0.03}O_4$. Reproduced from Ref. 140.

as obtained here, is not achievable by homogeneous doping, as the thinnest superconducting $La_{2-x}Sr_xCuO_4$ phase which is reported has a thickness of 1 u.c. (which contains 2 CuO_2 planes).[152,184] This finding can be related to the absence of crystallographic disorder in the heterogeneous doping case, which instead is intrinsically introduced when Sr is randomly dissolved in La_2CuO_4. A similar observation was made by Logvenov *et al.* for the related $La_{2-x}Sr_xCuO_4$ / La_2CuO_4 system.[32]

In order to rule out any major contribution to high-temperature superconductivity coming from the backward on the upward side, plane $P_{Cu} = -2$ was doped by Zn in all the samples. The reference T_c in this case (as obtained by doping only $P_{Cu} = -2$ with Zn), was found to be $T_c \approx 20$ K (green band in Figure 4.42) In this case it was not possible to assign high-temperature superconductivity to any specific CuO_2 planes by singularly doping each of them, meaning that several planes contribute simultaneously to the superconducting properties of this side of the interface. This is consistent with an homogeneous doping mode, according to which we predict a relatively large superconducting volume (about 1.5 u.c. i.e. 3 CuO_2 planes, cf. Figure 4.39) as a consequence of Sr doping. This again matches the conclusions drawn from the STEM-EELS measurements.

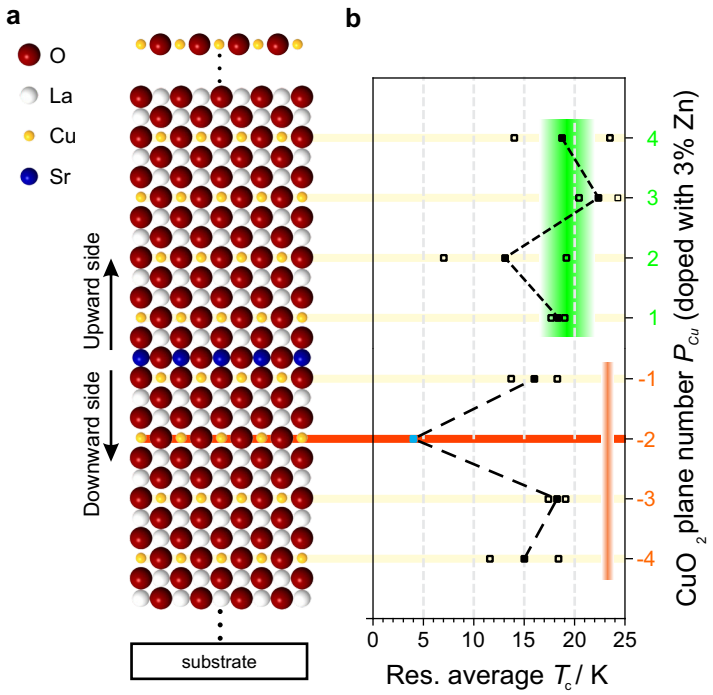

Figure 4.42. (a) Sketch of the symmetric structure investigated by Zn-tomography. (b) average residual T_c (solid squares) as a function of the Zn-doped CuO_2 plane P_{Cu}. The indicated T_c value for $P_{Cu} = -2$(closed light blue square) has to be considered as an upper limit, since the critical temperature for the samples was below the low limit for our measurements (4 K). Reference T_c for the upward and downward sides are indicated in green and orange, respectively. Open squares represent the single data points. Reproduced from Ref. 140.

Comparison with La_2CuO_4 / SrO bilayer

A dedicated experiment was performed in order to rule out any role of cationic intermixing (yet, as already demonstrated, very limited and not the main responsible for high-temperature superconductivity) for the occurrence of high-temperature superconductivity at the backward interface. We studied the properties of a bilayer structure made by La_2CuO_4 and a thick SrO layer: this type of structure is, from the point of view of growth dynamics for the downward interface, very similar to the one reported in Figure 4.42, with the only exception that here several SrO layers are deposited in sequence. Therefore, a similar La / Sr intermixing width can be expected in two cases. The substantial difference between the two systems is the charge of the SrO layer: in the delta-doped system SrO is negatively charged, whereas it represents a neutral plane in case of the La_2CuO_4 /SrO bilayer.

The electrical properties of such a structure are depicted in Figure 4.43b. The structure exhibit neither high-temperature superconductivity nor metallic behavior. One could in principle argue that such a finding can be simply related to the SrO phase acting as an insulating capping layer, eventually screening a possible contribution to the conductivity of the sample which deriving from La_2CuO_4. In order to rule out this possibility, we performed magnetic susceptibility experiments (see Section 3.5.1), demonstrating that no superconducting transition is present in the bilayer (Figure 4.44). This confirms once more the negligible role of cationic intermixing at the downward side of the interface and further highlights the key role of the negatively charged planes obtained by substituting LaO planes with SrO ones.

Realistic picture of charge distribution

The resulting charge distribution in the doped area of La_2CuO_4 is depicted in Figure 4.45. The Sr profile (black) is highly asymmetric: smeared in the growth direction (upward side), sharp in the opposite (downward). At the upward side, hole distribution (red line) follows the Sr profile, in agreement with the homogeneous doping case (cf. Figure 4.31a). A negatively charged area, resulting from the

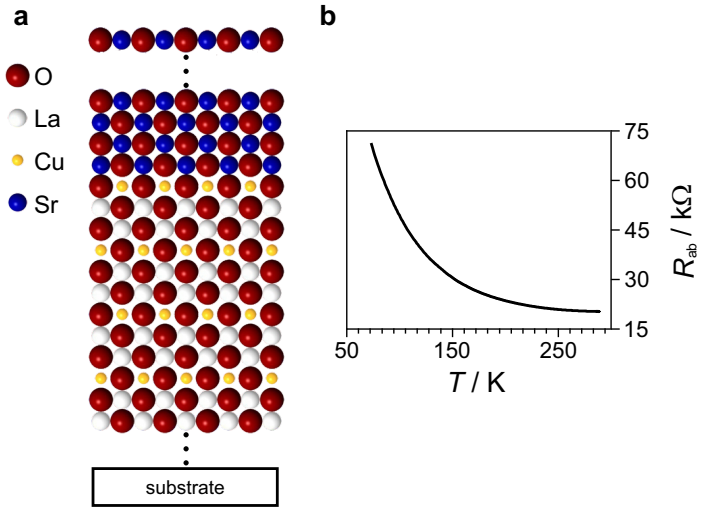

Figure 4.43. (a) Sketch of the bilayer La_2CuO_4 / SrO structure, to be compared with Figure 4.42a. (b) Electrical properties of 15 u.c. La_2CuO_4 / 10 u.c. SrO. Reproduced from Ref. 140.

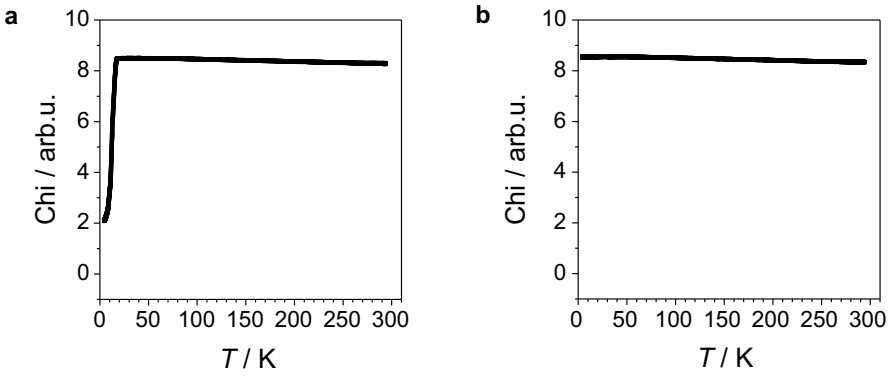

Figure 4.44. Magnetic susceptibility measurement for (a) two-dimensionally doped La_2CuO_4 structure, as depicted in Figure 4.42a (in the case of all the $P_{Cu} > 0$ are doped by Zn) and (b) for a La_2CuO_4 / SrO bilayer (as depicted in Figure 4.43b). Reproduced from Ref. 140.

disproportion between Sr and holes (as highlighted by STEM-EELS analysis), is present in correspondence of the maximum Sr content. In the space-charge picture, this can be viewed as a negatively charged surface requiring hole compensation at the left-hand side of the interface. Therefore, an hole accumulation layer is formed yielding superconductivity at the backward interface (heterogeneous doping). Notably, we expect a metallic ("overdoped") phase to be present in close proximity to the SrO layer, where the hole distribution is maximum.

Ignoring electronic charge localization on the CuO_2 planes i.e. considering a continuum approximation, the different mechanisms of hole distribution at the two interface sides can be depicted as in Figure 4.46. While, on the left-hand side (downward), a semi-infinte space-charge zone is formed, on the other side we face a sequence of finite, almost flat, contributions.

4.3.3 Relation between structural and superconducting properties

In a similar way to what was already proposed in the case of the $La_{2-x}Sr_xNiO_4$ / La_2CuO_4 heterostructures (see Section 4.2.3), also here it is worth considering the relation between the *c*-axis (which is affected by the out-of-plane electrostatic interactions in the ionic crystal structure i.e. "Madelung strain") and the measured T_c values as a function of the spacing N between the SrO-containing blocks (Figure 4.47).[69]

Note that in the top panel of Figure 4.47, two values of c are displayed, namely, c_{exp}, as obtained by XRD (red symbols), and c_{theo} (blue symbols), which is the expected theoretical value of c obtained according to Equation (3.4):

$$c_{theo} = \frac{c_{cond} \times M + c_{ins} \times (N + 1 - M)}{N + 1} \tag{4.4}$$

where c_{cond} is the lattice parameter of the (super)conducting phase, c_{ins} the lattice parameter of the insulating phase, M the thickness of the (super)conducting phase and $N+1$ the total thickness of one superlattice cell (cf. Figure 4.36). Note that both M and N are expressed as numbers of La_2CuO_4 constituting blocks.

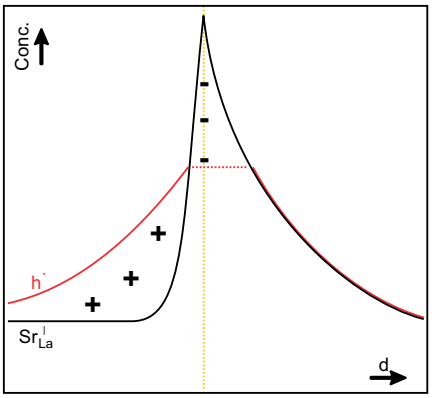

Figure 4.45. Realistic picture of Sr (black) and holes (red) distributions. The nominal position of the SrO layer is marked by the dotted yellow line. Reproduced from Ref. 140.

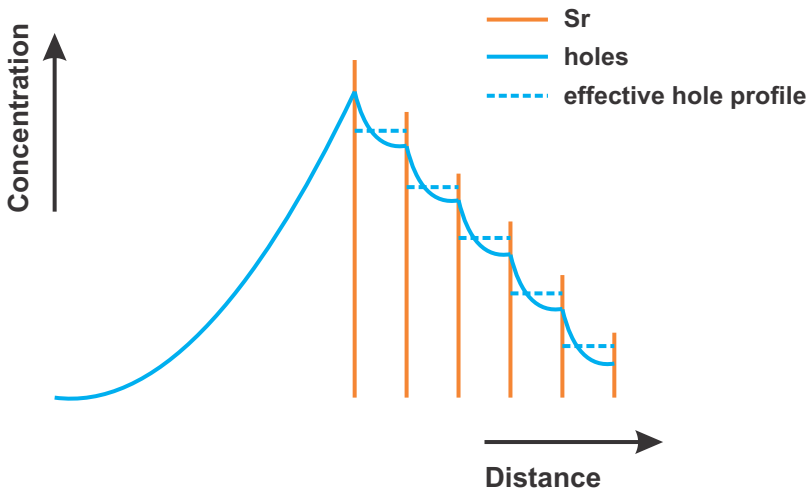

Figure 4.46. Holes concentration profile expected in a continuum approximation. Reproduced from Ref. 140.

Here the thickness of the (super)conducting phase is assumed to be $M = 6$ (cf. P_{Cu} ranging from -2 to 4 in Figure 4.40) while the lattice parameter of the insulating phase is $c_{ins} = 13.11$ Å (see Figure 4.6). At $N = 5$ (i.e. when 6 constituting blocks of La_2CuO_4 are present), $c_{cond} = c_{exp}$.

From the data shown in Figure 4.47, a good agreement between c_{theo} and c_{exp} can be recognized. In particular, for $7 \leq N \leq 11$, we can observe a decrease of both c_{theo} and c_{exp}. At first, this could be rationalized by simply considering the increasing volume fraction of the insulating phase (i.e. N increases over M). However such an explanation is not consistent with the simultaneous reduction of the T_c values since the total hole distribution is not expected to be influenced by N (as long as N, namely the distance between two subsequent SrO planes, is larger than the extent of the zone where the hole accumulation occurs). Therefore, the decrease of the c-axis together with the drop of the T_c values suggest (given the strong influence of the structural parameters on the superconducting properties i.e. T_c is linearly dependent on c), that for increasing N (in the range $7 \leq N \leq 11$) c_{cond} tends to shrink.

Interestingly, for $N > 11$ the values of c_{theo} and c_{exp} tend to diverge with the latter saturating at about 13.2 Å, while c_{theo} approaches c_{ins}. Since, in this range of N, c_{ins} contributes the most to the value of c_{theo}, this behavior means that the values of c_{ins} are larger than expected.

The resulting picture indicates that c_{cond} and c_{ins} mutually adapt to each other such that $c_{exp} \simeq c_{cond} \simeq c_{ins}$. Noteworthy, this finding allows for reconciliation with all the experimental findings: (i) by introducing an insulating phase ($7 \leq N \leq 11$), c_{cond} shrinks and T_c decreases; (ii) at the same time, c_{ins} is expanded, so that c_{exp} does not further decrease for $N > 11$; (iii) the relation $c_{exp} \simeq c_{cond}$ is experimentally corroborated if we plot c_{exp} versus T_c (Figure 4.48), resulting in a linear relation which is very similar to what was found for single phase La_2CuO_4 (see Figure 4.6). This indeed is suggestive that c_{exp} is the effective c-axis parameter of the superconducting phase rather than a simple average between c_{cond} and c_{ins} . Obviously, further analysis of possible local distortions of the lattice (i.e. by high resolution STEM imaging) should be carried out in order

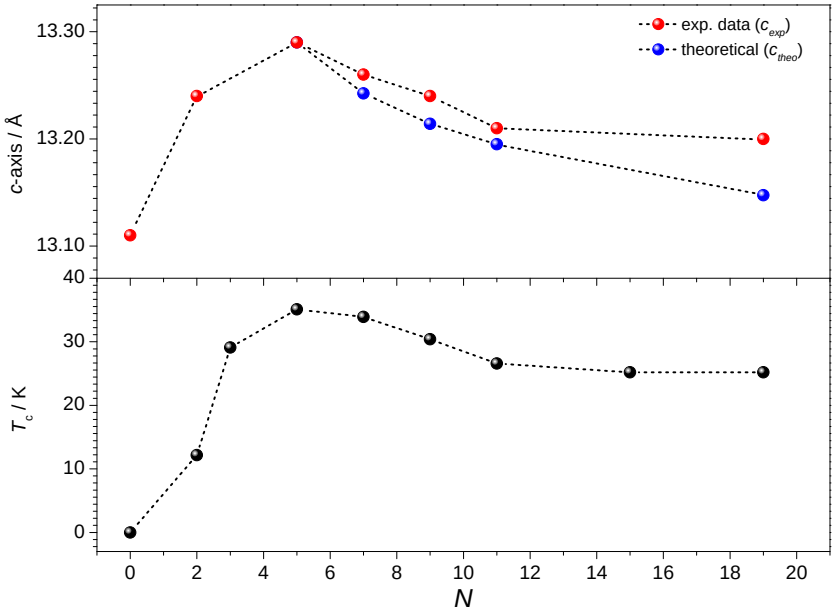

Figure 4.47. Top: experimental and theoretical c-axis lattice parameter as a function of the spacing N for two-dimensionally doped La_2CuO_4. Bottom: T_c versus N (as in Figure 4.36c).

to provide a direct evidence of such an interpretation of the experimental data.

4.3.4 Asymmetric cationic redistribution

Asymmetric cationic redistribution is common in delta-doped semiconducting systems (under the name of "Muraki segregation profile"),[190,191] but has seen only partial disclosure in the field of oxides superlattices and delta-doped systems.[171,172,192]

Some considerations can be made concerning the mechanism of Sr smearing. Let us first consider thermal diffusion. Starting from a delta-distribution, diffusion would occur according to:[193]

$$N_{dop}(x) = \frac{N_{dop,0}}{\sqrt{4\pi Dt}} \exp -\frac{x^2}{4Dt} \tag{4.5}$$

where $N_{dop}(x)$ and $N_{dop,0}$ are the dopant concentration at distance x from the position of the two-dimensional layer and the initial doping concentration,

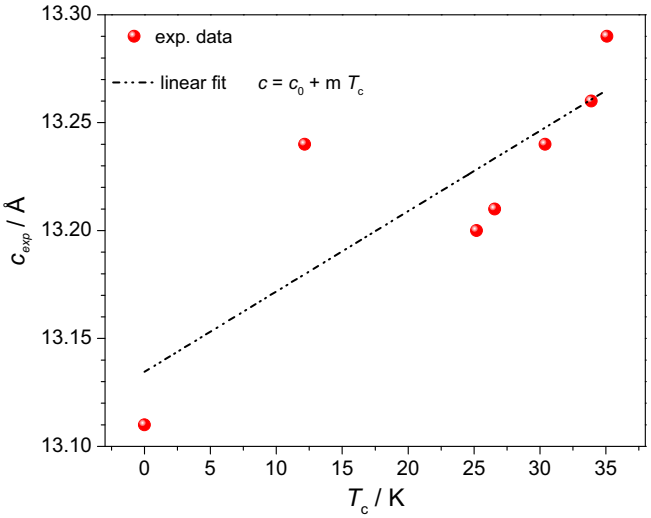

Figure 4.48. c_{exp} versus T_c for two-dimensionally doped La_2CuO_4. The fitting parameters are $c_0 = 13.134 \pm 0.029$, m$=0,037 \pm 0.001$. The residual sum of squares is 0.6.

respectively, D is the diffusion coefficient and t the diffusion time. This expression predicts an evolution into a symmetric Gaussian distribution profile, which is not consistent with the experimental findings describing instead a strongly asymmetric situation. Thus, this explanation can be discarded at least for what concerns the upward side for the interface.

The problem of intermixing occurring in the growth direction can be disentangled by allowing some intermixing to occur only at the film surface, i.e. between the last "La_2CuO_4 constituting block" (i.e. the last LaO-LaO-CuO_2 atomic layers on the film surface) and the incoming particles. This may be connected with the high mobility, due to the incomplete bonds, of the atoms at the film surface and with the observed roughness of the films (see Figure 4.33). Moreover, intermixing is supported by the kinetic energy of the incoming particles (≈ 0.1 eV for a typical MBE process).[194,195]

If one considers thermodynamical equilibrium, an assumption which may by justified by the very slow growth rate of the MBE process (see Section 3.1), some simple semi-quantitative considerations can be proposed. In particular, if we allow

for an equilibrium condition to be established between the last La_2CuO_4 block on the surface and the"incoming La_2CuO_4 block", by entropic effects these two would undergo cationic intermixing until they are equal in composition, i.e. the Sr content is equally distributed between the two. By iterating the mechanism (a graphical representation of the process is presented in Figure 4.49), each La_2CuO_4 constituting block (number with the index n, with $n = 2$ being the nominal two-dimensionally doped block) receives a Sr amount such that:

$$\frac{[Sr'_{La}]}{[La^{\times}_{La}]} = \frac{1}{2^n} \tag{4.6}$$

Such a Sr distribution is graphically represented in Figure 4.50. Notably, it predicts the smearing of the dopant for about 2.5-3 La_2CuO_4 blocks (i.e. 2.6-3 nm), which is in very good agreement with the observed value.

An alternative explanation is based on the dopant segregation towards the surface, which has been already observed for single phase thin films of oxides.[196] In this case, the dopant migrates towards the film surface during the growth process as a consequence of: (i) the elastic strain induced by the ionic size mismatch with the replaced La atom; (ii) the possible presence of a positive electrostatic potential at the free surface which attracts the negatively charged Sr defects (surface space-charge layer). The presence of a surface space-charge layer has been experimentally proved for perovskite systems and is justified by the abundance of oxygen vacancies at the surface, which are formed as a consequence of surface energy minimization effects.[105,197] It should be also noticed that dopant segregation has been theoretically predicted for $La_{2-x}Sr_xCuO_4$ and perovskite systems in general.[198–201]

In order to investigate the role of dopant segregation and more specifically of cationic size mismatch, we studied the effect of replacing Sr with Ba and Ca in two-dimensionally doped La_2CuO_4. The electrical properties, shown in Figure 4.51, exhibit superconducting behavior for all cases. Representative T_c values are summarized in Table 4.2. It should be mentioned that, for the Ba-doped system, we systematically observed the tendency to form secondary phases during growth. As a matter of fact, we could successfully synthesize only few samples which did not

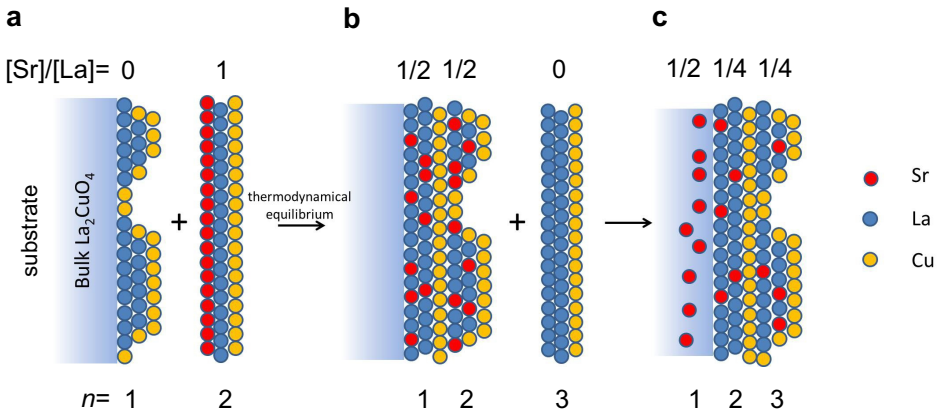

Figure 4.49. Sketch of the cationic intermixing process between the two superficial layers of La_2CuO_4. In panel (a), the last undoped La_2CuO_4 "constituting block" (labeled with $n = 1$) is depicted on the surface of the film, together with the incoming two-dimensionally doped La_2CuO_4 block ($n = 2$) (please note that, for simplicity, the growth process is pictured as "block-by-block" deposition, rather than as the real atomic-layer by atomic-layer). Here the film (excluding the last La_2CuO_4 constituting block) is labeled as "bulk La_2CuO_4". In (b), imposing the equilibrium conditions to be verified between the blocks $n = 1$ and $n = 2$, Sr is equally distributed between these two. Afterwards, when the next block ($n = 3$) is deposited, the situation evolves as pictured in (c): $n = 1$ now pertains to the bulk phase i.e. is no more involved in the mixing process, whereas the blocks $n = 2$ and $n = 3$, which are in thermodynamical equilibrium, share the same Sr amount. By iterating the process, a Sr distribution as depicted in Figure 4.50 results.

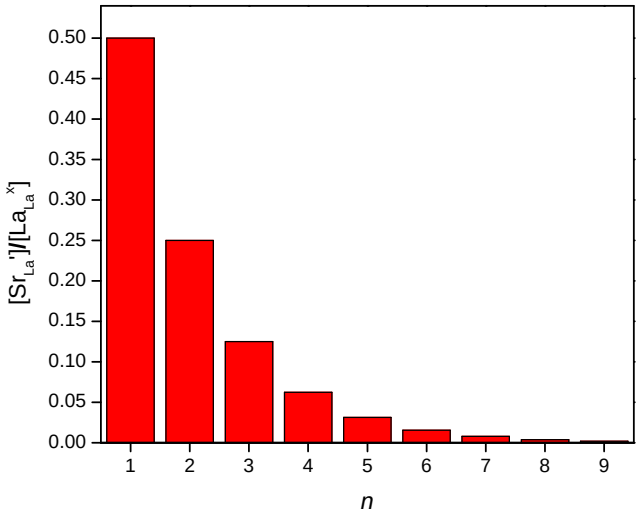

Figure 4.50. Expected Sr distribution in the growth direction as a consequence to entropic effects (according to Equation (4.6)).

exhibit the presence of outgrowths according to RHEED and AFM. We believe that the lower solubility of Ba should be related to the higher cationic size mismatch of such a specie. The broad superconducting transition which we measured for the Ba-doped sample could be attributed to such structural "imperfections".

The width of the dopant redistribution profiles, resulting from the STEM-EELS analysis of the samples, are summarized in Table 4.3 for the three cases. The data are obtained as an average over 3-4 different delta-doped areas. The cationic mismatch with the substituted lanthanum cation is reported for an immediate

	$T_{c,0.9}$ (K)	T_c
Ca-doped	25.7	17.3
Ba-doped	34.7	20.5
Sr-doped	40.7	37.2

Table 4.2. Representative T_c values for two-dimensionally doped La_2CuO_4 for different dopants.

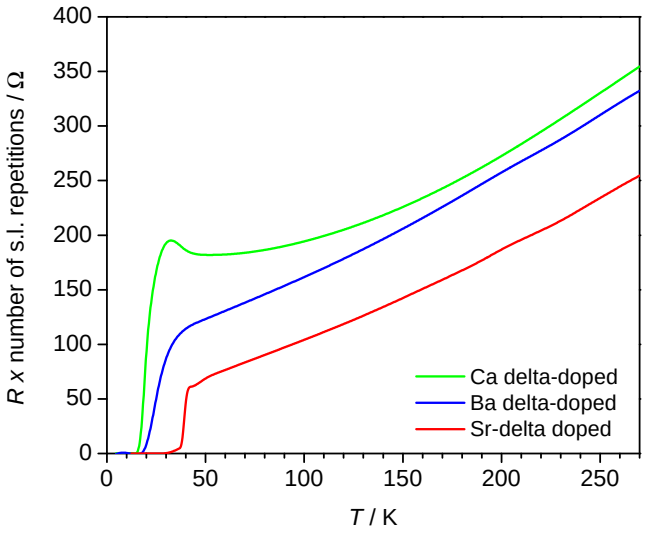

Figure 4.51. Resistance versus temperature for two-dimensionally M-doped La_2CuO_4 (M=Ba, Sr, Ca), having $N = 9$. In order to allow for a direct comparison, the resistance values have been multiplied for the number of superlattice repetitions.

comparison (see also Section 2.1.1).

Focusing on the upward interface, one recognizes that no clear relation can be inferred between the extension of the dopant redistribution and the cationic size mismatch with La, as the smearing width is comparable for all the three cases. This is indicative that, between the two possible redistribution mechanisms described above i.e. the one based on entropic effects and the one taking into account dopant segregation for steric reasons, the first seems to be more likely as in this case segregation occurs independently of the ionic radius.

At the other side instead (downward), redistribution is promoted for Ca, which has the lowest cationic radius, whereas it limited in case of Ba and Sr. This finding points towards thermal diffusion as the responsible for intermixing at the downward side of the interface, since, in this case, a role of the ionic radius is expected (in particular, here diffusion appears to be faster for the ion having smaller radius). Such an effect, which is time dependent, would modify the Sr distribution as resulting from the mechanism described above for the upward side

	D_1 (nm)	D_2 (nm)	mismatch with La
Ca-doped	1.89±0.31	2.65±0.34	-2.47%
Sr-doped	0.96±0.33	2.25±0.54	+8.26 %
Ba-doped	1.23±0.26	2.97±0.60	+21.48 %

Table 4.3. Dopant spread at the backward (D_1) and upward (D_2) side of the interface for two-dimensionally doped La_2CuO_4. Cationic size mismatch with La for the three different dopants is reported.

(see Figure 4.49), slightly smearing the profile also at the backward side of the interface.

Chapter 5

Conclusions

The present thesis describes the investigation of interface effects in epitaxial heterostructures with respect to the occurrence of high-temperature superconductivity. In particular, the results have been analyzed in the light of the space-charge model, which predicts a local rearrangement of the mobile charge carriers at the interface as a consequence of a local electrostatic potential. Experiments have been carried out using lanthanum cuprate (La_2CuO_4) as a model material. Since native La_2CuO_4 is an electrical insulator which undergoes a superconducting transition upon p-type doping, strategies have been employed in order to induce space-charge effects with the purpose of enhancing the hole concentration at the interface. The synthesis of the samples has been accomplished by the use of the atomic-layer-by-layer Oxide-Molecular Beam Epitaxy (ALL-Oxide-MBE) method, allowing for controlling the materials composition down to the single atomic layer level.

An important first achievement of the project consisted in the installation and optimization of the Oxide-MBE system. We demonstrated the feasibility of synthesizing single phase lanthanum cuprate and lanthanum nickelate ($La_{2-x}Sr_xNiO_4$), which then have been used as "building blocks" for the heterostructures. Starting from the native material La_2CuO_4, we obtained the superconducting phase by oxygen doping employing in-situ ozone annealing ($La_2CuO_{4+\delta}$) and by doping with an acceptor ($La_{2-x}Sr_xCuO_4$). $La_{2-x}Sr_xNiO_4$ was successfully synthesized, to the best of our knowledge for the first time by Oxide-MBE, exhibiting the typical

insulator-to-metal transition upon x increase.

Two types of heterostructures have been realized for the study of space-charge effects, namely (i) La_2CuO_4 / $La_{2-x}Sr_xNiO_4$ bilayers and superlattices and (ii) two-dimensionally doped La_2CuO_4. In both cases, thanks to local effects of charge redistribution, high-temperature superconductivity occurs with critical temperatures reaching up to $\approx 35 - 40$ K.

In the first case, high-temperature superconductivity is induced in La_2CuO_4 by coupling it with highly doped ($x \geq 0.6$) $La_{2-x}Sr_xNiO_4$. In the light of the compositional analysis performed by STEM, according to which a certain (yet limited to 0.5-1 u.c.) cationic redistribution at the interface occurs, a significant role for the occurrence of high-temperature superconductivity can be attributed to Sr migrating from $La_{2-x}Sr_xNiO_4$ to La_2CuO_4 where it acts as acceptor dopant. Nevertheless, based on further experimental observations (i.e. the intermixing width is strongly dependent on the layers sequence whereas the electrical properties are only partially affected), alternative explanations can be brought to the fore. In particular one can expect the transfer of positively charge carriers, i.e. holes and oxygen vacancies, to the La_2CuO_4 phase inducing a negative potential in $La_{2-x}Sr_xNiO_4$ at the interface. For compensation, holes are enriched in La_2CuO_4 giving rise to the observed high-temperature superconductivity. Although a direct experimental evidence is missing, the findings allow for considering this as a possible explanation.

In the second case (two dimensionally doped La_2CuO_4), the structure consists of superlattices in which, with a predefined periodicity, atomic layers of LaO in La_2CuO_4 are substituted by atomic layers of MO, with M being an acceptor dopant (M=Sr, Ca, Ba). By employing a variety of complementary techniques, several remarkable observations could be made especially in the case of two dimensionally Sr-doped La_2CuO_4 (which was investigated more extensively): (i) electrical transport measurements demonstrated that superconducting layers (whose thickness can be estimated in 2.5-3 u.c.) form in proximity of the SrO layers. T_c is strongly dependent on the spacing between the SrO layers; (ii) by STEM imaging and spectroscopic methods, an asymmetric spread of the dopant, which redistributes mostly in the growth direction, was observed, (iii) the spatially confined dopant

layer acts as a negatively charged surface, inducing the formation of a compensating hole accumulation layer at the side of the interface facing the substrate (where the dopant distribution is abrupt), (iv) at this side of the interface, high-temperature superconductivity is confined to a single atomic layer. In particular the points (iii) and (iv), which were put in evidence by several independent experimental investigations (i.e. zinc-tomography, STEM-EELS, comparison with a related system i.e. La_2CuO_4 /SrO bilayer), undoubtedly demonstrated that the hole and the acceptor dopant distributions are decoupled and that a space-charge mode is active.

The study of two-dimensionally confined Sr-doped La_2CuO_4 allows for a direct comparison between "classical" homogeneous doping and heterogeneous doping based on space-charge effects. We demonstrated that heterogeneous doping, here relying on the intentional introduction of a charged surface in the form of a spatially confined doped region, is effective for inducing high-temperature superconductivity due to hole accumulation. Heterogeneous doping was demonstrated to be not only a successful alternative to homogeneous doping but rather to offer a series of unique features. Thanks to this doping approach, it is possible to affect the charge distribution locally without affecting the material chemical composition and without introducing the crystallographic disorder which instead is intrinsic of homogeneous doping. This has a number of advantages: (i) one can structure the material at wish by inserting active layers in the matrix, defining their number and their position *a-priori*; (ii) the space-charge situation induces layer-dependent defect concentration, allowing for the precise tuning of the functional properties, in contrast to conventional doping which leads to an homogeneous situation. In our case in particular we obtained the alternation of metallic, high-temperature superconducting and insulating phases at the sub-unit-cell level, thus opening a possible path for applications on devices relying on graded, or even asymmetrical, junctions on the sub-nanoscale. Noteworthy, superconductivity is confined to a single atomic plane, whereas a large volume is required in the case of homogeneous doping; (iii) the technique may be applied to situations where the solubility of the dopant is limited and conventional doping is not possible; (iv) our findings

can be used to shed light onto the influence of dimensionality on superconductivity and onto the importance of the effects of defect chemistry and ionic mobility in the field of high-temperature superconductivity.

One further aspect is worth being mentioned: despite the use of ALL-oxide MBE, which is generally acknowledged as the state-of-the-art method for the synthesis of oxide heterostructures, we systematically observed a certain tendency to cationic intermixing at the interfaces. This was true in the case of the $La_{2-x}Sr_xNiO_4$ / La_2CuO_4 interface, in which the intermixing width was about 0.5-1 u.c., but it was particularly evident in the case of two-dimensionally doped La_2CuO_4 in which such a cationic intermixing involved about 3 u.c. This aspect should be taken into serious account in the investigations dealing with oxide epitaxial interfaces, since it may influence, or even determine, the interfacial properties of such systems. The situation is even more complicated by the fact that, in both the cases, we observed that the dopant spread is asymmetric i.e. it is mostly pronounced in the growth direction. We analyzed in particular the case of two-dimensionally doped La_2CuO_4, in which we compared the cationic distribution resulting from the use of different dopants (Sr, Ba, Ca). This allowed us to verify the influence of the ionic radius on the extent of the dopant spread. We could highlight that in the downward direction (opposite to the growth direction) the redistribution is associated with the size of the ionic radius (Ca diffuses more extensively than Ba and Sr), as one would expect in a usual thermal diffusion situation. At the opposite side instead (upward direction), we found no clear trend: having already ruled out that thermal diffusion (which would eventually result in a symmetric dopant profile) occurs at this side, we can also exclude a major role stemming from dopant segregation effects (i.e. dopant migration towards the film surface as a consequence of lattice strain induced by dopant substitution). Rather, redistribution is driven by entropic effects involving the surface layer and the incoming particles during the growth process.

List of symbols and abbreviations

List of most uysed symbols

e	Elementary charge
e'	Electron according to the Kröger-Vink notation
$\mathrm{h}^{\bullet}$	Electron hole according to the Kröger-Vink notation
n	Electron concentration
$\mathrm{O}_{\mathrm{i}}''$	Oxygen interstitial according to the Kröger-Vink notation
P	Pressure
p	Electron hole concentration
R	Electrical resistance
R_{ms}	Root mean squared roughness
T	Temperature
T_{c}	Superconducting critical temperature (10% of the normal state value)
$T_{\mathrm{c,\ 0.9}}$	Superconducting critical temperature (90% of the normal state value)
$\mathrm{Sr}'_{\mathrm{La}}$	Negatively charged Sr dopant on a La site according to the Kröger-Vink notation
$\mathrm{V}_{\mathrm{O}}^{\bullet\bullet}$	Oxygen vacancy according to the Kröger-Vink notation

δ	Oxygen nonstoichiometry
ρ	Electrical resisitivity

List of abbreviations

AFM	Atomic Force Microscopy
ALL	Atomic layer-by-layer
EDXS	Energy-dispersive X-ray spectroscopy
EELS	Electron energy loss spectroscopy
HAADF	High-angle annular dark field
MBE	Molecular Beam Epitaxy
STEM	Scanning transmission electron microscopy
TEM	Transmission electron microscopy
RHEED	Reflection high-energy electron diffraction
XRD	X-ray diffraction
XRR	X-ray reflectivity

Bibliography

[1] J. Maier, "Nanoionics: ion transport and electrochemical storage in confined systems," *Nature Materials*, vol. 4, no. 11, pp. 805–815, 2005.

[2] P. Zubko, S. Gariglio, M. Gabay, P. Ghosez, and J.-M. Triscone, "Interface physics in complex oxide heterostructures," *Annual Review of Condensed Matter Physics*, vol. 2, no. 1, pp. 141–165, 2011.

[3] J. Maier, "Ionic conduction in space charge regions," *Progress in Solid State Chemistry*, vol. 23, no. 3, pp. 171–263, 1995.

[4] J. Maier, "Defect chemistry and conductivity effects in heterogeneous solid electrolytes," *Journal of The Electrochemical Society*, vol. 134, no. 6, pp. 1524–1535, 1987.

[5] P. Lupetin, G. Gregori, and J. Maier, "Mesoscopic charge carriers chemistry in nanocrystalline $SrTiO_3$," *Angewandte Chemie International Edition*, vol. 49, no. 52, pp. 10123–10126, 2010.

[6] K. Urban and C. L. Jia, "Atomic-resolution measurement of oxygen concentration in oxide materials.," *Science*, vol. 303, no. 5666, pp. 2001–4, 2004.

[7] H. J. Avila-Paredes and S. Kim, "The effect of segregated transition metal ions on the grain boundary resistivity of gadolinium doped ceria: Alteration of the space charge potential," *Solid State Ionics*, vol. 177, no. 3536, pp. 3075 – 3080, 2006. Proceedings of the E-MRS Symposium P on Solid State Ionics: Mass and Charge Transport at Various Length Scales.

[8] Y. Chiang, E. B. Lavik, I. Kosacki, H. L. Tuller, and J. Y. Ying, "Defect and transport properties of nanocrystalline CeO_{2-x}," *Applied Physics Letters*, vol. 69, no. 2, pp. 185–187, 1996.

[9] A. Tschöpe and R. Birringer, "Grain size dependence of electrical conductivity in polycrystalline cerium oxide," *Journal of Electroceramics*, vol. 7, no. 3, pp. 169–177, 2001.

[10] S. Kim and J. Maier, "On the conductivity mechanism of nanocrystalline ceria," *Journal of The Electrochemical Society*, vol. 149, no. 10, pp. J73–J83, 2002.

[11] I. Denk, W. Mnch, and J. Maier, "Partial conductivities in $SrTiO_3$: Bulk polarization experiments, oxygen concentration cell measurements, and defect-chemical modeling," *Journal of the American Ceramic Society*, vol. 78, no. 12, pp. 3265–3272, 1995.

[12] K. K. Adepalli, M. Kelsch, R. Merkle, and J. Maier, "Influence of line defects on the electrical properties of single crystal TiO_2," *Advanced Functional Materials*, vol. 23, no. 14, pp. 1798–1806, 2013.

[13] N. Sata, K. Eberman, K. Eberl, and J. Maier, "Mesoscopic fast ion conduction in nanometre-scale planar heterostructures.," *Nature*, vol. 408, no. 6815, pp. 946–9, 2000.

[14] X. Guo, I. Matei, J. Jamnik, J.-S. Lee, and J. Maier, "Defect chemical modeling of mesoscopic ion conduction in nanosized CaF_2/BaF_2 multilayer heterostructures," *Physical Review B*, vol. 76, p. 125429, Sep 2007.

[15] X. Guo and J. Maier, "Ionically conducting two-dimensional heterostructures," *Advanced Materials*, vol. 21, no. 25-26, pp. 2619–2631, 2009.

[16] G. Hammerl, A. Schmehl, R. Schulz, B. Goetz, and H. Bielefeldt, "Enhanced supercurrent density in polycrystalline $YBa_2Cu_3O_{7-\delta}$ at 77 K from calcium doping of grain boundaries," *Nature*, vol. 407, no. 6801, pp. 162–164, 2000.

[17] A. Ohtomo and H. Y. Hwang, "A high-mobility electron gas at the $LaAlO_3/SrTiO_3$ heterointerface," *Nature*, vol. 427, no. 6973, pp. 423–426, 2004.

[18] N. Reyren, S. Thiel, A. D. Caviglia, L. F. Kourkoutis, G. Hammerl, C. Richter, C. W. Schneider, T. Kopp, A.-S. Rüetschi, D. Jaccard, M. Gabay, D. A. Muller, J.-M. Triscone, and J. Mannhart, "Superconducting interfaces between insulating oxides," *Science*, vol. 317, no. 5842, pp. 1196–1199, 2007.

[19] A. Brinkman, M. Huijben, M. van Zalk, J. Huijben, U. Zeitler, J. C. Maan, W. G. van der Wiel, G. Rijnders, D. H. A. Blank, and H. Hilgenkamp, "Magnetic effects at the interface between non-magnetic oxides," *Nature Materials*, vol. 6, no. 7, pp. 493–496, 2007.

[20] N. Nakagawa, H. Y. Hwang, and D. A. Muller, "Why some interfaces cannot be sharp," *Nature Materials*, vol. 5, no. 3, pp. 204–209, 2006.

[21] J. Mannhart and D. G. Schlom, "Oxide interfaces-an opportunity for electronics," *Science*, vol. 327, no. 5973, pp. 1607–11, 2010.

[22] J. N. Eckstein, "Oxide interfaces: Watch out for the lack of oxygen," *Nature Materials*, vol. 6, no. 7, pp. 473–474, 2007.

[23] Z. Q. Liu, C. J. Li, W. M. Lü, X. H. Huang, Z. Huang, S. W. Zeng, X. P. Qiu, L. S. Huang, A. Annadi, J. S. Chen, J. M. D. Coey, T. Venkatesan, and Ariando, "Origin of the two-dimensional electron gas at $LaAlO_3/SrTiO_3$ interfaces: The role of oxygen vacancies and electronic reconstruction," *Physical Review X*, vol. 3, p. 021010, 2013.

[24] L. Qiao, T. C. Droubay, V. Shutthanandan, Z. Zhu, P. V. Sushko, and S. A. Chambers, "Thermodynamic instability at the stoichiometric $LaAlO_3$ / $SrTiO_3$ (001) interface," *Journal of Physics: Condensed Matter*, vol. 22, no. 31, p. 312201, 2010.

[25] M. P. Warusawithana, C. Richter, J. A. Mundy, P. Roy, J. Ludwig, S. Paetel, T. Heeg, A. A. Pawlicki, L. F. Kourkoutis, M. Zheng, M. Lee, B. Mulcahy,

W. Zander, Y. Zhu, J. Schubert, J. N. Eckstein, D. A. Muller, C. S. Hellberg, J. Mannhart, and D. G. Schlom, "$LaAlO_3$ stoichiometry is key to electron liquid formation at $LaAlO_3$-$SrTiO_3$ interfaces," *Nature Communications*, vol. 4, 2013.

[26] A. Ohtomo, D. A. Muller, J. L. Grazul, and H. Y. Hwang, "Artificial charge-modulationin atomic-scale perovskite titanate superlattices," *Nature*, vol. 419, no. 6905, pp. 378–380, 2002.

[27] J. Biscaras, N. Bergeal, A. Kushwaha, T. Wolf, A. Rastogi, R. C. Budhani, and J. Lesueur, "Two-dimensional superconductivity at a mott insulator/band insulator interface $LaTiO_3/SrTiO_3$," *Nature communications*, vol. 1, p. 89, 2010.

[28] K. S. Takahashi, M. Kawasaki, and Y. Tokura, "Interface ferromagnetism in oxide superlattices of $CaMnO_3/CaRuO_3$," *Applied Physics Letters*, vol. 79, no. 9, pp. 1324–1326, 2001.

[29] H. Y. Hwang, Y. Iwasa, M. Kawasaki, B. Keimer, N. Nagaosa, and Y. Tokura, "Emergent phenomena at oxide interfaces," *Nature Materials*, vol. 11, no. 2, pp. 103–113, 2012.

[30] A. Gozar, G. Logvenov, L. F. Kourkoutis, A. T. Bollinger, L. A. Giannuzzi, D. A. Muller, and I. Bozovic, "High-temperature interface superconductivity between metallic and insulating copper oxides," *Nature*, vol. 455, no. 7214, pp. 782–785, 2008.

[31] J. Wu, O. Pelleg, G. Logvenov, A. T. Bollinger, Y.-J. Sun, G. S. Boebinger, M. Vanevic, Z. Radovic, and I. Bozovic, "Anomalous independence of interface superconductivity from carrier density," *Nature Materials*, vol. 12, no. 10, pp. 877–81, 2013.

[32] G. Logvenov, A. Gozar, and I. Bozovic, "High-temperature superconductivity in a single copper-oxygen plane," *Science*, vol. 326, no. 5953, pp. 699–702, 2009.

[33] S. Smadici, J. C. T. Lee, S. Wang, P. Abbamonte, G. Logvenov, A. Gozar, C. D. Cavellin, and I. Bozovic, "Superconducting transition at 38 K in insulating-

overdoped La_2CuO_4-$La_{1.64}Sr_{0.36}CuO_4$ superlattices: Evidence for interface electronic redistribution from resonant soft x-ray scattering," *Physical Review Letters*, vol. 102, no. 10, 2009.

[34] F. Kröger and H. Vink, "Relations between the concentrations of imperfections in crystalline solids," *Solid State Physics*, vol. 3, pp. 307 – 435, 1956.

[35] S. N. Ruddlesden and P. Popper, "The compound $Sr_3Ti_2O_7$ and its structure," *Acta Crystallographica*, vol. 11, no. 1, pp. 54–55, 1958.

[36] D.-K. Seo, W. Liang, M.-H. Whangbo, Z. Zhang, and M. Greenblatt, "Electronic band structure and madelung potential study of the nickelates La_2NiO_4, $La_3Ni_2O_7$, and $La_4Ni_3O_{10}$," *Inorganic Chemistry*, vol. 35, no. 22, pp. 6396–6400, 1996.

[37] J. Longo and P. Raccah, "Structure of La_2CuO_4 and $LaSrVO_4$," *Journal of Solid State Chemistry*, vol. 6, no. 4, pp. 526–531, 1973.

[38] S.-W. Cheong, J. Thompson, and Z. Fisk, "Properties of La_2CuO_4 and related compounds," *Physica C: Superconductivity*, vol. 158, no. 1–2, pp. 109 – 126, 1989.

[39] P. Radaelli, D. Hinks, A. MItchell, B. Hunter, and J. Wagner, "Structural and superconducting properties of $La_{2-x}Sr_xCuO_4$ as a function of sr content," *Physical review. B, Condensed matter*, vol. 49, no. 6, pp. 4163–4175, 1994.

[40] M. Reehuis, C. Ulrich, K. Prokeš, A. Gozar, G. Blumberg, S. Komiya, Y. Ando, P. Pattison, and B. Keimer, "Crystal structure and high-field magnetism of La_2CuO_4," *Physical Review B*, vol. 73, no. 14, p. 144513, 2006.

[41] C. Chaillout, S. Cheong, Z. Fisk, M. Lehmann, M. Marezio, B. Morosin, and J. Schirber, "The crystal structure of superconducting $La_2CuO_{4.032}$ by neutron diffraction," *Physica C*, vol. 158, no. 1-2, pp. 183–191, 1989.

[42] D. Hong and D. Smyth, "Defect chemistry of undoped La_2CuO_4," *Journal of Solid State Chemistry*, vol. 97, no. 2, pp. 427 – 433, 1992.

[43] V. V. Kharton, A. P. Viskup, A. V. Kovalevsky, E. N. Naumovich, and F. M. B. Marques, "Ionic transport in oxygen-hyperstoichiometric phases with K_2NiF_4-type structure," *Solid state ionics*, vol. 143, no. 3-4, pp. 337–353, 2001.

[44] D. Rice and D. Buttrey, "An x-ray diffraction study of the oxygen content phase diagram of $La_2NiO_{4+\delta}$," *Journal of Solid State Chemistry*, vol. 105, no. 1, pp. 197 – 210, 1993.

[45] V. Vashook, S. Tolochko, I. Yushkevich, L. Makhnach, I. Kononyuk, H. Altenburg, J. Hauck, and H. Ullmann, "Oxygen nonstoichiometry and electrical conductivity of the solid solutions $La_{2-x}Sr_xNiO_y$ $(0 \leq x \leq 0.5)$," *Solid State Ionics*, vol. 110, no. 34, pp. 245 – 253, 1998.

[46] H. Kanai, J. Mizusaki, H. Tagawa, S. Hoshiyama, K. Hirano, K. Fujita, M. Tezuka, and T. Hashimoto, "Defect chemistry of $La_{2?x}Sr_xCuO_{4?\delta}$: Oxygen nonstoichiometry and thermodynamic stability," *Journal of Solid State Chemistry*, vol. 131, no. 1, pp. 150 – 159, 1997.

[47] R. Shannon, "Revised effective ionic radii and systematic studies of interatomic distances in halides and chalcogenides," *Acta Crystallographica Section A*, vol. 32, no. 5, pp. 751–767, 1976.

[48] J. Maier and G. Pfundtner, "Defect chemistry of the high-T_c superconductors," *Advanced Materials*, vol. 3, no. 6, pp. 292–297, 1991.

[49] E. J. Opila, H. L. Tuller, B. J. Wuensch, and J. Maier, "Oxygen tracer diffusion in $La_{2-x}Sr_xCuO_{4-y}$ single crystals," *Journal of the American Ceramic Society*, vol. 76, no. 9, pp. 2363–2369, 1993.

[50] J. Maier, *Physical Chemistry of Ionic Materials*, ch. Equilibrium thermodynamics of the real solid, pp. 108–241. John Wiley & Sons, Ltd, 2005.

[51] J. Schirber, B. Morosin, R. Merrill, P. Hlava, E. Venturini, J. Kwak, P. Nigrey, R. Baughman, and D. Ginley, "Stoichiometry of bulk superconducting $La_2CuO_{4+\delta}$: A superconducting superoxide?," *Physica C: Superconductivity*, vol. 152, no. 1, pp. 121 – 123, 1988.

[52] H. Sato, M. Naito, and H. Yamamoto, "Superconducting thin films of $La_2CuO_{4+\delta}$ by oxygen doping using ozone," *Physica. C, Superconductivity*, vol. 280, no. 3, pp. 178–186, 1997.

[53] B. G. Bagley, L. H. Greene, J. Tarascon, and G. W. Hull, "Plasma oxidation of the high-T_c superconducting perovskites," *Applied Physics Letters*, vol. 51, no. 8, pp. 622–624, 1987.

[54] E. Takayama-Muromachi, T. Sasaki, and Y. Matsui, "Direct oxidation of La_2CuO_4 in an aqueous solution of $KMnO_4$," *Physica C: Superconductivity*, vol. 207, no. 1–2, pp. 97 – 101, 1993.

[55] J.-C. Grenier, A. Wattiaux, N. Lagueyte, J. Park, E. Marquestaut, J. Etourneau, and M. Pouchard, "A new superconductor obtained by electrochemical oxidation of La_2CuO_4," *Physica C: Superconductivity*, vol. 173, no. 3–4, pp. 139 – 144, 1991.

[56] H. Takagi, S. ichi Uchida, K. Kitazawa, and S. Tanaka, "High-T_c superconductivity of La-Ba-Cu Oxides. II. -Specification of the superconducting phase," *Japanese Journal of Applied Physics*, vol. 26, no. 2A, p. L123, 1987.

[57] A. R. Moodenbaugh, Y. W. Xu, M. Suenaga, T. J. Folkerts, and R. N. Shelton, "Superconducting properties of $La_{2-x}Ba_xCuO_4$," *Physical Review B*, vol. 38, no. 7, pp. 4596–4600, 1988.

[58] K. Kishio, K. Kitazawa, S. Kanbe, I. Yasuda, N. Sugii, H. Takagi, S. ichi Uchida, K. Fueki, and S. Tanaka, "New high temperature superconducting oxides. $(La_{1-x}Sr_x)_2CuO_{4-\delta}$ and $(La_{1-x}Ca_x)_2CuO_{4-\delta}$," *Chemistry Letters*, vol. 16, no. 2, pp. 429–432, 1987.

[59] N. Nguyen, J. Choisnet, M. Hervieu, and B. Raveau, "Oxygen defect K_2NiF_4-type oxides: The compounds $La_{2-x}Sr_xCuO_{4-x/2+\delta}$," *Journal of Solid State Chemistry*, vol. 39, no. 1, pp. 120 – 127, 1981.

[60] B. Dabrowski, Z. Wang, J. Jorgensen, R. Hitterman, J. Wagner, B. Hunter, and D. Hinks, "Suppression of superconducting transition temperature in orthorhombic $La_{2-x}Ca_xCuO_4$," *Physica C: Superconductivity*, vol. 217, no. 3–4, pp. 455 – 460, 1993.

[61] A. Moodenbaugh, R. Sabatini, YWZu, J. Ochab, and J. Huber, "Solubility of Ca in superconducting $La_{2-x}Ca_xCuO_4$," *Physica. C, Superconductivity*, vol. 198, no. 1-2, pp. 103–108, 1992.

[62] L. Shen, P. Salvador, T. O. Mason, and K. Fueki, "High temperature electrical properties and defect chemistry of $La_{2-x}Ca_xCuO_{4-y}$ superconductors-II. Defect structure modeling," *Journal of Physics and Chemistry of Solids*, vol. 57, no. 12, pp. 1977–1987, 1996.

[63] H. Sato, A. Tsukada, M. Naito, and A. Matsuda, "$La_{2-x}Sr_xCuO_y$ epitaxial thin films (x=0 to 2): Structure, strain, and superconductivity," *Physical Review B*, vol. 61, no. 18, pp. 12447–12456, 2000.

[64] M.-Y. Su, E. A. Cooper, C. E. Elsbernd, and T. O. Mason, "High-temperature defect structure of lanthanum cuprate," *Journal of the American Ceramic Society*, vol. 73, no. 11, pp. 3453–3456, 1990.

[65] Y. Wu, D. E. Ellis, L. Shen, and T. O. Mason, "Point defects of La_2CuO_4-based ceramics, part I: Oxygen interstitials," *Journal of the American Ceramic Society*, vol. 79, no. 6, pp. 1599–1604, 1996.

[66] J. B. Torrance, Y. Tokura, A. I. Nazzal, A. Bezinge, T. C. Huang, and S. S. P. Parkin, "Anomalous disappearance of high-T_c superconductivity at high hole concentration in metallic $La_{2-x}Sr_xCuO_4$," *Physical Review Letters*, vol. 61, no. 9, pp. 1127–1130, 1988.

[67] L. Shen, P. A. Salvador, and T. O. Mason, "Point defect modeling of La_2CuO_4-based superconductors," *Journal of the American Ceramic Society*, vol. 77, no. 1, pp. 81–88, 1994.

[68] J. D. Jorgensen, B. Dabrowski, S. Pei, D. G. Hinks, L. Soderholm, B. Morosin, J. E. Schirber, E. L. Venturini, and D. S. Ginley, "Superconducting phase of $La_2CuO_{4+\delta}$: A superconducting composition resulting from phase separation," *Physical Review B*, vol. 38, pp. 11337–11345, 1988.

[69] V. Y. Butko, G. Logvenov, N. Bozovic, Z. Radovic, Z., and I. Bozovic, "Madelung strain in cuprate superconductors: A route to enhancement of the critical temperature," *Advanced Materials*, vol. 21, no. 36, pp. 3644–3648, 2009.

[70] J. Bednorz and K. Müller, "Possible high-T_c superconductivity in the BaLaCuO system," *Zeitschrift für Physik B Condensed Matter*, vol. 64, no. 2, pp. 189–193, 1986.

[71] A. Schilling, M. Schilling, J. D. Cantoni, H. R. Guo, and Ott, "Superconductivity above 130-K in the Hg-Ba-Ca-Cu-O system," *Nature*, vol. 363, no. 6424, pp. 56–58, 1993.

[72] C. Chu, L. Gao, F. Chen, Z. huang, and R. Meng, "Superconductivity above 150-K in $HgBa_2Ca_2Cu_3O_{8+\delta}$ at high-pressures," *Nature*, vol. 365, no. 6444, pp. 323–325, 1993.

[73] T. Yamada, K. Kinoshita, and H. Shibata, "Synthesis of superconducting T'-$(La_{1-x}Ce_x)_2CuO_4$," *Japanese Journal of Applied Physics*, vol. 33, no. 2A, p. L168, 1994.

[74] M. Naito and M. Hepp, "Superconducting T-$La_{2-x}Ce_xCuO_4$ films grown by molecular beam epitaxy," *Japanese Journal of Applied Physics*, vol. 39, no. 6A, p. L485, 2000.

[75] A. Sawa, M. Kawasaki, H. Takagi, and Y. Tokura, "Electron-doped superconductor$La_{2-x}Ce_xCuO_4$: Preparation of thin films and modified doping range for superconductivity," *Physical Review B*, vol. 66, p. 014531, 2002.

[76] Y. Kamihara, T. Watanabe, M. Hirano, and H. Hosono, "Iron-based layered superconductor $La[O_1 - xF_x]FeAs$ (x = 0.05 − 0.12) with T_c = 26 K," *Journal of the American Chemical Society*, vol. 130, no. 11, pp. 3296–3297, 2008.

[77] J. Bardeen, L. N. Cooper, and J. R. Schrieffer, "Theory of superconductivity," *Physical Review*, vol. 108, pp. 1175–1204, 1957.

[78] N. E. Hussey, "Phenomenology of the normal state in-plane transport properties of high-T_c cuprates," *Journal of Physics: Condensed Matter*, vol. 20, no. 12, p. 123201, 2008.

[79] C. Varma, "High-temperature superconductivity: Mind the pseudogap," *Nature*, vol. 468, no. 7321, pp. 184–5, 2010.

[80] Y. Ando, S. Komiya, K. Segawa, S. Ono, and Y. Kurita, "Electronic phase diagram of high-T_c cuprate superconductors from a mapping of the in-plane resistivity curvature," *Physical Review Letters.*, vol. 93, p. 267001, 2004.

[81] H. Sato, A. Tsukada, M. Naito, and A. Matsuda, "Absence of 1/8 anomaly in strained thin films of $La_{2-x}Ba_xCuO_{4+\delta}$," *Physical Review B*, vol. 62, no. 2, pp. R799–R802, 2000.

[82] I. Bozovic, G. Logvenov, I. Belca, B. Narimbetov, and I. Sveklo, "Epitaxial strain and superconductivity in $La_{2-x}Sr_xCuO_4$ thin films," *Physical Review Letters*, vol. 89, no. 10, p. 107001, 2002.

[83] M. Khan, Y. Mori, I. Tanaka, and H. Kojima, "Growth and superconductivity of $La_{2x}Ca_xCuO_4$ single crystals," *Physica C: Superconductivity*, vol. 262, no. 3–4, pp. 202 – 206, 1996.

[84] M. Fukuoka, Y. Nakayama, Y. Tomioka, K. Kishio, and K. Kitazawa, "Superconductivity of $(La,Ca)_2CuO_4$ prepared in high oxygen pressure," *Physica C: Superconductivity*, vol. 190, no. 1–2, pp. 91 – 92, 1991. Proceedings of the International Workshop on Chemical Designing and Processing of High-T_c Superconductors (Chem-HTSC).

[85] L. Liu, G. Che, J. Zhao, and Z. Zhao, "Thermal treatment effect of the oxidized $La_2CuO_{4+\delta}$: The access of continuous and discontinuous T_c," *Physica C: Superconductivity*, vol. 425, no. 1–2, pp. 37 – 43, 2005.

[86] P. G. Radaelli, J. D. Jorgensen, R. Kleb, B. A. Hunter, F. C. Chou, and D. C. Johnston, "Miscibility gap in electrochemically oxygenated $La_2CuO_{4+\delta}$," *Physical Review B*, vol. 49, pp. 6239–6245, Mar 1994.

[87] H. H. Feng, Z. G. Li, P. H. Hor, S. Bhavaraju, J. F. DiCarlo, and A. J. Jacobson, "Superconducting phases of $La_2CuO_{4+\delta}$ prepared by electrochemical oxidation at ambient temperature," *Physical Review B*, vol. 51, pp. 16499–16502, Jun 1995.

[88] P.-H. Hor, H.-H. Feng, Z.-G. Li, J. F. Dicarlo, S. Bhavaraju, and A. J. Jacobson, "Phase separations and superconductivity in electrochemically intercalated $La_2CuO_{4+\delta}$," *Journal of Physics and Chemistry of Solids*, vol. 57, no. 6–8, pp. 1061 – 1065, 1996. Proceeding of the 8th International Symposium on Intercalation Compounds.

[89] B. O. Wells, Y. S. Lee, M. A. Kastner, R. J. Christianson, R. J. Birgeneau, K. Yamada, Y. Endoh, and G. Shirane, "Incommensurate spin fluctuations in high-transition temperature superconductors," *Science*, vol. 277, no. 5329, pp. 1067–1071, 1997.

[90] L. Chen, C. Dong, Y. Huang, F. Zhou, G. Che, and Z. Zhao, "Superconducting phase with T_c of 17 K in $La_2CuO_{4+\delta}$," *Solid State Communications*, vol. 114, no. 2, pp. 107 – 111, 2000.

[91] N. Poccia, M. Fratini, A. Ricci, G. Campi, L. Barba, A. V. Orgeas, G. Bianconi, G. Aeppli, and A. Bianconi, "Evolution and control of oxygen order in a cuprate superconductor.," *Nature Materials*, vol. 10, no. 10, pp. 733–6, 2011.

[92] M. Schroeder and M. A. Dragan, "Oxygen transport in $La_{2-x}Sr_xNiO_{4+\delta}$: membrane permeation and defect chemical modelling," *Journal of Material Science*, vol. 42, no. 6, pp. 1972–1983, 2007. International Conference on Nonstoichiometric Compounds, Kauai, HI, APR 03-08, 2005.

[93] Nakamura, "Oxygen nonstoichiometry and defect equilibrium in la2xsrxnio4," *Solid state ionics*, vol. 180, no. 4-5, p. 368, 2009.

[94] Kim, "Defect- chemical analysis of the nonstoichiometry, conductivity and thermopower of La_2NiO_4," *PCCP. Physical chemistry chemical physics*, vol. 12, no. 18, p. 4704, 2010.

[95] Vashook, "Composition and conductivity of some nickelates," *Solid state ionics*, vol. 119, no. 1-4, p. 23, 1999.

[96] E. Naumovich, M. Patrakeev, V. Kharton, A. Yaremchenko, D. Logvinovich, and F. Marques, "Oxygen nonstoichiometry in $La_2Ni(M)O_{4+\delta}$ (M=Cu, Co) under oxidizing conditions," *Solid State Sciences*, vol. 7, no. 11, pp. 1353 – 1362, 2005.

[97] Z. Li, R. Haugsrud, J. Smith, and T. Norby, "Steady-state permeation of oxygen through $La_{1.9}Sr_{0.1}NiO_{4+\delta}$," *Journal of the Electrochemical Society*, vol. 156, no. 9, pp. B1039–B1044, 2009.

[98] J. P. Tang, R. I. Dass, and A. Manthiram, "Comparison of the crystal chemistry and electrical properties of $La_{2x}A_xNiO_4$ (A = Ca, Sr, and Ba)," *Materials Research Bulletin*, vol. 35, no. 3, pp. 411–424, 2000.

[99] M. Hücker, K. Chung, M. Chand, T. Vogt, J. M. Tranquada, and D. J. Buttrey, "Oxygen and strontium codoping of La_2NiO_4: Room-temperature phase diagrams," *Physical Review B*, vol. 70, p. 064105, Aug 2004.

[100] J. Bassat, P. Odier, A. Villesuzanne, C. Marin, and M. Pouchard, "Anisotropic ionic transport properties in $La_2NiO_{4+\delta}$ single crystals," *Solid State Ionics*, vol. 167, no. 34, pp. 341 – 347, 2004.

[101] K. Sreedhar and J. Honig, "Low-temperature electron transport properties of $La_{2-x}Sr_xNiO_4$ with $0.5 \leq x \leq 1.3$," *Journal of Solid State Chemistry*, vol. 111, no. 1, pp. 147 – 150, 1994.

[102] S. Shinomori, M. Kawasaki, and Y. Tokura, "Orientation-controlled epitaxy and anisotropic properties of $La_{2-x}Sr_xNiO_4$ with $0.5 \leq x \leq 1.5$ covering the insulator–metal transition," *Applied Physics Letters*, vol. 80, no. 4, pp. 574–576, 2002.

[103] K. Ruck, G. Krabbes, and I. Vogel, "Structural and electrical properties of $La_{2-x}Ca_xNiO_{4+\delta}$ ($0 \leq x \leq 0.4$) with regard to the oxygen content δ," *Materials Research Bulletin*, vol. 34, no. 10–11, pp. 1689–1697, 1999.

[104] J. Alonso, J. Amador, E. Gutirrez-Puebla, M. Monge, I. Rasines, C. Ruz-Valero, and J. Camp, "Persistence of the La_2NiO_4 crystal structure in$La_{2-x}Ba_xNiO_4$ samples with high *ba* contents ($x \leq 1$)," *Solid State Communications*, vol. 76, no. 12, pp. 1327 – 1331, 1990.

[105] R. A. De Souza and M. Martin, "Using $^{18}O/^{16}O$ exchange to probe an equilibrium space-charge layer at the surface of a crystalline oxide: method and application," *Phys. Chem. Chem. Phys.*, vol. 10, pp. 2356–2367, 2008.

[106] Z. Wang, M. Saito, K. McKenna, L. Gu, S. Tsukimoto, A. Shluger, and Y. Ikuhara, "Atom-resolved imaging of ordered defect superstructures at individual grain boundaries.," *Nature*, vol. 479, no. 7373, pp. 380–3, 2011.

[107] S. Kim, J. Fleig, and J. Maier, "Space charge conduction: Simple analytical solutions for ionic and mixed conductors and application to nanocrystalline ceria," *Phys. Chem. Chem. Phys.*, vol. 5, pp. 2268–2273, 2003.

[108] H. L. Tuller, S. J. Litzelman, and W. Jung, "Micro-ionics: next generation power sources," *Physical Chemistry Chemical Physics*, vol. 11, no. 17, pp. 3023–3034, 2009.

[109] J. Maier, "Defect chemistry and ion transport in nanostructured materials: Part ii. aspects of nanoionics," *Solid State Ionics*, vol. 157, no. 1–4, pp. 327 – 334, 2003. Proceedings of the 6th International Symposium on Systems with Fast Ionic Transport (ISSFIT).

[110] J. Maier, "Ionic transport in nano-sized systems," *Solid State Ionics*, vol. 175, no. 1–4, pp. 7 – 12, 2004. Fourteenth International Conference on Solid State Ionics.

[111] M. C. Göbel, G. Gregori, and J. Maier, "Numerical calculations of space charge layer effects in nanocrystalline ceria. part I: comparison with the analytical

models and derivation of improved analytical solutions," *Physical Chemistry Chemical Physics*, vol. 16, pp. 10214–10231, 2014.

[112] M. Ohring, *Materials Science of Thin Films*. Academic Press, 2002.

[113] J. A. Venables, G. D. T. Spiller, and M. Hanbucken, "Nucleation and growth of thin films," *Reports on Progress in Physics*, vol. 47, no. 4, p. 399, 1984.

[114] K. Reichelt, "Nucleation and growth of thin films," *Vacuum*, vol. 38, no. 12, pp. 1083 – 1099, 1988.

[115] D. L. Smith, *Thin-film deposition: principles and practice*. McGraw-Hill, Inc, 1995.

[116] D. G. Schlom, J. N. Eckstein, I. Bozovic, Z. J. Chen, A. F. Marshall, K. E. von Dessonneck, and J. Harris, J. S., "Molecular beam epitaxy-a path to novel high-T_c superconductors?," *Proceedings of the SPIE - The International Society for Optical Engineering*, vol. 1285, pp. 234–47, 1990.

[117] D. G. Schlom, *Molecular beam epitaxial growth of cuprate superconductors and related phases*. PhD thesis, Stanford University, 1990.

[118] J. N. Eckstein and I. Bozovic, "High-temperature superconducting multilayers and heterostructures grown by atomic layer-by-layer molecular beam epitaxy," *Annual Review of Materials Science*, vol. 25, no. 1, pp. 679–709, 1995.

[119] M. I. Nandasiri, P. Nachimuthu, T. Varga, V. Shutthanandan, W. Jiang, S. V. N. T. Kuchibhatla, S. Thevuthasan, S. Seal, and A. Kayani, "Influence of growth rate on the epitaxial orientation and crystalline quality of CeO_2 thin films grown on $Al_2O_3(0001)$," *Journal of Applied Physics*, vol. 109, no. 1, pp. –, 2011.

[120] T. Venkatesan, E. W. Chase, X. D. Wu, A. Inam, C. C. Chang, and F. K. Shokoohi, "Superconducting $Y_1Ba_2Cu_3O_{7-x}$ films on si," *Applied Physics Letters*, vol. 53, no. 3, pp. 243–245, 1988.

[121] D. G. Schlom, J. N. Eckstein, E. S. Hellman, S. K. Streiffer, J. S. Harris, M. R. Beasley, J. C. Bravman, T. H. Geballe, C. Webb, K. E. von Dessonneck, and F. Turner, "Molecular beam epitaxy of layered DBCO compounds," *Applied Physics Letters*, vol. 53, no. 17, pp. 1660–1662, 1988.

[122] M. A. H. H. Sitter, *Molecular Beam Epitaxy" Fundamentals and current status*. Springer-Verlag, 1989.

[123] J. N. Eckstein, I. Bozovic, K. E. von Dessonneck, D. G. Schlom, J. S. Harris, and S. M. Baumann, "Atomically layered heteroepitaxial growth of single-crystal films of superconducting $Bi_2Sr_2Ca_2Cu_3O_x$," *Applied Physics Letters*, vol. 57, no. 9, pp. 931–933, 1990.

[124] I. Bozovic, J. Eckstein, M. Klausmeier-Brown, and G. Virshup, "Superconductivity in epitaxial $Bi_2Sr_2CuO_6/Bi_2Sr_2CaCu_2O_8$ superlattices: The superconducting behavior of ultrathin cuprate slabs," *Journal of Superconductivity*, vol. 5, no. 1, pp. 19–23, 1992.

[125] F. Baiutti, G. Christiani, and G. Logvenov, "Towards precise defect control in layered oxide structures by using oxide molecular beam epitaxy," *Beilstein Journal of Nanotechnology*, vol. 5, pp. 596–602, 2014.

[126] I. Bozovic, "Atomic-layer engineering of superconducting oxides: yesterday, today, tomorrow," *Applied Superconductivity, IEEE Transactions on*, vol. 11, pp. 2686–2695, Mar 2001.

[127] B. Cullity and S. Stock, *Elements of X-ray diffraction*. Prentice Hall, 2001.

[128] A. Le Bail, I. Madsen, L. M. D. Cranswick, J. K. Cockcroft, P. Norby, A. D. Zuev, A. Fitch, J. Rodriguez-Carvajal, C. Giacovazzo, R. B. Von Dreele, P. Scardi, N. C. Popa, R. Allmann, L. A. Solovyov, B. Hinrichsen, U. Schwarz, A. Altomare, A. Moliterni, R. Caliandro, R. Rizzi, N. V. Y. Scarlett, and M. Jansen, *Powder Diffraction*. The Royal Society of Chemistry, 2008.

[129] M. Lagally and D. Savage, "Quantitative electron diffraction from thin films," *MRS Bulletin*, vol. 18, pp. 24–31, 1 1993.

[130] N. J. C. Ingle, A. Yuskauskas, R. Wicks, M. Paul, and S. Leung, "The structural analysis possibilities of reflection high energy electron diffraction," *Journal of Physics D: Applied Physics*, vol. 43, no. 13, p. 133001, 2010.

[131] J. E. Mahan, K. M. Geib, G. Y. Robinson, and R. G. Long, "A review of the geometrical fundamentals of reflection highenergy electron diffraction with application to silicon surfaces," *Journal of Vacuum Science & Technology A*, vol. 8, no. 5, pp. 3692–3700, 1990.

[132] O. Auciello and A. R. Krauss, "In situ real-time characterization of thin films," *Measurement Science and Technology*, vol. 13, no. 4, p. 644, 2002.

[133] J. B. Nelson and D. P. Riley, "An experimental investigation of extrapolation methods in the derivation of accurate unit-cell dimensions of crystals," *Proceedings of the Physical Society*, vol. 57, no. 3, p. 160, 1945.

[134] E. E. Fullerton, I. K. Schuller, H. Vanderstraeten, and Y. Bruynseraede, "Structural refinement of superlattices from x-ray diffraction," *Physical Review B*, vol. 45, pp. 9292–9310, Apr 1992.

[135] U. Pietsch, V. Holy, and T. Baumbach, *High-resolution X-ray scattering: from thin films to lateral nanostructures*. Sp, 2004.

[136] J. Als-Nielsen and D. McMorrow, *Elements of Modern X-ray Physics, 2nd Edition*. Wiley, 2011.

[137] L. G. Parratt, "Surface studies of solids by total reflection of x-rays," *Physical Review*, vol. 95, pp. 359–369, Jul 1954.

[138] G. Binnig, C. F. Quate, and C. Gerber, "Atomic force microscope," *Physical Review Letters.*, vol. 56, pp. 930–933, Mar 1986.

[139] L. van der Pauw, "A method of measuring specific resistivity and hall effect of lamellae of arbitrary shap," *Philips Technical review*, vol. 20, pp. 220–224, 1958.

[140] F. Baiutti, G. Logvenov, G. Gregori, G. Christiani, Y. Wang, W. Sigle, P. A. van Aken, and J. Maier, "High-temperature superconductivity in space-charge regions of lanthanum cuprate induced by two-dimensional doping," *Nature Communications*, 2015. Submitted.

[141] P. Hartel, H. Rose, and C. Dinges, "Conditions and reasons for incoherent imaging in stem," *Ultramicroscopy*, vol. 63, no. 2, pp. 93 – 114, 1996.

[142] S. J. Pennycook, M. Varela, A. R. Lupini, M. P. Oxley, and M. F. Chisholm, "Atomic-resolution spectroscopic imaging: past, present and future," *Journal of Electron Microscopy*, vol. 58, no. 3, pp. 87–97, 2009.

[143] H. Romberg, M. Alexander, N. Nucker, P. Adelmann, and J. Fink, "Electronic structure of the system," *Physical Review B*, vol. 42, pp. 8768–8771, Nov 1990.

[144] D. A. Muller, N. Nakagawa, A. Ohtomo, J. L. Grazul, and H. Y. Hwang, "Atomic-scale imaging of nanoengineered oxygen vacancy profiles in $SrTiO_3$," *Nature*, vol. 430, no. 7000, pp. 657–661, 2004. 10.1038/nature02756.

[145] D. B. Williams and C. B. Carter, *Transmission Electron Microscopy - A Textbook for Material Science*. Springer, 2009.

[146] J. He, R. F. Klie, G. Logvenov, I. Bozovic, and Y. Zhu, "Microstructure and possible strain relaxation mechanisms of $La_2CuO_{4+\delta}$ thin films grown on $LaSrAlO_4$ and $SrTiO_3$ substrates," *Journal of Applied Physics*, vol. 101, no. 7, pp. 073906–6, 2007.

[147] G. Logvenov and I. Bozovic, "Artificial superlattices grown by MBE: Could we design novel superconductors?," *Physica C: Superconductivity*, vol. 468, no. 2, pp. 100 – 104, 2008. Room Temperature Superconductivity.

[148] D. G. Schlom, L.-Q. Chen, X. Pan, A. Schmehl, and M. A. Zurbuchen, "A thin film approach to engineering functionality into oxides," *Journal of the American Ceramic Society*, vol. 91, no. 8, pp. 2429–2454, 2008.

[149] J. Locquet, J. Perret, J. Fompeyrine, E. Machler, and J. Seo, "Doubling the critical temperature of $La_{1.9}Sr_{0.1}CuO_4$ using epitaxial strain," *Nature*, vol. 394, no. 6692, pp. 453–456, 1998.

[150] M. Minola, F. Baiutti, G. Cristiani, G. Logvenov, M. Le Tacon, B. Keimer, M. Salluzzo, G. Dellea, G. Ghiringhelli, and L. Braicovich, "Spin excitations in ultrathin optimally doped high-T_c cuprates," 2015. In preparation.

[151] H. Sato, H. Yamamoto, and M. Naito, "Growth of (001) $La_{1.85}Sr_{0.15}CuO_4$ ultrathin films without buffer or cap layers," *Physica C: Superconductivity*, vol. 274, no. 34, pp. 227 – 231, 1997.

[152] A. Rufenacht, P. Chappatte, S. Gariglio, C. Leemann, J. Fompeyrine, J.-P. Locquet, and P. Martinoli, "Growth of single unit-cell superconducting $La_{2-x}Sr_xCuO_4$ films," *Solid-State Electronics*, vol. 47, no. 12, pp. 2167 – 2170, 2003. Proceedings of the 9th International Workshop on Oxide Electronics.

[153] V. Faucheux, S. Pignard, and M. Audier, "Growth of La_2NiO_4 thin films by chemical vapor deposition," *Journal of Crystal Growth*, vol. 275, no. 1-2, pp. E947–E951, 2005.

[154] G. Garcia, M. Burriel, N. Bonanos, and J. Santiso, "Electrical conductivity and oxygen exchange kinetics of $La_2NiO_{4+\delta}$ thin films grown by chemical vapor deposition," *Journal of Electrochemical Society*, vol. 155, no. 3, pp. P28–P32, 2008.

[155] P. Briois, F. Perry, and A. Billard, "Structural and electrical characterisation of lanthanum nickelate reactively sputter-deposited thin films," *Thin solid films*, vol. 516, no. 10, pp. 3282–3286, 2008.

[156] S. Shinomori, Y. Okimoto, M. Kawasaki, and Y. Tokura, "Insulator-metal transition in $La_{2-x}Sr_xNiO_4$," *Journal of the Physical Society of Japan*, vol. 71, no. 3, pp. 705–708, 2002.

[157] G. Kim, S. Wang, A. J. Jacobson, and C. L. Chen, "Measurement of oxygen transport kinetics in epitaxial $La_2NiO_{4+\delta}$ thin films by electrical conductivity relaxation," *Solid State Ionics*, vol. 177, no. 17-18, pp. 1461–1467, 2006.

[158] D. Lee, A. Grimaud, E. Crumlin, K. Mezghani, and M. Habib, "Strain influence on the oxygen electrocatalysis of the (100)-oriented epitaxial $La_2NiO_{4+\delta}$ thin films at elevated temperatures," *The journal of physical chemistry. C*, vol. 117, no. 37, pp. 18789–18795, 2013.

[159] S. Smadici, J. C. T. Lee, J. Morales, G. Logvenov, O. Pelleg, I. Bozovic, Y. Zhu, and P. Abbamonte, "Graded orbital occupation near interfaces in a La_2CuO_4 / La_2NiO_4 superlattice," *Physical Review B*, vol. 84, no. 15, p. 155411, 2011. PRB.

[160] Y. Hotta, T. Susaki, and H. Y. Hwang, "Polar discontinuity doping of the $LaVO_3/SrTiO_3$ interface," *Physical Review Letters.*, vol. 99, p. 236805, Dec 2007.

[161] A. Bhattacharya, S. J. May, S. G. E. te Velthuis, M. Warusawithana, X. Zhai, B. Jiang, J. M. Zuo, M. R. Fitzsimmons, S. D. Bader, and J. N. Eckstein, "Metal-insulator transition and its relation to magnetic structure in $LaMnO_{32n}$ / $SrMnO_{3n}$," *Physical Review Letters*, vol. 100, no. 25, p. 257203, 2008. PRL.

[162] P. Perna, D. Maccariello, M. Radovic, U. Scotti di Uccio, I. Pallecchi, M. Codda, D. Marr, C. Cantoni, J. Gazquez, M. Varela, S. J. Pennycook, and F. M. Granozio, "Conducting interfaces between band insulating oxides: The $LaGaO_3/SrTiO_3$ heterostructure," *Applied Physics Letters*, vol. 97, no. 15, pp. –, 2010.

[163] C. He, T. D. Sanders, M. T. Gray, F. J. Wong, V. V. Mehta, and Y. Suzuki, "Metal-insulator transitions in epitaxial $LaVO_3$ and $LaTiO_3$ films," *Physical Review B*, vol. 86, p. 081401, 2012.

[164] C. Li, L. Gu, X. Guo, D. Samuelis, K. Tang, and J. Maier, "Charge carrier accumulation in lithium fluoride thin films due to Li-Ion absorption by titania (100) subsurface," *Nano Letters*, vol. 12, no. 3, pp. 1241–1246, 2012.

[165] F. Zheng, G. Logvenov, I. Bozovic, Y. Zhu, and J. He, "Structural origin of enhanced critical temperature in ultrafine multilayers of cuprate superconducting films," *Phys. Rev. B*, vol. 89, p. 184509, May 2014.

[166] P. R. Willmott, S. A. Pauli, R. Herger, C. M. Schlepütz, D. Martoccia, B. D. Patterson, B. Delley, R. Clarke, D. Kumah, C. Cionca, and Y. Yacoby, "Structural basis for the conducting interface between $LaAlO_3$ and $SrTiO_3$," *Physical Review Letters*, vol. 99, no. 15, p. 155502, 2007. PRL.

[167] S. A. Chambers, M. H. Engelhard, V. Shutthanandan, Z. Zhu, T. C. Droubay, L. Qiao, P. V. Sushko, T. Feng, H. D. Lee, T. Gustafsson, E. Garfunkel, A. B. Shah, J. M. Zuo, and Q. M. Ramasse, "Instability, intermixing and electronic structure at the epitaxial heterojunction," *Surface Science Reports*, vol. 65, no. 10–12, pp. 317–352, 2010.

[168] H. K. Sato, C. Bell, Y. Hikita, and H. Y. Hwang, "Stoichiometry control of the electronic properties of the $LaAlO_3/SrTiO_3$ heterointerface," *Applied Physics Letters*, vol. 102, no. 25, pp. –, 2013.

[169] R. Colby, L. Qiao, K. H. L. Zhang, V. Shutthanandan, J. Ciston, B. Kabius, and S. A. Chambers, "Cation intermixing and electronic deviations at the insulating $LaCrO_3/SrTiO_3(001)$ interface," *Physical Review B*, vol. 88, p. 155325, 2013.

[170] S. Nazir, B. Amin, U. Schwingenschloegl, and U. Schwingenschlgl, "Suppression of the two-dimensional electron gas in $LaGaO_3/SrTiO_3$ by cation intermixing.," *Scientific Reports*, vol. 3, p. 3409, 2013.

[171] L. F. Kourkoutis, D. A. Muller, Y. Hotta, and H. Y. Hwang, "Asymmetric interface profiles in $LaVO_3/SrTiO_3$ heterostructures grown by pulsed laser deposition," *Applied Physics Letters*, vol. 91, no. 16, pp. –, 2007.

[172] S. J. May, A. B. Shah, S. G. E. te Velthuis, M. R. Fitzsimmons, J. M. Zuo, X. Zhai, J. N. Eckstein, S. D. Bader, and A. Bhattacharya, "Magnetically asymmetric interfaces in a $LaMnO_3/SrMnO_3$ superlattice due to structural asymmetries," *Physical Review B*, vol. 77, p. 174409, 2008.

[173] T. Nakano, N. Momono, T. Nagata, M. Oda, and M. Ido, "Contrasting Ni- and Zn-substitution effects on magnetic properties and superconductivity in $La_{2-x}Sr_xCuO_4$," *Physical Review B*, vol. 58, pp. 5831–5838, Sep 1998.

[174] D. Haskel, E. A. Stern, V. Polinger, and F. Dogan, "Suppression of superconductivity in $La_{1.85}Sr_{0.15}Cu_{1-y}Ni_yO_4$: The relevance of local lattice distortions," *AIP Conference Proceedings*, vol. 554, no. 1, pp. 154–168, 2001.

[175] A. Kan, H. Ogawa, H. Ohsato, and J. Sugishita, "Influence of M (M =Zn and Ni) substitution for Cu on microwave dielectric characteristics of $YBa_2(Cu_{1-x}M_x)O_5$ solid solutions," *Japanese Journal of Applied Physics*, vol. 40, no. 9S, p. 5774, 2001.

[176] M. Kilo, M. A. Taylor, C. Argirusis, G. Borchardt, B. Lesage, S. Weber, S. Scherrer, H. Scherrer, M. Schroeder, and M. Martin, "Cation self-diffusion of ^{44}Ca,^{88}Y, and ^{96}Zr in single-crystalline calcia- and yttria-doped zirconia," *Journal of Applied Physics*, vol. 94, no. 12, pp. 7547–7552, 2003.

[177] M. Taylor, C. Argirusis, M. Kilo, G. Borchardt, K.-D. Luther, and W. Assmus, "Correlation between ionic radius and cation diffusion in stabilised zirconia," *Solid State Ionics*, vol. 173, no. 1–4, pp. 51 – 56, 2004. Proceedings of {EMRS} Symposium K on Solid State Ionics: High Temperature vs. Low Temperature Defect Chemistry.

[178] E. F. Schubert, J. B. Stark, B. Ullrich, and J. E. Cunningham, "Spatial localization of impurities in Delta-doped n-type GaAs," *Applied Physics Letters*, vol. 52, no. 18, pp. 1508–1510, 1988.

[179] B. Jalan, S. Stemmer, S. Mack, and S. J. Allen, "Two-dimensional electron gas in δ-doped $SrTiO_3$," *Physical Review B*, vol. 82, no. 8, p. 081103, 2010. PRB.

[180] Y. Kozuka, M. Kim, H. Ohta, Y. Hikita, C. Bell, and H. Y. Hwang, "Enhancing the electron mobility via delta-doping in $SrTiO_3$," *Applied Physics Letters*, vol. 97, no. 22, pp. –, 2010.

[181] K. Nishio, M. Matvejeff, R. Takahashi, M. Lippmaa, M. Sumiya, H. Yoshikawa, K. Kobayashi, and Y. Yamashita, "Delta-doped epitaxial La:$SrTiO_3$ field-effect transistor," *Applied Physics Letters*, vol. 98, no. 24, pp. –, 2011.

[182] D. Ouellette, P. Moetakef, T. Cain, J. Zhang, S. Stemmer, D. Emin, and S. J. Allen, "High-density two-dimensional small polaron gas in a delta-doped mott insulator.," *Scientific Reports*, vol. 3, p. 3284, 2013.

[183] T. S. Santos, B. J. Kirby, S. Kumar, S. J. May, J. A. Borchers, B. B. Maranville, J. Zarestky, S. G. E. te Velthuis, J. van den Brink, and A. Bhattacharya, "Delta doping of ferromagnetism in antiferromagnetic manganite superlattices," *Physical Review Letters*, vol. 107, no. 16, p. 167202, 2011. PRL.

[184] I. Bozovic, G. Logvenov, M. Verhoeven, P. Caputo, E. Goldobin, and T. H. Geballe, "No mixing of superconductivity and antiferromagnetism in a high-temperature superconductor.," *Nature*, vol. 422, no. 6934, pp. 873–5, 2003.

[185] Y. Kozuka, M. Kim, C. Bell, B. G. Kim, Y. Hikita, and H. Y. Hwang, "Two-dimensional normal-state quantum oscillations in a superconducting heterostructure," *Nature*, vol. 462, no. 7272, pp. 487–490, 2009.

[186] B. E. Conway, C. G. Vayenas, R. E. White, and M. E. Gamboa-Adelco, *J. Maier in Modern Aspects of Electrochemistry 38*. Springer US, 2005.

[187] I. Bozovic and J. N. Eckstein, "Analysis of growing films of complex oxides by rheed," *Mrs Bulletin*, vol. 20, no. 5, pp. 32–38, 1995. Bozovic, i eckstein, jn.

[188] H. Alloul, P. Mendels, H. Casalta, J. Marucco, and J. Arabski, "Correlations between magnetic and superconducting properties of Zn-substituted $YBa_2Ca_3O_{6+X}$," *Physical review letters*, vol. 67, no. 22, pp. 3140–3143, 1991.

[189] K. Karpinska, M. Z. Cieplak, S. Guha, A. Malinowski, T. Skoskiewicz, W. Plesiewicz, M. Berkowski, B. Boyce, T. R. Lemberger, and P. Lindenfeld, "Metallic nonsuperconducting phase and d-wave superconductivity in Zn-substituted $La_{1.85}Sr_{0.15}CuO_4$," *Phys. Rev. Lett.*, vol. 84, pp. 155–158, 2000.

[190] E. F. Schubert, "Delta doping of III−V compound semiconductors: Fundamentals and device applications," *Journal of Vacuum Science & Technology A*, vol. 8, no. 3, pp. 2980–2996, 1990.

[191] K. Muraki, S. Fukatsu, Y. Shiraki, and R. Ito, "Surface segregation of in atoms during molecular beam epitaxy and its influence on the energy levels in InGaAs/GaAs quantum wells," *Applied Physics Letters*, vol. 61, no. 5, pp. 557–559, 1992.

[192] Y. Kozuka, Y. Hikita, C. Bell, and H. Y. Hwang, "Dramatic mobility enhancements in doped $SrTiO_3$ thin films by defect management," *Applied Physics Letters*, vol. 97, no. 1, pp. –, 2010.

[193] E. Schubert, *Delta-doping of semiconductors*. 2005.

[194] M. H. Yang and C. P. Flynn, "Growth of alkali halides from molecular beams: Global growth characteristics," *Physical Review Letters.*, vol. 62, pp. 2476–2479, 1989.

[195] E. L. Pankratov, "Dynamics of -dopant redistribution during heterostructure growth," *The European Physical Journal B*, vol. 57, no. 3, pp. 251–256, 2007.

[196] W. Lee, J. W. Han, Y. Chen, Z. Cai, and B. Yildiz, "Cation size mismatch and charge interactions drive dopant segregation at the surfaces of manganite perovskites," *Journal of the American Chemical Society*, vol. 135, no. 21, pp. 7909–7925, 2013.

[197] R. A. De Souza, J. Zehnpfenning, M. Martin, and J. Maier, "Determining oxygen isotope profiles in oxides with time-of-flight sims," *Solid State Ionics*, vol. 176, no. 15–16, pp. 1465–1471, 2005.

[198] P. R. Kenway, S. C. Parker, and W. C. Mackrodt, "The calculated structure, stability and composition of the low index surfaces of La_2CuO_4 and Nd_2CuO_4," *Surface Science*, vol. 326, no. 3, pp. 301–310, 1995.

[199] C. C. Battaile, R. Najafabadi, and D. J. Srolovitz, "Simulation of segregation to free surfaces in cubic oxides," *Journal of the American Ceramic Society*, vol. 78, no. 12, pp. 3195–3200, 1995.

[200] H. B. Lee, F. B. Prinz, and W. Cai, "Atomistic simulations of surface segregation of defects in solid oxide electrolytes," *Acta Materialia*, vol. 58, no. 6, pp. 2197–2206, 2010.

[201] M. S. D. Read, M. S. Islam, G. W. Watson, and F. E. Hancock, "Surface structures and defect properties of pure and doped La_2NiO_4," *Journal of Materials Chemistry*, vol. 11, no. 10, pp. 2597–2602, 2001.

Curriculum vitae

Name:	**Federico Baiutti**
Date and place of birth:	07.10.1985 in Monfalcone (GO), Italy
Aug. 2011 - July 2015:	**Ph.D.**
	Max Planck Institute for Solid State Research, Stuttgart, Germany.
	Department of Physical Chemistry of Solids (Prof. Dr. Joachim Maier).
	Title of the final thesis: *"Heterogeneous doping and superconductivity in La_2CuO_4-based heterostructures."*
Sept. 2008 - Apr. 2011:	**M.Sc. in Materials Engineering**
	University of Trieste, Italy
	Title of the final thesis: *"Deposition and characterization of thin films of superconducting cuprates."*
Sept. 2008 - Apr. 2011:	**B.Sc. in Industrial Engineering**
	University of Trieste, Italy.
	Title of the final thesis: *"Problems on injection systems of diesel engines: study of a case."*
Sept. 2003 - July 2008:	**High school diploma**
	Liceo scientifico statale "M. Buonarroti", Monfalcone, Italy

Acknowledgements

At the end of this work, I would like to express my gratitude to Prof. Joachim Maier for giving me the opportunity to work in his department. I deeply appreciated his support and his valuable advices. Being part of his group has been a great occasion for my professional and personal development. Thanks to all the members of the Maier department for the help they offered in many occasions and for making the atmoshpere at work very pleasant and enjoyable.

Prof. Fisher and Prof. Weidenkaff are acknowledged for accepting the role of external members of my Ph.D. examination committee.

My deep gratitude goes to Dr. Giuliano Gregori, who supervised this work with passion, competence and patience.

Thanks to Dr. Gennady Logvenov, who trusted me and always took in great consideration my point of view. From him I acquired most of the knowledge which allowed this project to be completed.

Thanks to Georg Cristiani who had a central role in the daily work, offering his unique technical expertise and his very valuable scientific opinions. Together with him, I very much appreciated the support which was offered by Peter Specht, Ben Stuhlhofer and by all the members of the Technology Group at the MPI. I would like to acknowledge also Dr. Yi Wang, Dr. Wilfried Sigle and Prof. Peter Van Aken from the StEM Group for the precious collaboration on the project.

During the time of my Ph.D. I could always rely on my precious friends Adam, Anton, Elisa, Giuliano, Marco, Matteo, Piero. Thanks for your company, for being so trustable and honest, for sharing the nicest moments and for helping with the not so nice ones. To you guys are related all the memories of my days in

Stuttgart.

To my best friends at home and around the world Anna, Arturo, Chiara, Francesco, Giuseppe, Marco, Nicoletta, Piero and Rossella goes my heartfelt gratitude: luckily, certain things don't change, despite the time and the distance.

To my mum and dad, to my brother and his family, Afton and Nico, I dedicate this work. You are a costant presence and support, as you have always been. Grazie, a voi devo tutto.